Investigation of Novel Nanoparticles for Biomedical Applications

Matthew Taylor MPhys

MPhil

University of York

Physics

April 2018

Abstract

The aim of the work presented here is to investigate the oxidation behaviour of nanoparticles produced using novel physical vapour deposition methods with magnetic moments and saturation greater than commercially available Fe-oxide nanoparticles. The production of such nanoparticles is tailored towards usage in biomedical applications, where, due to health and safety concerns the strength and frequency of magnet fields is limited. As such the goal is to produce highly optimised and tailored nanostructures that offer the best magnetic performance possible under the medical constraints. This necessitates building a detailed understanding of the oxidation pathways and processes that nanoparticles undergo as the formation of oxide layers on nanoparticles hinders their magnetic performances.

Furthermore, while the oxidation of bulk materials is well-studied and documented applying this understanding at the nanoscale presents many challenges as oxidation behaviour at this level differs greatly based on the physical properties of the samples. Fe was used throughout this study due to the materials desirable magnetic properties and current use in medical applications. The study presented here examines the mechanisms behind the oxidation of spherical Fe/Fe_xO_y particles with the oxidation process enhanced through annealing at 200°C as well as attempts to create protective metal shells around pure Fe particles to preserve the iron core from oxidation. To this end investigation into the production of Fe@Cu, Fe@Ag, Fe@Al and Fe@Mg is given. Particle analysis was carried out using the wide variety of characterisation techniques available through electron microscopy using a JEOL 2011 TEM and JEOL 2200 FS (S)TEM.

It was found that diffusion through iron oxide grain boundaries in the particle shell had a significant effect with the diffusion coefficient estimated to be $4.67 \times 10^{-11} cm^2\ s^{-1}$. While the best performing metallic coating was Fe@Cu with particle exhibiting vastly different physical properties due to the addition of copper.

Contents

List of Figures

List of Tables

Acknowledgements

I would like to thank a number of people without whom this submission would never been possible.

Firstly, I would like to thank my colleagues at the University of Physics whose hard-work and support helped me transition from the Astrophysics to Condensed Matter groups. I am greatly appreciative of their efforts over the past few years. I would also like to thank my collaborators at Leicester, especially Katie Dexter for her hard-work in making the samples we studied.

I would like to thank my former colleagues Konstantinos and Teresa whose support and advice in the early days was greatly appreciated, in addition to the countless political discussion we had. I would also like to thank my colleagues at the Nanocentre who taught me how to use the microscopes without blowing the vacuum.

I also greatly thank my family for the unending supply of support and advice both physical and emotional, they provided me over the years, especially during my period of injury. Their help during the period of rehabilitation for my leg when I was at my lowest point remains a source of strength without which this submission would never have been possible. Thank you to my parents, my brother and my grandparents for all you have ever done for me.

Lastly, I would like to thank my partner, whose smiles and company over the latter years of my PhD kept me sane and laughing, and for her support and understanding throughout the last three years.

"All a failure can ever be, is the promise of future success."

Declaration

The work presented in this thesis is based on original research performed at the Department of Physics, University of York, UK, between October 2013 and April 2018 under the supervision of Dr. Roland Kröger of the Nano- and Biomaterials Physics Group. I confirm that none of this research has previously been submitted for any other qualification at this, or any other University, all other sources are acknowledged clearly as References in the text.

Matthew Robin Taylor

Chapter 1: Introduction

The motivations for the study of oxidation in iron-based nanostructures are manifold; on the one hand nanotechnology is a well-established, fast growing, disruptive field, with the opportunity to enhance our current understanding and technological ability in a wide range of fields such as biomedicine, magnetic data storage, and imaging[1]. By 2019 the market for nanomedicine alone is expected to exceed $526 billion according to financial reports[2]. On the other hand, iron-based nanostructures offer strong magnetic properties that make them highly desirable in biomedical and therapeutic fields[3], where it is hoped they can be functionalised to aid in the mortification of cancerous cells or targeted drug delivery, allowing for higher doses without the risk of damage to the rest of the body. Therefore, it would be beneficial to gain a deeper understanding of how such systems function on the nanoscale for both medical and mechanical purposes[3].

Nanoparticles can be synthesised or found naturally and consist of a wide variety of materials and alloys. Some particularly well-known and well-studied nanostructures include: carbon nanotubes, which have been considered for many applications, including the field of neurobiology[4]; and silver nanoparticles which have been used to kill bacteria in fabrics[5]. Nanoparticles are a fascinating area of study due, in part to their size-dependent properties, often being described as a ‘bridge’ between the classical and quantum effects. This is because of quantum effects can be observed when the size of a nanoparticle is very small (~ 10 nm)[6]. These unique properties arise from a significant proportion of the particle’s atoms being located at the surface. This can be visualised by imaging a particle with a diameter of 2 cm compared to one with a diameter of 10nm. The former will have only one atom in ten million located at the surface whereas for the nanoparticle it will have one atom in every ten, while the exact number depends on the crystal structure this illustrates the large difference in the number of surface atoms. This difference of five orders of magnitude is key, with surface atoms behaving very differently to bulk atoms in many important areas such as chemical bonding. Understanding these behaviours and properties of nanoparticles is essential to exploit these properties.

One particularly interesting application of magnetic iron nanoparticles is the mortification of cancerous tissue through magnetic field induced hyperthermia (MFH). Whereby heating generated by iron nanoparticles due to the oscillation of an external magnetic field is used as a treatment for cancer. This is because proteins in cells that are heated to around 42°C are denatured and their membranes become permeable resulting in the death of the cell or increased susceptibility to traditional cancer treatments such as Radio- and Chemotherapy[7]. This would allow for lower doses of the normally severely damaging cancer drugs to be used and in some cases reduce the collateral damage of such treatments through increased targeting. Such outcomes are highly desirable and as such, small superparamagnetic and ferromagnetic iron nanoparticles are considered for use in this manner. However, due to the limits on the strength and frequency of an external magnetic field applied to a human body achieving the desired levels of heating and performance is challenging. As such understanding the mechanisms behind the oxidation of such particles is critical as oxide formation serves to lower the magnetic response of iron particles which limits their viability in medical settings.

In this chapter, an introduction to magnetic iron oxide nanoparticles will be given along with a short literature review to explain the motivation for this study; this will be followed by a description of the synthesis of the nanoparticles and end with an explanation of: the experiments carried out, the thesis structure and a discussion of the key concepts.

1.1 Magnetic Nanoparticles: Motivation and Background

The most common material used in the development of magnetic nanoparticles for biomedical purposes is ferromagnetic iron. Ferromagnetism is important as it offers the best magnetic properties of all materials in terms of magnetic response, and its ability to retain a magnetic field without the presence of an external field. The magnetic susceptibility of ferromagnets can be up to four orders of magnitude higher than that of paramagnets or diamagnets[8]. Out of the group of ferromagnetic elements iron, nickel, and cobalt only some iron oxides have been approved for use in human medicine due to the issues surrounding the biocompatibility of the other materials. This short-coming is not a major limitation as iron contains the largest magnetic moment of the three materials at ≈3.19 μ_B per atom with nickel and cobalt possessing 1.20 μ_B and 2.54 μ_B per atom respectively[9]. This, and the fact that iron also possesses the largest magnetic susceptibility of the three materials making it the ideal candidate due to the restrictions imposed on using magnetic fields in medical settings, makes iron the most commonly studied material for biomedical nanostructures[10]. As such iron nanoparticles are typically the basis any material system considered for medical applications. The typical system will consist of the iron base material and a functional material (often in the form of a shell) that will act to either transport a drug, attach to sample, or serve some other medical purpose.

Iron, and its oxides, are naturally abundant in the earth crust and have been an integral part of human civilisation since antiquity. Iron and iron oxides are important across a wide variety of contemporary fields such as clean fuel, data storage[11], water treatment[12] and biomedicine[13,14] with each application desiring their own specialised iron/iron oxide particles[15]. Of particular interest are core-shell iron structures consisting of a metallic iron core and either an oxide or secondary metal shell, these particles possess readily controllable physical and magnetic properties and the ability to insulate the magnetic iron core from oxidation, thereby increasing the overall magnetic response of the nanoparticle, especially in the case of iron/metal core-shell particles[13]. Despite the high degree of attention these materials attract, the study of nanoparticles still faces many challenges. Undoubtedly the largest barriers to continued progress across all these fields is the lack of magnetic

response and reactivity that can occur as a result of oxidation [15]. As such understanding the nature of the oxidation process occurring within these particles is of great importance.

The oxidation processes and characteristics of bulk iron have been extensively examined at both academic and industrial levels[16,17]. However, the nature of these processes is still only just beginning to be understood. The difficulty becomes apparent when one considers the substantial number of sizes and shapes that such nanoparticles can exhibit. As physical characteristics determine the electronic, structural, and magnetic properties, this wide array of particle morphologies results in a wide variety of characteristics. Furthermore, the effect of temperature on the oxidation of these particles is of critical importance, as the idea of heating magnetic particles *in vivo,* as a potential method of targeting (or aiding in the targeting of) cancerous cells is one possible application of magnetic nanoparticles[18].

Research of the medical use of magnetic nanoparticles began in the late 1950's by Gilchrist *et al*[19], where the possibility of using external magnetic fields with nanoparticles as a non-invasive agent was addressed. Through this work the most notable challenges, namely the possible toxicity of the agent and the safety of the alternating magnetic field (AMF) were established, these problems are still debated today and frame the basic motivation for studies into the oxidation of iron oxide nanoparticles. One particular problem is the upper limit of the strength of any external magnetic field which can be safely applied to a patient[20]. Therefore, maximising the magnetic response of the particles to get the optimal performance out of particles within a range of magnetic field strength values is a key challenge for materials scientists.

Currently, four main avenues of functionality for magnetic nanoparticles which are being explored in biomedicine are:

- Drug delivery agents
- Cell separation techniques
- MRI contrast enhancers
- Magnetic Hyperthermia

Of those four main areas of usage MRI contrast enhancement is the most mature where iron oxide nanoparticles have been used as agents for over 25 years and are

becoming increasingly common, as per mole iron-based contrast is typically stronger than the traditional Gd-based agents[21]. Furthermore, as Gd-based agents have been shown to occasionally cause health problems in some patients, such as fibrosis in renal-impaired patients[22] and with the increasing quality of iron oxide based agents, this is leading to more research and development on superparamagnetic iron oxide nanoparticles (SPIONs) as a potential new generation of agents[23]. Furthermore, with the development of magnetic particle imaging (MPI), which uses superparamagnetic nanoparticles to produce 3D maps in a similar manner to a gamma camera, even more attention is being paid to this application of iron nanoparticles.

Targeted drug delivery using magnetic nanoparticles is a technique that requires the functionalisation of magnetic iron nanoparticles, such that a therapeutic agent is bound to an iron/iron oxide nanoparticle, and the magnetic core then allows for the targeting of previously difficult-to-reach tumours. Furthermore, in the ideal case, the therapeutic agent would be embedded in a material that would only release the drug after heating; oscillation of the external magnetic field can achieve this heating of the particles. This would allow for the administration of higher doses of drugs with less risk to surrounding healthy tissue. In this respect, the drug delivery and magnetic hyperthermia applications share common requirements and problems.

A similar technique is that of magnetic nanoparticle hyperthermia (MNP) whereby cancerous tissue is destroyed through the heating of nanoparticles via external oscillating magnetic fields at cancerous regions of the body. The benefits of such techniques are obvious as the technique could in principle replace or limit the need for dangerous and toxic chemotherapy drugs or radiotherapy which damage surrounding healthy tissue as well as cancerous tissue. Unfortunately, current commercially available nanoparticles cannot achieve the required heating for this treatment to be effective stand-alone. However, it has been suggested that magnetic particles used in conjunction with chemotherapy, radiotherapy and other cancer treatments can increase the success rates of the treatments[24,25]. The difficulty in reaching effective heating levels arises when the effect of external magnetic fields on the body are considered; while increasing the strength of the applied magnetic field would increase the heating output of a magnetic particle, the field itself leads to serious damage to healthy tissue. This is due to the fact that as eddy currents are

formed as the field amplitude is increased, this eddy currents occurring in surrounding tissue and bone structures can lead to severe muscle and nerve damage. As such a limit is placed on the maximum strength and frequency of an applied magnetic field which can be used in a medical setting, this limit (the Atkinson-Bresovich limit) is that the product of the magnetic field strength H_0 and frequency f and cannot exceed ($H_0 \times f = 4.85 \times 10^8$ Am^{-1} s^{-1}) [26].

Due to the Atkinson-Bresovich limit, one of the key issues regarding the use of magnetic nanoparticles in biomedical settings is the optimisation of the particles' magnetic response. To achieve the best possible magnetic properties within these limits a detailed understanding of the material systems is critical. Arguably the largest concern regarding the optimisation of magnetic iron nanoparticles lies in the spontaneous and rapid oxidation of iron in air. This oxidation resulting in particle shells of iron oxide has a negative effect on the magnetic properties of the particles, as many of natural iron oxides within the range of temperatures and conditions that would be common in biomedical settings are antiferromagnetic. That is, the magnetic moments of the atoms in the particle align such that neighbouring magnetic moments 'point' in the opposite direction, this results in particles with anti-ferromagnetic or ferrimagnetic oxides possessing a significantly lower magnetic response. Furthermore, as iron readily oxidises this results in weak magnetic performance from particles that have oxidised. Thus, the understanding of the processes governing oxidation at the nanoscale is critical to improve the performance of nanoparticles to be used in biomedical settings.

Furthermore, other key challenges facing the study of magnetic nanoparticles are:

- the effective particle size,
- surface effects,
- stoichiometry.

The effective particle size is important to be considered as the magnetic and physical characteristics of nanoparticle samples can vary widely based on the size and shape distributions of the sample. As such, methods of synthesis that can generate monodisperse iron core-shell structures are critical. Secondly, the surface effects of the particles become important due to many applications of magnetic nanoparticles requiring a form of biological functionalisation[27]. Moreover, as the

diameter decreases, the surface atoms make up an increased proportion of the total particle and surfaces have a significant role in the magnetic properties of the particles, where surface oxidation is believed to play a major role. Lastly, particle stoichiometry has been shown to have the effect of lowering the magnetic saturation (M_s) of the material with pure stoichiometric magnetite possessing an M_s of 480 kA/m, which decreases as non-stoichiometry increases[28]. This effect has been observed during particle synthesis and after long periods of storage.

The study presented here is motivated by the unique challenges posed by the applications of iron nanostructures and the critical importance of understanding the oxidation processes they undergo. This led to an exploration of the iron nanostructures and attempts to drive the oxidation process through thermal means. To this end, a variety of iron nanostructures were designed based on the desired shell material; samples of pure iron that could form an initial oxide shell layer and samples of iron that were coated in a variety of metallic materials with the desire to form a protective shell layer.

1.2 Research Objectives and Aims

In the study presented here, iron and iron oxide core-shell nanoparticles are investigated and characterised to determine the distribution of physical characteristics such as size and shape, as well the extent of oxidation and the processes that drive it. The iron oxide particles are split into two types: core-oxide particles consisting of an iron core and oxide shell, and core-metal particles which consist of an iron core and a secondary metal shell.

All sets of samples were characterised using scanning transmission electron microscopy (STEM) or conventional transmission electron microscopy (CTEM). Particle size and morphology were characterised using CTEM to provide a balance between accuracy of measurement and coverage of the samples, while particle composition was determined using Selective Area Electron Diffraction (SAED) and, where appropriate, Energy Dispersive X-ray Spectroscopy (EDX). Samples were heated in an alumina tube furnace with a maximum temperature of 1500K to

thermally induce further oxidation where needed, as oxidation times in air are impractically long beyond initial oxide formation. Detailed investigation of the structure of the samples was performed using high-resolution STEM and TEM (HRSTEM/HRTEM).

The first sub-set of particles is core-shell structures, where the attempt has been made to deposit a protective metallic shell around the iron core. The goal of this approach is to attempt to create a particle where the iron core is shielded from oxidation, thus preserving the high magnetic moment associated with the core metal. The second type of particle is an iron core surrounded by a layer of iron oxide, the goal with these particles is to investigate the behaviour of the particles when oxidation is thermally induced. Particles were prepared using a gas aggregation cluster source under ultra-high vacuum conditions and were deposited directly onto copper TEM grids with carbon support films. This approach allowed for control over the physical characteristics of the samples produced and the possibility of coating the particles in secondary metal layers.

The initial samples were prepared at varying temperatures with the aim of exploring how the conditions in the core-shell deposition chamber affect the samples; these samples were then moved into ambient surroundings to form their initial oxide layers. For samples that were to be coated further the core-shell chamber would be heated and filled with the target metal before being deposited and left to cool. Samples designed to be heated *ex situ* after deposition would be prepared in a similar way and removed immediately into atmospheric conditions to form their initial oxide. Any subsequent heating to thermally force oxidation was performed using a tube furnace at 200°C which is considered a low temperature for oxidation heating experiments.

1.3 Thesis Outline

This thesis will begin with a general introduction to the key concepts surrounding iron and iron oxide and a discussion of the current understanding regarding the known processes that govern the oxidation of bulk iron and how they may apply at the nanoscale. The fundamental theory behind the characterisation using (S)TEM and the many avenues it provides for obtaining supplementary data will be presented. This will then be followed by a detailed description of the method used to synthesis the samples and a discussion of its advantages over other common methods of creating core-shell nanoparticles. Data will then be presented regarding the coating of iron nanoparticles with copper and the implications of this will be discussed, along with attempts to insulate the iron nanoparticles with other metal materials. Lastly, results regarding the investigation into oxidation processes at the nanoscale will be presented and discussed. Finally, the thesis will discuss the results and compare the experimental data to that found in other studies, with the goal of formulating a working model for the oxidation processes of metallic nanoparticles.

1.4 Key Concepts: Oxidation of Iron

1.4.1 Oxides of Iron

There are six iron oxides composed of Fe and O: namely wüstite (FeO), hematite (α-Fe_2O_3), Maghemite (γ-Fe_2O_3), (β-Fe_2O_3), (ε-Fe_2O_3) and Magnetite (Fe_3O_4). The most common naturally occurring iron oxides in current biomedical settings are maghemite (γ-Fe_2O_3) and magnetite (Fe_3O_4). The latter, magnetite, is a black magnetic material whose molecular formula can be written as a combination of wüstite (FeO) and hematite (α-Fe_2O_3) and has the strongest magnetism of all naturally occurring minerals. Magnetite has an inverse spinel structure with oxygen forming a face-centered cubic (FCC) structure, the iron atoms located at the interstices with Fe^{2+} and Fe^{3+} ions found at the octahedral sites while only Fe^{3+} ions are found at the tetrahedral sites it is ferromagnetic until the Curie temperature of

853K[29] whereupon it becomes paramagnetic. Maghemite, however, is a brown, magnetic mineral found in soils and can be formed through the weathering or low-temperature oxidation of magnetite and other spinels; it is metastable with respect to hematite at higher temperatures (α-Fe_2O_3). It is isostructural with respect to magnetite but with cation deficient sites.

Of the remaining iron oxides, hematite is the oldest known compound and is very common in soils and rocks. It is extremely stable and mined as the main ore of iron. It possesses a trigonal crystal structure and is paramagnetic. Lastly, wüstite has a simple cubic structure, which shares a similar structure to NaCl, the mineral has been found in meteorites and deep-sea trenches and displays a high concentration of defects making pure wüstite crystals difficult to obtain.

The nanostructures explored in this study consist of multiple different morphologies ranging from traditional spherical particles to cubic structures. Cubic nanoparticles have recently seen an increase in interest, primarily due to their potential advantages in catalytic activity and their high specific absorption rate (SAR) values, which is critically important in medical hyperthermia[30]. The oxidation processes behind both spherical and cubic nanoparticles have been explored in detail by researchers, yet many aspects of the oxidation process remain uncertain[31,32]. The initial oxide layer evident after the particles are removed from the deposition chamber into atmospheric conditions can be readily explained with Cabrera-Mott theory, the foundation of the theory of metal oxidation[33].

The reactions of iron and the formation of iron oxide are frequently used as examples when discussing oxidation behaviours. This is likely due to the availability of the material as well as its widespread use across many fields and applications. As noted previously, iron forms six distinct oxides, three of which are stable: wüstite (FeO), magnetite (Fe_3O_4) and maghemite (Fe_2O_3) with the phase diagram shown above in Fig. 1.1. As it is common for all three oxides to exist in oxidised iron it is sensible to divide the oxidation of the iron-oxygen system into three distinct temperature regions above and below 570ºC and above 900ºC with oxygen partial pressures similar to those in atmosphere[34,35,36].

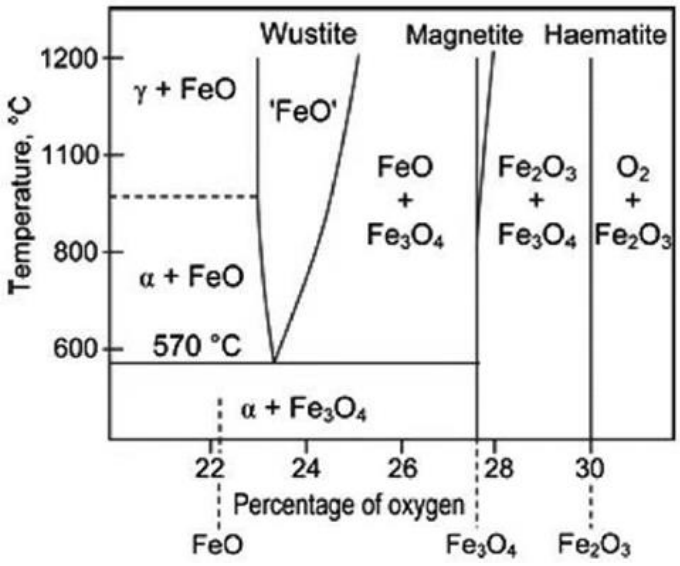

Figure 1.1. Phase diagram for iron oxide[37].

At high-temperatures above 750ºC-900ºC, the oxide shell was found to contain no significant amounts of either magnetite or maghemite, as the disassociation pressure of these two oxides is substantially lower than for wüstite[38]. In this regime, oxidation is observed to be linear although at certain oxygen partial pressures, the rate will transition to parabolic. Above 570ºC the oxide shell remains mostly composed of FeO, however now thin films of Fe_2O_3 and Fe_3O_4 can be seen, with the Fe_3O_4 being the larger of the two layers. Below 570ºC, wüstite becomes unstable in bulk and is not present, with the oxide shell being composed primarily of Fe_3O_4. When the oxide shell is very thin, wüstite may exist as a thin film at the metal-oxide interface at temperatures approaching 400ºC[39]. At this temperature and below, the growth rate of the magnetite phase controls the oxidation rate, and, furthermore, the mechanism of oxidation is different for the separate oxide phases, with both wüstite and magnetite oxidising predominately through cation diffusion, although oxygen in-diffusion does have a non-trivial role in the oxidation of magnetite[40]. Maghemite however, oxidises primarily through oxygen anion diffusion and it is possible that at these low temperatures oxygen in-diffusion may reach the metal-oxide interface and penetrate the metal. It was found that there was a change in the oxidation growth rate at low temperatures, from parabolic at temperatures above 200ºC to logarithmic at temperatures below this.

Having discussed the iron material system and its observed oxidation behaviour in bulk, a discussion regarding the known methods of oxidation will be given, this will include a short historical overview of early models, before focusing on the theory behind the two main models for the prediction of oxidation.

1.4.2 Theories on the Oxidation Metals

In 1923 oxidation of metals was divided into two categories by Pilling and Bedworth according to the relative formation of oxide to metal consumed[41]. This was represented as the 'Pilling-Bedworth ratio' which compares the volume of the oxide produced with the volume of metal consumed; with materials whose ratio was greater than unity being described as 'protective' oxide shells, as they tended to surround the particle completely. This leads to the oxide shell growing according to a parabolic relationship. For materials with ratios below unity it was argued that the oxide shell would be porous and non-protective and grow according to a rectilinear growth law.

Pilling and Bedworth's description proved to be effective only in limited cases. While initially it was supported by experiments on calcium and copper (light and heavy metals with ratios of 0.64 and 1.75 respectively)[42]. Pilling and Bedworth assumed that the oxidation proceeded by in-diffusion of oxygen through the oxide film. However this has been shown to not always be the case and that the dominant diffusing species is typically the metal 'out-diffusing' towards the oxygen[43]. This makes sense in heavier metals, especially where the metal cation is often smaller than the oxygen anion. However, for metals whose diffusion mechanism operates through transport of material from the surface to the metal-oxide interface, the Pilling-Bedworth rule has some degree of applicability.

An example of such a system would be the linear oxidation of magnesium above 475ºC, although there are many exceptions to their rule. The main flaw in the early understanding of oxidation was the poor assumption that stress and strain effects acted in opposition to oxidation; it was assumed that small compressional stresses could act to 'push' together cracks in oxide scales and retard oxidation.

However, there are cases of materials that would experience ‘breakaway’ oxidation above certain temperatures, which suggested the role of stress and strain energies in the oxidation process is more complicated than allowed for in the early models[44]. As the understanding of oxidation behaviour increased it became necessary to consider the mechanisms behind the growth of oxide scales and films; this is often represented in the form of ‘oxidation *vs* time’ curves, which can in most cases be described simply. The most common of these curves is split into two distinct categories that depend on the thickness of the oxide scale formed: where the scale is thick (often defined as >1μm), *parabolic* and *linear* time curves are observed and when the scale is thin, *logarithmic* and *cubic* curves predominate[35].

Wagner Theory of Oxidation

In the case of thick films, the most well tested theory was developed by Wagner in 1933 and provides a means by which the rate of oxide growth can be linked to measurable transport properties of the material. Based on the parabolic relationships that had been observed previously,

$$\frac{dX}{dt} = \frac{k_p}{2X} \tag{1.1}$$

Where X is the film thickness and k_p is the parabolic rate constant the rate of oxide growth[45]. Therefore, the parabolic kinetics can be seen as the transport of material along a gradient (driving force) that decreases as the oxide thickness increases[46].

$$X^2 = k_p t \tag{1.2}$$

The details of the transport mechanism (if metal cation diffusion is dominates oxygen anion diffusion) depend on the material in question. For example, it has been found that iron cation diffusion dominates in magnetite while maghemite is dominated largely by oxygen anion diffusion[47]. However, as the diffusion species are electrically charged as shown in Fig. 1.2 both electronic and ionic transport is needed to cause oxidation at the oxide-gas interface, with the respective fluxes being

driven by both chemical and electric field gradients. The general expression for the flux of a diffusing species is given by;

$$J_i = \frac{D_i C_i}{kT}\left[-\frac{d\mu_i}{dx} + q_i E\right] \tag{1.3}$$

Where *i* represents the species or defect being transported, for example, an electron or iron ion. C_i is the concentration of the species or defect, D_i the diffusion coefficient, μ_i the chemical potential and q_i the charge, k and T represents the Boltzmann constant and absolute temperature respectively with E as the electric field. The chemical potential μ_i can be expressed further as $\mu_i = kT\ ln(C_i) + constant$ for ideal diffusing species[48].

The ability to express electrical transport properties in terms of diffusion characteristics is derived from the Nernst-Einstein relation, which establishes the relationship between the molar conductivity Λ and the diffusion coefficient and can is given by;

$$D_i = \frac{RT}{q_i^2 F^2}\Lambda_{m,i}^0 \tag{1.4}$$

Where q is the charge on the ion *i*, F is the Faraday constant, R is the gas constant and T is the absolute temperature. This relationship assumes that the electric field is small such that ($qEa << kT$) where a is the ionic jump distance. When this relationship holds true Wagner's theory of oxidation can be applied. However when the electric fields are large enough that $E \ll \frac{kT}{aq}$ this relationship break downs, such as in the case for thin films, Cabrera-Mott theory must be applied[49].

A full derivation of Wagner theory is beyond the scope of this study as it can only be applied in cases where the oxide film is suitably thick, which is also shown to not occur in nanoparticles. The final result expresses the parabolic rate constant as a function of the diffusion coefficient for a given molecular oxygen activity at the oxide-gas interface[50].

$$k_p = \frac{6}{f} D^* \tag{1.5}$$

Where D^* is the diffusion coefficient for a given oxide-gas interface oxygen activity and f is the correlation factor for the metal and oxygen ion self-diffusion mechanism.

Cabrera-Mott Theory of Oxidation

When the oxide film is below the thickness stated previously then the Nernst-Einstein relationship and the assumption of charge neutrality are no longer valid, and the theory of oxide growth must take into account the atomic jumps in the presence of large electric field gradients. Cabrera and Mott developed their theory in 1949 in an attempt to describe the oxidation process in atomistic terms[33]. The first assumption is that electrons can pass freely from the metal to the oxide shell so that surface oxygen atoms may be ionised. The resulting effect is that a uniform electric field is created across the oxide film, due to the positive surface charge from the metal ions at the metal/oxide interface and a negative surface charge due to the excess oxygen ions at the surface. In Wagner theory, due to the small electrical fields, transport is largely driven by the chemical gradient across the oxide film. However, in Cabrera-Mott theory the electric field drives the ionic transport through the diffusion of metal ions out towards the surface and the diffusion of oxygen ions inwards[46].

Electrons may be transported across the film through two possible mechanisms namely tunnelling across the potential barrier which binds them to their original atom, and transport through thermionic emission. In the case of tunnelling, the critical limit was considered by Fromhold and colleagues who solved the problem numerically were able to determine that the critical thickness for electron tunnelling was of the order of 25Å, above which, the tunnelling current would become too small to account for oxide growth[46,51]. This was backed by observation for oxidising materials at low temperatures which achieved films on average between 20-30Å. The mechanism described by the Cabrera-Mott theory of oxidation relies on this tunnelling of electrons through the surface such that surface oxygen is ionised; the simplest such ionisation interaction is give in Eq. 1.6 and is shown in Fig. 1.2.

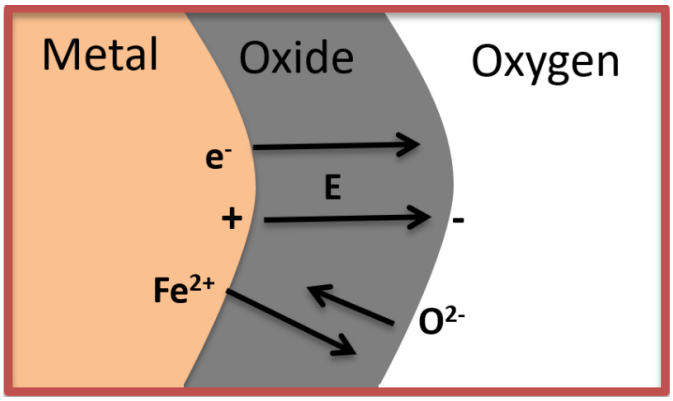

Figure 1.2 Schematic diagram of the basic surface interaction that involves an electron tunnelling through the oxide shell to the surface to ionise excess oxygen atoms. The resulting potential acts as a driving force to facilitate the ionic transport of iron and/or oxygen ions across the oxide.

$$\frac{1}{2}O_2(gas) + 2e(metal) \rightarrow O^{2-}(surface) \tag{1.6}$$

Fig. 1.2 shows a schematic representation of a basic surface interaction that results in the oxidation of material on the particles surface, free electrons e^-pass through the oxide shell freely resulting in a separation of charge, with the anode at the metal/oxide interface and the cathode at the oxide/gas interface. This drives the transport of Fe^{2+} ions through the oxide shell to the surface and O^{2-} ions through the shell to the core, the relative rates of in- and out-diffusion are dependent on the ions being transported.

Other more complicated surface interactions can occur, but only the simplest case will be explored as the same principles can be applied for all surface interactions. If the interaction is assumed to be at equilibrium, then the equilibrium constant is given in Eq. 1.7 as in the case where the Gibbs free energy change is zero, then the ratio of activities in the reaction are equal to the equilibrium constant.

$$K = \frac{a(O^{2-})}{a(O_2)^{1/2}a(e)^2} \tag{1.7}$$

Where K is related to the Gibbs free energy change and can be expressed as;

$$K = \frac{\Delta G}{kT} \tag{1.8}$$

And $a(O_2)$ is given by;

$$a(O^{2-}) = \frac{n_0}{N_s} \tag{1.9}$$

Where n_0 is the number of excess oxygen ions and N_s is the total number of oxygen ions per unit of surface area. The electron activity is given by[46];

$$a(e) \ = \exp\left(-\frac{e\Delta\Phi}{kT}\right) \tag{1.10}$$

Where $\Delta\Phi$ is the Mott potential, from these equations we can derive an expression for the number of excess oxygen ions. The number of excess oxygen ions is therefore given by;

$$n_0 = N_s \, a(O_2)^{1/2} exp\left[-\frac{(\Delta G + 2e\Delta\Phi)}{kT}\right] \tag{1.11}$$

This equation was solved for the Mott potential $\Delta\Phi$, which can be estimated from[46].

$$\Delta\Phi \approx \frac{\Delta G}{2e} \tag{1.12}$$

To calculate the diffusion rate caused by the electric field, Cabrera and Mott assumed that the rate-controlling step of the process is the injection of defects into the oxide shell at one of the two interfaces. This introduction of defects has been highlighted schematically in Fig. 1.3. In the simplest case, the defect, which can be a metal interstitial or oxygen vacancy, is introduced at the metal/oxide interface. The metal interstitial defect is more likely to occur as, under the electric field, it acts to bias the direction of travel for the ion in the direction of the particle surface. As such the potential barrier the ion must overcome to jump towards the core of the particle is raised by $qa\Delta\Phi/2X$, As a result, it is possible for the field to become so large that ion transport in the direction of the core is negligible due to an insurmountable potential barrier in that direction.

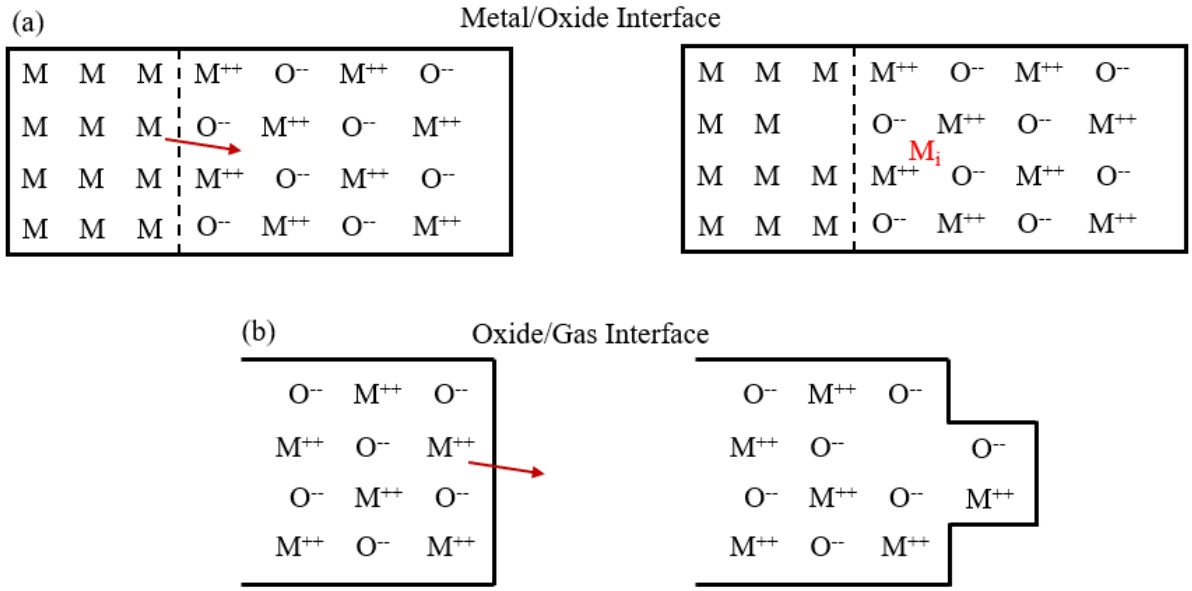

Figure 1.3 Illustration of the basic surface interaction and limiting process in Cabrera-Mott theory for the injection of a point defect into the oxide film at the metal/oxide and oxide/gas interfaces. (a) the transfer of a metal atom to an interstitial site in the oxide shell and (b) the transfer of a metal ion to a site on the surface of the particle creating a metal vacancy in the shell.

The probability of an atom overcoming the potential barrier and travelling into the oxide shell (where it should be noted that the activation energy for subsequent jumps through the oxide is much lower than the energy required for the initial jump) can thus be expressed as in Eq. 1.13[52].

$$\gamma = exp\left(\frac{-W}{kT}\right) exp\left(\frac{qa\Delta\Phi}{2kTX}\right) \tag{1.13}$$

Where, W is the activation energy required to make the 'saddling' jump into the oxide, q is the electric charge of the ion, a is the interatomic distance, $\Delta\Phi$ is the Mott potential, X is the oxide shell thickness, k is the Boltzmann constant and T is the absolute temperature.

This expression comes from the fact that the chance of an ion overcoming a potential barrier in the absence of any electric field would be $exp\left(\frac{-W}{kT}\right)$, however, as mentioned the electric field will lower the potential barrier by $qa\Delta\Phi/2X$. Furthermore, the chance per unit time for the ion to overcome the potential barrier will be the value in Eq. 1.13 multiplied by the ionic jump attempt frequency υ which

represents the number of ‘attempts’ an ion will make per second to overcome the potential barrier[53].

$$\gamma(t) = vexp\left(\frac{-W}{kT}\right)exp\left(\frac{qa\Delta\Phi}{2kTX}\right) \tag{1.14}$$

The overall diffusion rate can be calculated as the number of ions that diffuse successfully across the oxide per unit time; which would be given by the product of $\gamma(t)$ and N_0 the number of ions in positions to diffuse at a given time. This would lead to an increase in the oxide shell given in Eq. 1.15[54].

$$\frac{dX}{dt} = N_0\Omega v\ exp\left(\frac{qa\Delta\Phi}{2kTX} - \frac{W}{kT}\right) \tag{1.15}$$

Where Ω is the oxide volume produced per diffusing ion with all other variables maintaining the definitions given previously. As can be seen in Eq. 1.15, as the oxide shell thickness increases, the rate of oxidation drops, while it will never reach completely zero as there will always be a finite chance for an atom to jump into the oxide it can become negligible. The value for the negligible oxidation rate is arbitrary and was defined by Cabrera and Mott’s original paper as to be (10^{-15} ms^{-1}) which is equal to roughly 30nm per year oxide growth. When the rate becomes negligible, however, should be considered with reference to the material and context.

The limits to the applicability of Cabrera-Mott theory can be determined by first considering the velocity of drift for a diffusing particle, which can be expressed as the distance travelled in a single ‘jump’ into the oxide shell, multiplied by the chance of overcoming the potential barrier and the attempt frequency.

$$\frac{dX}{dt} = av\ exp\left(\frac{qa\Delta\Phi}{2kTX} - \frac{W}{kT}\right) \tag{1.16}$$

Where the interatomic distance a provides the distance travelled by the ion in each jump, this can be simplified and written as shown in Eq. 1.17[46].

$$\frac{dX}{dt} = \frac{D_i}{a}exp\left(\frac{X_1}{X}\right) \tag{1.17}$$

Where D_i can be linked to the diffusion coefficient with similar dimensions shown in Eq. 1.18 and X_1 which provides the upper limit for validity of the theory shown in Eq. 1.19.

$$D_i = a^2 \upsilon \exp(-\frac{W}{kT}) \tag{1.18}$$

$$X_1 = \frac{qa\Delta\Phi}{2kT} \tag{1.19}$$

Using iron as an example we can construct an estimate for the predicted shell thickness using the Cabrera-Mott approach. Working through the variables in 1.16 we can estimate the value for N_0 as the number of iron atoms at the metal/oxide interface. In practice, this is an overestimation as not all the atoms at the interface will be on active sites and capable of making the jump into the oxide shell. As such, the oxidation will be an overestimate with the true rate being somewhat slower. Assuming a spherical iron particle with a diameter of 20nm we would expect that $N_0 = 6.13 \times 10^{18}\ atoms\ cm^{-2}$. The value for oxide formed per diffusion iron can be calculated as the volume of the magnetite unit cell per iron atom; the magnetite cell has a lattice parameter of 0.839nm and consists of 8 Fe3O4 units for a total number of 24 Fe atoms and 32 O atoms. We can estimate that $\Omega = 2.46 \times 10^{23}\ cm^3 atom^{-1}$[55]. The jump attempt frequency is analogous to the atoms vibrational frequency which can be modelled as a simple harmonic oscillator with a frequency v[56].

$$v = \frac{\omega}{2\pi} = \frac{1}{2\pi}\sqrt{\frac{k}{m}} \tag{1.20}$$

Where m is the atomic mass and k is the force constant. This value is usually approximated to $v = 1 \times 10^{13}$ s^{-1} as this is a good approximation of the atoms vibrational frequency[57]. Using values in the literature for the α-Fe force constant (1520 Nm^{-1}) we get a vibrational frequency of $v = 2.03 \times 10^{13}\ s^{-1}$[58]. The charge on the ion is $q = +2e$ and the interatomic spacing is approximated to be $a = 0.25nm$ as the bond length can be affected in many ways but is often of this order of magnitude[59]. At room temperature kT can be estimated as ~ 25meV. The value for the Mott potential can be estimated using Eq. 1.13 with a literature value for the free-

energy change being $\Delta G = 5.26\ eV$[60]. The activation energy for the ion to make a 'jump' into the oxide shell is heavily dependent upon the nature of the system in question. For this example, a literature value representing the activation energy for oxidation in oxygen at room temperature has been used with $W = 1.39\ eV$[61].

The result of the calculation can be seen in Fig. 1.4 and shows the exponentially decreasing diffusion rate with increasing oxide thickness. Assuming the criteria postulated in Mott's original work as to what should constitute a negligible growth rate of $\frac{dX}{dt} = 10^{-15}\ ms^{-1}$ this results in an oxide shell with a thickness of 2.5nm for particles oxidised in atmospheric conditions which fits well with the initial observation observed in iron nanoparticles[62,63].

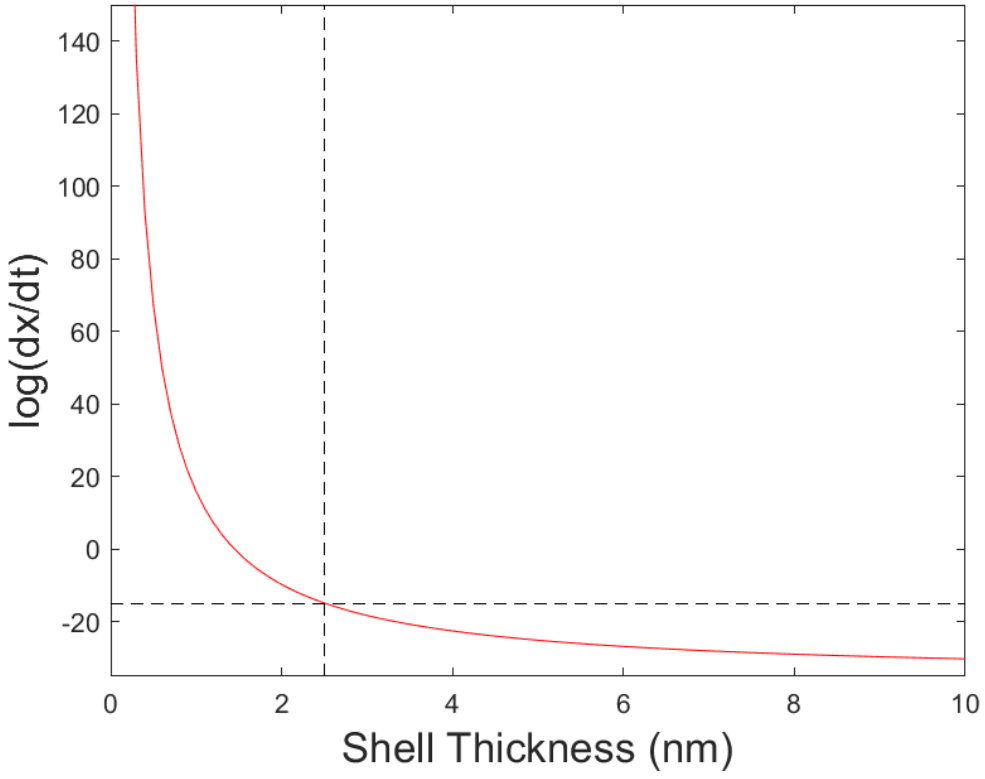

Figure 1.4 Graph showing the result of the oxide shell thickness calculations for the iron/iron oxide system, the black dashed lines showing the point at which the oxidation rate reaches Mott's criteria for negligibility (10^{-15} ms^{-1}). An oxide shell thickness of 2.5nm is predicted in this manner and fits well with observations made in the literature.

1.4.3 Oxidation of Nanoparticle Structures

The models discussed so far were developed for considering bulk materials with either thin or thick oxide films, however, the oxidation of nanoparticles presents interesting limitations. For example, the geometry of nanoparticles has been shown to have a significant effect on the properties of the particles. One example for this is that cubic shaped nanoparticles have shown advantages in terms of catalytic properties, packing density and orientability[63]. It was found that for cubic nanoparticles, oxidation would be enhanced at the centre of the side facets due to ionic transport of material along a strain gradient.

Generally, oxidation in bulk surfaces results in the strain in the oxide film being homogenously distributed and decreasing away from the metal/oxide interface, if the strain is large enough, due to the misfit between the core and oxide lattices, then misfit dislocations will be introduced at a critical thickness[64]. This allows for the relaxation of the strain in the lattice. It was found however that for cubic particles, the strain in the oxide increased away from the metal/oxide interface towards the centre of the facet[65].

The mechanism identified to account for the strain gradients and was explained using a modification to Fick's second law. Fick's laws were developed by Adolf Fick in 1855 and describe the diffusion coefficient of a material; the one-dimensional formulation is discussed here although it can be extended to three-dimensions. In this simple model of diffusion, we consider a diffusing trace amount of impurity or element (often referred to as the tracer) in a single-phase metal or alloy[66]. The volume density of the tracer can be given by;

$$C(x) = \frac{\sigma(x)}{\Delta x} \tag{1.21}$$

Where $\sigma(x)$ is the density of impurities in a plane given in (atoms m^{-2}) and where Δx is the separation of the planes. In general, we can assume that a molecule undergoing diffusion has neighbouring vacancies to which it can jump, we can further simplify the system by assuming that the tracer element is chemical identical to its surrounding atoms. This is the case for radioactive isotope tracers which remain distinguishable from their host atoms. We can define the flux of atoms that

move from a plane at position *z* to one at position $x + \Delta x$ as J_1 and the flux of atoms moving in the reverse direction as J_2.

$$J_1 = \frac{1}{2} v\sigma(x) \tag{1.22}$$

$$J_2 = \frac{1}{2} v\sigma(x + \Delta x) \tag{1.23}$$

Where ν is the average ionic jump attempt frequency and the factor of (1/2) represents the possibility of jumps being able to go in one of two directions; forward or back. As such the total flux *J* can be given by Fick's first law;

$$J = J_1 - J_2 = -D \frac{dC(x)}{dx} \tag{1.24}$$

Where D is known as the diffusivity and is given, in the one-dimensional case by with units of ($m^2\ s^{-1}$);

$$D = \frac{1}{2} v(\Delta x)^2 \tag{1.25}$$

The diffusion coefficient is the proportionality factor which links the rate of diffusion to a direction determined by the concentration gradient, which in qualitative terms implies that the mass of a substance diffuses through a unit surface in unit time for a given concentration gradient. The diffusion coefficient is dependent on several factors such as molecule size, temperature, and pressure as well as the properties of the diffusing species; it is often determined experimentally and is the most common figure quoted in literature on diffusion properties.

Fick's second law predicts how the diffusion process changes the concentration profile with time in a system. It arises from a combination of Fick's first law shown in Eq. 1.24 and the continuity equation shown in Eq. 1.26 which states that as particles cannot be created or destroyed any change in the concentration at a cross-section must be equal to the change in flux.

$$\left(\frac{\partial C}{\partial t}\right)_x = -\left(\frac{\partial J}{\partial x}\right)_t \tag{1.26}$$

Combining equations 1.24 and 1.25 gives us Fick's second law that states the change in concentration with time at some point on along a concentration gradient depends on the second derivative of that gradient.

$$\left(\frac{\partial C}{\partial t}\right)_x = D\left(\frac{\partial^2 C}{\partial x^2}\right)_t \tag{1.27}$$

The effect of strain on the change in the concentration profile can be expressed by a modification to the equation above by Pratt and Kröger et al. to include a term that accounts for the transport of matter due to strain gradients in the oxide[65].

$$\frac{\partial C(x,t)}{\partial t} = D\frac{\partial^2 C(x,t)}{\partial x^2} + \frac{D}{k_B T}\frac{\partial}{\partial x}\left[\frac{dU(x)}{dx}c(x,t)\right] \tag{1.28}$$

The findings accurately model observations of iron nanoparticles oxidising under ambient conditions in air over a period of up to two years which sees the particles evolve from cubic core-shell structures to fully oxidised spherical particles with central Kirkendall voids. However, such effects have yet to be observed in the more common spherical nanoparticles, this is likely due to the increased number of grain boundaries in such particles. It has been well established that atoms at grain boundaries are more mobile than those in a lattice with the difference in the diffusion coefficient being as large as 10 orders of magnitude for some materials and certain temperatures[67]. The effects of the diffusion along the grain boundaries may play a significant role in the diffusion of spherical nanoparticles, a similar role to that played by strain-effects in the oxidation of cubic nanoparticles.

It is also well known that the effect of diffusion along grain boundaries is increasingly dominant for materials at lower temperatures as diffusion through the lattice reaches very low diffusivities[46]. However, when temperatures are raised such that the diffusion through the lattice is non-negligible, this pathway will come to dominate the diffusion process. This is due to the small relative volume of the particle that is composed of grain boundaries compared to the lattice. A simplified model of grain boundary diffusion assumes that there are no fundamental differences between grain boundaries and the lattice[68]. Instead, the grain boundary may be treated as a lattice with a large number of vacancies that act as the main mechanism

behind diffusion. In this model the main difference between lattice and grain boundary regions is the activation energy for the initial diffusing 'jump' being much lower around grain boundaries than through the bulk lattice resulting in faster diffusion. The diffusion coefficient for grain boundaries is given by the Arrhenius' equation and has been well supported in practice by experiment[69].

$$D_i = D_{o_i} \exp\left(-\frac{Q_i}{kT}\right) \tag{1.29}$$

Where D_0 is the pre-exponential component, Q is the activation energy, k is the Boltzmann constant and T is the absolute temperature.

This model has been the prevailing mode of thinking since the 1970's and remains a good explanation of grain boundary diffusion today; computer simulations and experimental work have since evolved the understanding of how diffusion along grain boundary regions operates[70]. Diffusion along the grain boundaries of a material has been shown to occur through interstitial or substitutional mechanisms, not just vacancy diffusion. Furthermore, the rate of diffusion is heavily linked to the properties of individual grain boundaries with the grains structure, orientation and, energy having significant effects. It is likely that boundaries in a polycrystalline sample have their own diffusion coefficient and that the overall diffusion coefficient along grain boundaries is an average over the different grains in the sample.

It is useful to view diffusion in a polycrystalline sample as the combination of contributions of both lattice and grain boundary diffusion. These contributions are weighted by the respective volume fractions for a given particle. This leads to the effect where despite their relatively low fraction, the lower activation energy for diffusion around grain boundaries leads to increased diffusivity at low temperatures; resulting in a grain boundary dominated mechanism. When describing the effective diffusion coefficient D_{eff} two main interpretations exist, the first is to over-estimate the effective coefficient by assuming that the processes for lattice and grain boundary can be combined in parallel. This leads to Hart's equation[71].

$$D_{eff} = gD_{gb} + (1 - g)D_l \tag{1.30}$$

Where g represents the volume fraction and is equal to $3\delta/d$, where δ is the grain boundary width which is approximated through experiment to be 0.5nm and d

is the average grain size. D_l and D_{gb} represent the diffusion coefficients for the lattice and grain boundaries respectively. This equation assumes that all boundaries are in parallel, as such it provides an upper limit to the effective diffusion coefficient while the series combination provides the lower limit such that.

$$D_{eff} = \frac{D_{gb}D_l}{gD_{gb} + (1-g)D_l} \tag{1.31}$$

Hart's equation has the advantage of being simple and understandable, providing an upper limit on the effective diffusivity. Importantly, as the atomistic mechanisms behind grain boundary are still controversial, it is useful to be able to provide a concrete upper estimate. However, experiments have shown that the best estimate to the effective diffusivity is not to treat the polycrystal as either a parallel or serial arrangement of grains but as an effective medium approximation using the Maxwell-Garnett equation[72].

$$D_{eff} = \frac{D_{gb}[2gD_{gb} + (3-2g)D_l]}{(3-g)D_{gb} + gD_l} \tag{1.32}$$

Where all the variables retain the same meanings as in Hart's equation. This approach is the method best supported by computer simulation and experiment. Furthermore, at low temperatures where the difference in the diffusivities is such that $D_{gb} >> D_l$ and when the volume fraction becomes large then both the Hart and Maxwell-Garnett equations can be approximated as;

$$D_{eff} \approx gD_{gb} = \frac{3\partial}{d}D_{gb} \tag{1.33}$$

and

$$D_{eff} \approx \frac{2g}{3-g}D_{gb} = \frac{2\partial}{3-d}D_{gb} \tag{1.34}$$

This allows for the estimation of the grain boundary diffusion coefficient for the sample, as the effective diffusion coefficient can be inferred empirically by comparing the decrease in the size of the iron core during heating and considering the amount of iron core material that must out-diffuse to account for this. In addition to this, the average grain size of the particles can be measured in HRTEM and

HRSTEM using the Fourier Filtering and analysis of the image's FFT. As mentioned before, the grain boundary width was estimated as 0.5 nm which is supported in the literature[73]. The value for the diffusion coefficient is often determined empirically from ln(*D*) vs 1/*T* plots.

As a follow-on from these observations, this study aims to investigate the effect on the diffusion of similar nanoparticles caused by the presence of grain boundaries. This is important for the overall picture of nanoparticle diffusion as the more commonly found spherical particles have many grain boundaries, although the cubic particles in the aforementioned studies showed mostly mono-crystalline side facets which imply a low presence of grain boundaries.

1.4.4 Coating of Metal Nanoparticles

The materials selected for the use as nanoparticles optimised for biomedical applications are required to have strong magnetic properties, this is due to the limitations regarding the use of magnetic fields in medical environments as described previously. When a magnetic material is exposed to a magnetic field with strength ***H***, the magnetic induction is given by;

$$B = \mu_0(H + M) \tag{1.35}$$

Where μ_0 is the permeability of free space, ***M*** is the magnetisation where $M = mN/V$ with ***m*** representing the atomic magnetic moment and ***N/V*** the number of atoms per unit volume.

The magnetism of a material is derived through the magnetic moments of the electrons and originates from their orbital motion and spin. All materials are magnetic to some degree with their magnetic responses being classified in terms of their magnetic susceptibility χ where;

$$M = \chi H \tag{1.36}$$

Which describes the magnetisation induced by a magnetic field ***H***. The susceptibility is dimensionless, and most materials have low values between 10^{-6} and 10^{-1}[74] and even then, only in the presence of a magnetic field. These materials are

classified as paramagnetic or diamagnetic depending on the origin of their magnetisation. In the case of diamagnetic materials, the magnetic response arises from the distortion of orbiting electrons such that a weak field is produced in opposition to the external magnetic field. This response is very weak and only significant in materials with no permanent magnetic moment. In the case of paramagnets, the magnetic response arises from the aligning of the material's magnetic moments within the external magnetic field. When the magnetic field is removed the net magnetisation of the material returns to zero, due to the random orientation of the atomic moments within the sample.

The most useful magnetic materials are those with the ability to maintain their magnetisation without the presence of a magnetic field. These materials are classified as ferromagnetic, ferrimagnetic or anti-ferromagnetic depending on the nature of the alignment between the spins in the material. The advantage of these materials is this coupling gives rise to very high susceptibilities which allow for very high magnetic responses even in relatively small magnetic fields. The susceptibility in ordered materials is a function of temperature such that;

$$\chi = \frac{C}{T} \tag{1.37}$$

Where $\boldsymbol{C}$ is the Curie Constant and $\boldsymbol{T}$ is the temperature. The susceptibility is also dependent on the field strength $\boldsymbol{H}$ as shown previously and this gives rise to the characteristic sigmoidal *M*-*H* curve where $\boldsymbol{M}$ approaches a saturation point at a large value of $\boldsymbol{H}$.

The explanation for this effect is that the magnetic moments/spins in ferromagnetic, ferrimagnetic and antiferromagnetic materials order themselves in such a way that domains are created. A magnetic domain is a region of a material in which the magnetic moments of the individual atoms in the region align in a uniform direction. Domains form in magnetic materials as a way for the material to minimise its internal energy (magnetic self-energy). The formation of domains is limited by the creation of domain boundaries associated with the formation of a new domain, the domain boundaries represent areas of increased exchange energy. As such there will reach a point where the increased energy from domain boundaries balances out the energy minimised through the formation of a domain. This effect is important as

it infers a critical size for domain boundary formation. In fact, it has been observed that nanoparticles; which go below this size exhibit superparamagnetic behaviour. This occurs because at the macroscopic scale magnetic materials are formed of several randomly oriented domains, while at the nanoscale the number of domains in a particle is very small. If the particle's size goes below the critical size for domain formation, then it will become energetically-favourable for the particle to become a particle with only a single domain. The size of superparamagnetic particles tends to be of the order of ~1nm to ~10nm[15].

In ferromagnetic materials there is a splitting of the materials magnetic behaviour at the Curie Temperature T$\boldsymbol{c}$ where below this temperature the material acts as a ferromagnet and above the temperature the material exhibits paramagnetism. This is due to thermal fluctuations overcoming the ordering of the magnetic moments resulting in a disorder of the magnetic moments. A similar transition occurs in a superparamagnet described by the Néel relaxation time τ_N. This represents the average time for the magnetic moment to flip between the two stable antiparallel orientations and is given by;

$$\tau_N = \tau_0 \, exp\left(\frac{\Delta E}{kT}\right) \tag{1.38}$$

Where $\boldsymbol{\tau_0}$ represents the pre-exponential factor (usually ranging between 10^{-9} and 10^{-11} s) and ΔE represents the energy barrier that must be overcome. Superparamagnetism is desirable as the particles do not exhibit any hysteresis and display no magnetic memory after the external magnetic field is removed. This makes them very interesting in applications where directing or targeting is a requirement. It should be noted, however, that typically superparamagnetic particles have lower induced magnetisation than ferromagnetic materials do.

It is clear, therefore that iron nanoparticles represent a very interesting and useful material for use in medical applications as the magnetic response of ferromagnetic materials is very large. The challenge arises due to the near instantaneous oxidation that iron will undergo once exposed to oxygen, this process is highly undesirable because, as mentioned, there are strict limits on the strength and frequency of the magnetic fields allowed and as such particles must be functionalised to provide the best magnetic response within these limits. Of the

stable oxides of iron wüstite is unstable at temperatures below 500K but both maghemite and magnetite (γ-Fe_2O_3 and Fe_3O_4) are ferrimagnetic while hematite (α-Fe_2O_3) is anti-ferromagnetic below 250K above which it is weakly ferromagnetic. In all cases except the latter the formation of oxide will serve to limit the magnetic response of the particles. One potential way around this is to coat the iron cores during deposition (before the formation of their initial oxide layers) with a protective coating that is either resistant to oxidation or whose oxides do not have a strong effect on the overall magnetism of the particle. The metal coating materials attempted in this study include; copper, silver, aluminium, and magnesium.

Copper

The motivation behind the usage of copper as a shell material stems from its previous successful use in core-shell particle deposition[75]. Where the presence of copper in the iron-metal nanoparticle system was inferred due to the increase in cluster size observed before and after the iron clusters preceded through the shell-evaporator region. This indicates a degree of copper uptake onto the iron clusters, however, the exact nature of the uptake; such as the location of the copper and degree of alloying could not be determined. These early indications however, make the use of copper a convenient test case to see if such core-metal nanoparticles can be produced.

One important factor to consider is the lattice misfit between the two desired materials. A small lattice misfit is important for the growth of one material upon another; in this case copper on iron. The concept of lattice misfit is most often used in regard to epitaxial growth and is determined by comparing the lattice parameters of the two materials in question. For example, when depositing one material upon another (the substrate) the perfect case would be for the coating material to match perfectly with the lattice from the substrate and simply continue that lattice structure as it is deposited.

Practically even small degrees of misfit influence the final shell structure, with the degree of misfit calculated using the expression;

$$f = \frac{(a_A - a_B)}{a_A} \tag{1.39}$$

Where a_A and a_B are the lattice parameters for the two respective materials. In the case of materials where the lattice mismatch is small ≈10% it is possible for the material to maintain the lattice structure of the substrate; however, the deposited material will need to either slightly stretch or contract its own lattice structure to accommodate and this will result in the building up of strain energy in the lattice. This stress and strain energy intuitively scales with the thickness of the deposited material until a critical thickness is reached in which it will become energetically favourable for misfit dislocations or other methods of relieving the strain to occur. This critical thickness is given by the expression;

$$d_{crit} = \frac{b}{9.9 \cdot f} \tag{1.40}$$

Where b is the Burgers vector and f is the lattice misfit. As such when this the critically limit is plotted against the lattice misfit we find that even for very small misfits of 1% the critical shell thickness for dislocation formation is only ≈4nm.

In the context of the Fe@Cu material system the misfit is 26% between α-Fe (BCC) and Cu, while being <1% between γ-Fe (FCC) and Cu. As such depositing a copper film onto the iron clusters is expected to produce either highly strained metallic shells or else a large number of defects.

In terms of copper's magnetic suitability as a shell, the material is diamagnetic with a mass magnetic susceptibility of -1.08×10^{-9} m^3/kg compared to ferromagnetic iron and as such will have little overall impact on the magnetic applicability of the iron particle. This is desirable, as the high magnetic response of pure α-iron is needed for the material system to function well in its intended setting. In terms of oxidation, copper has two stable oxides; Copper(I) Oxide (CuO_2) and Copper(II) Oxide (CuO). CuO_2 is formed through exposure of copper to air through the reaction;

$$4\,Cu + O_2 \rightarrow 2\,Cu_2O \tag{1.41}$$

Like bulk copper the material is diamagnetic and therefore ideal as a shell material from a magnetic point of view. On the other hand, CuO_2 is formed by

heating copper in air at temperatures between 300°C and 800°C, the material is paramagnetic which like diamagnetic materials should not have a significant effect on the overall magnetic response when compared to the ferromagnetic iron core.

Another possibility is that deposition of copper onto the iron clusters will lead to the alloying of the iron and copper at the surface, this could have interesting effects as the higher than normal surface-to-volume ratio that makes nanoparticles uniquely interesting also implies that a larger proportion of the particles overall magnetic activity will be influenced by the surface atoms. If these same surface atoms are alloyed with copper, the effects could influence the overall magnetic properties to a significant degree, as the magnetic behaviour of Fe-based alloys is more complex than the behaviours of the other ferromagnetic elements, Co, and Ni. In general, the alloying effect on the magnetic behaviour of transition metals such as Co and Ni are well understood by the Friedel's Theory, but in the case of Fe-based alloys it has been found that the magnetic moment of the alloy reduces sharply as the Fe content of the alloy changes. This is attributed to the fact that the majority spin-band in Iron is not filled and so more open to perturbation upon alloying. One notable exception however is the case of the FeCu alloy, which displays a constant magnetic moment when alloyed with α-Fe. While the alloy maintains a high degree of Fe content (>75%) then the iron will retain its BCC crystal structure and magnetic moment. As more copper is introduced to the material the iron will shift to γ-Fe and a FCC structure, which will reduce the magnetic moment of the material. This phase shift occurs at roughly 60% iron content. As such even if a degree of alloying occurs at the surface it is possible that the iron nanoparticle will retain much of its desirable magnetic properties making even the alloyed material system a particularly interesting area of study.

With this said however, it is important to highlight that both copper oxides (CuO) and (CuO_2) are bio-incompatible, with studies having highlighted major problems with the environmental impact of copper oxide nanoparticles[76]. Therefore, such materials will need to be coated with biocompatible films before use in any biomedical application. The coating of both iron and non-iron nanoparticles has been studied in great detail and is beyond the scope of this study. The main aim of this study is to investigate the feasibility of iron-metal nanoparticles by determining if the shell material is present in the particles and to what extent the deposition properties

such as temperature affect the characteristics of the particles; size, shape, shell thickness for example.

Chapter 2: TEM Techniques

This chapter will cover the different techniques available in both scanning transmission electron microscopy (STEM) and transmission electron microscopy (TEM). The techniques discussed will cover only those directly applicable to the characterisation of the iron-based nanoparticles, as TEMs of all types provide many possible characterisation techniques and not all will be used in this study.

Firstly, there will be a general discussion of overall TEM theory covering how signals are generated, along with a brief description of the two microscopes used in the study. Following this, each technique will be presented separately with a discussion of the theoretical background and how it is used for characterisation in this study. The techniques used and covered are:

- Bright-Field imaging (BF) and Dark-Field imaging (DF)
- High-Resolution imaging (HRTEM) and (HRSTEM)
- Energy-Dispersive X-Ray Spectroscopy (EDX)
- Selective-Area Electron Diffraction (SAED)

Following this, there will be a description of the sample preparation method, this will include a description of the cluster source and the background theory regarding the formation of low-energy nanoclusters. Lastly, there will be a discussion behind the design of the heating and coating experiments that have been carried out in this study, here a description of the sample preparation parameters for each experiment will be presented.

2.1 Introduction to Electron Microscopy

The use of electrons as an imaging tool has many benefits, the most important being that they allow for resolutions much smaller than those achieved by the best visible light microscopes (VLM).As techniques in electron microscopy developed, it was realised that electrons possess several other benefits, such as the production of many types of secondary signals that can be used alongside or as stand-alone techniques to gather chemical, structural and physical information from samples[77]. However, the main benefit of electron microscopy, namely the ability to resolve increasingly smaller objects, the idea can be best demonstrated by considering the Rayleigh criterion for a VLM. The Rayleigh criterion represents the smallest distance that can be resolved using a given light source.

$$\delta = \frac{0.61\lambda}{\mu \sin \beta} \tag{2.1}$$

Where λ is the wavelength of the radiation, μ is the refractive index of the medium through which the object is being viewed and β is the semi-angle of collection for the lens. As such, a good estimate for the resolution limit of a green light VLM (λ ~ 550nm) is about 300nm which corresponds to a particle of roughly 1000 atoms in diameter. To probe smaller diameters a better radiation source is needed. Through De Broglie's theory that electrons, and indeed all particles, have wave-like characteristics, we can estimate the wavelength of the electron in a TEM (note that relativistic effects must be considered as, the electrons' velocities exceed 0.5c where c is the speed of light)[78]. Using De Broglie's wave-particle duality we can relate the particles wavelength to its momentum such that

$$\lambda = \frac{h}{p} \tag{2.2}$$

Furthermore, due to the law of conservation of energy, the electron, as it is accelerated through a potential, must gain kinetic energy equivalent to that imparted to the scattering electron inside the TEM, and that the momentum can be related to the particles mass we obtain;

$$eV = \frac{m_0 v^2}{2} \tag{2.3}$$

and

$$p = m_0 v = (2m_0 eV)^{1/2} \tag{2.4}$$

Equations 2.2, 2.3 and 2.4 can be combined to give Eq. 2.5 which has been modified for relativistic effects[79].

$$\lambda = \frac{h}{\left[2m_0 eV\left(1 + \frac{eV}{2m_0 e^2}\right)\right]^{1/2}} \tag{2.5}$$

Therefore, for an accelerating voltage of 200V, the voltage used by the microscopes in this study the resolution limit determined through the equations 2.1 and 2.5 is δ ~ 4pm, which is many times smaller than the diameter of an atom. It is worth noting however, that this limit has never been reached in practice and is unlikely to be approached in the near future, due to the quality of current electron lens; the current best TEM microscopes are able to achieve resolutions on the sub-ångstrom level (<0.1nm [80]). This sub- angstrom resolutions are achievable due to the advances made in aberration correction, the JEOL 2200 FS in this study is one such microscope.

Electrons are a type of ionising radiation, this means that they can remove tightly bound inner-shell electrons by imparting some of the electron energy to a specimen's constituent atoms. While this can lead to complications regarding specimen damage (particularly when higher accelerating voltages are used, or on more sensitive samples) it does possess the benefit of producing a variety of secondary signals which can be used as analytical tools to provide a great level of insight into a specimen [81]. A schematic of some of the signals produced in a TEM is given in Fig. 2.1.

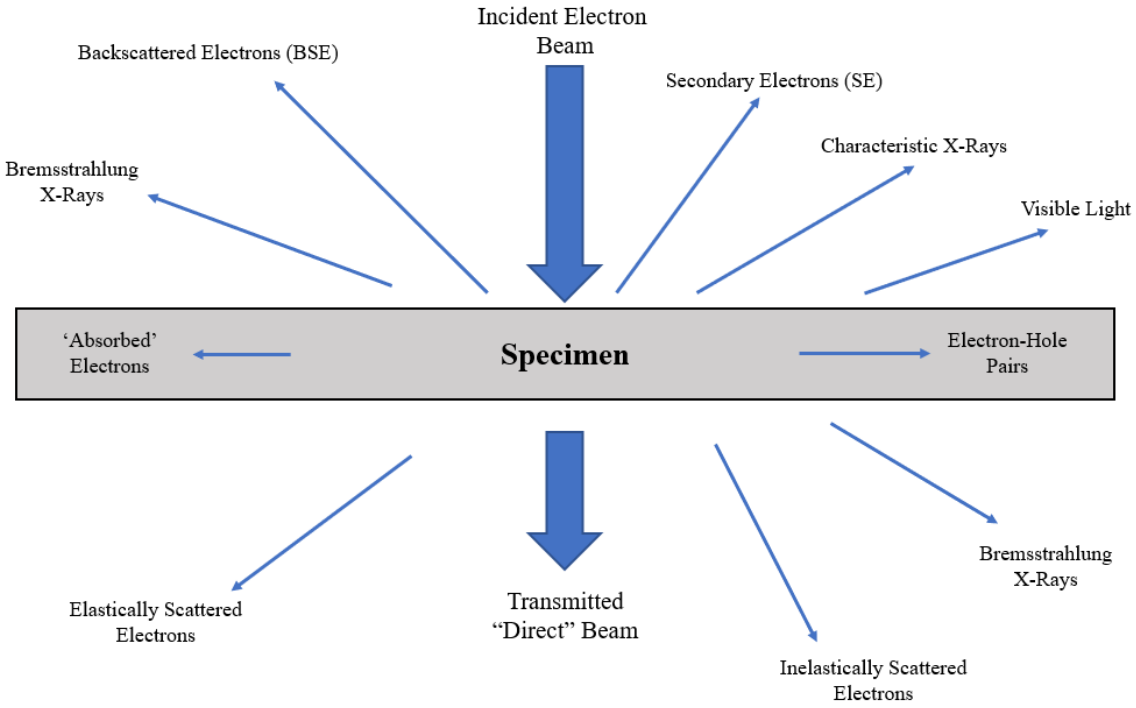

Figure 2.1 Schematic diagram of signals generated due to the interaction of the incident electron beam with a thin specimen. Most signals may be detected in a TEM with the appropriate detector, the direction of the arrow indicates the general direction of the signal; either back away from the specimen or transmitted through it.

The most common form of 'interaction' between the electron beam and the sample is for the electron to pass through the sample without undergoing any noticeable scattering or interaction. This occurs because the effective size of the electron is many orders of magnitude smaller than the characteristic sizes of atoms and the spacings between them, as such, from the perspective of the electron, the specimen is largely empty space. Electrons that pass through the sample in this manner form the direct beam. The direct beam can also contain electrons that have undergone plural or multiple scattering in such a way that their trajectories have realigned with the direct beam as shown in Fig. 2.2 [82]. This is a highly undesirable event due to the complications it causes for image interpretation, which is heavily dependent on understanding the scattering processes each electron has undergone. This leads to the requirement that TEM samples be very thin films to reduce the chance of a single electron undergoing multiple scattering events.

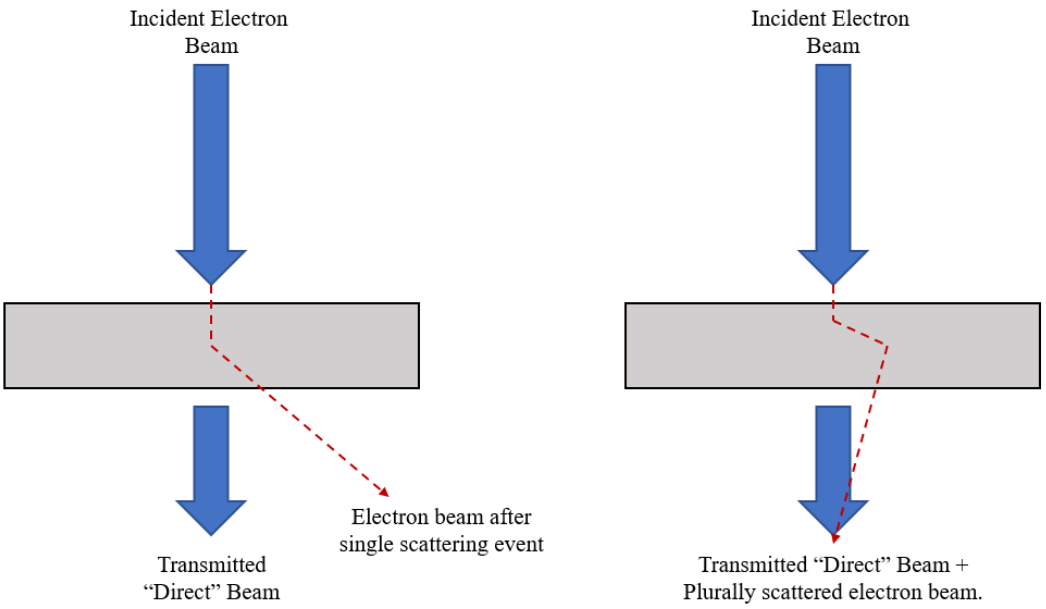

Figure 2.2 Schematic of electron scattering in a thin specimen, for resulting images to be interpretable only single scattering events should be occurring in the specimen. This is achieved by thinning the specimen. The thicker the specimen the greater the possibility of plural or multiple scattering events to occur resulting in potential for scattered electrons to make up signal from the direct beam (scattered electrons) or other scattered beams than the one corresponding to the original scattering event.

For electrons that interact with the specimen and are deflected from their original trajectory, interactions can be split into two rough categories: signals produced due to elastic interactions and those produced through inelastic interactions. Elastic interactions are characterised by zero or negligible energy transfer between the electron and the sample. These events occur due to deflection via Coulomb interactions. Electrons scattered in this way are often coherent, meaning they are in phase with each other and scatter at relatively low angles between 1° and 10°. However, as the scattering angle increases, the chance of incoherent scattering increases. These elastic interactions are often used in imaging, as their scattering angle is heavily dependent on the atom with which the electron interacted[83].

The case where energy is transferred between the incident electron and the specimen, inelastic scattering occurs; this type of scattering is almost always incoherent and occurs at very low scattering angles (<1°). Furthermore, the energy

imparted by the electron will cause a variety of secondary signals such as x-rays, Auger electrons, or secondary electrons.

X-rays are produced through inelastic scattering, when an unexcited ground-state atom within the sample has an inner-shell electron excited by the electron beam. Upon de-excitation, the excited electron, or another outer-shell electron fills the vacant hole in the inner shell, and an x-ray will be produced with an energy equal to the energy difference between the two atomic shells. As the relationship between atomic shells is unique to each atom, these x-rays, once detected with a spectrometer, can be used to chemically identify the atoms in a sample; this forms the basis of EDX, which will be described in more detail later[79]. Another useful spectroscopic signal is the emission of electrons from the outer shell due to the Auger effect, this is when the incident electron beam ejects an electron completely from the inner atomic shells which is subsequently filled by an outer-shell electron. The energy required for the outer-shell electron to fill the vacancy will cause the ejection of a second outer-shell electron, if the energy drop is greater than the binding energy. This effect was originally considered a nuisance effect, but has since become a powerful tool for generating high-resolution chemical information from a specimen with specially designed Scanning Auger Microscopes (SAMs)[84].

Secondary and back-scattered electrons signals form the back-bone of Scanning Electron Microscopy (SEM), which is a very commonly used technique to probe surface information of materials. Back-scattered electrons arise when an electron undergoes strong Coulomb interaction after passing close to a nucleus, but instead of being merely diverted, they are deflected at a very large scattering angle. These events are much rarer than forward elastic scattering, such as that which makes up the direct beam, and are strongly dependent on the atomic number Z, with heavier atoms producing more back-scattered electrons, with most back-scattered electrons coming from surface regions. The number of back-scattering events also decreases with increasing accelerating voltage as faster electrons are less likely to be deflected from their original paths. Secondary electrons are produced when loosely bound outer-shell electrons are liberated from their parent atom by an inelastic scattering event and are used to in SEM to generate a high-resolution signal combining spatial resolution with characteristically shallow sampling depth making them a useful surface-probing signal [85].

Despite these many advantages, there are drawbacks to the use of electron microscopy as a characterisation tool. The most evident drawback is that with any higher-resolution imaging method, the area of a sample that can be realistically imaged is very small. Therefore, drawing overall conclusions about a sample can be problematic if the area sampled in the TEM is not representative of the sample as a whole. As such, it can be useful to combine TEM with lower-resolution techniques such as VLM or SEM which offer better sampling abilities.

Another major issue with TEM images, is the interpretation of the 2D images provided as 3D structures. As the images are also viewed in transmission it can be difficult to draw conclusions about the overall structure of the particles or specimen being imaged. This is because the TEM may be able to resolve neighbouring features, depending on the microscopes point-resolution, however, features that are stacked on top of each other will be resolved incorrectly as a single feature. As such it is necessary to interpret TEM images with the aid of accompanying characterisation techniques such as EDX, EELS or Auger spectroscopy, SEM, or Electron Tomography.

Sample preparation of TEM specimens must also be considered as, for a sample to be imaged properly in a TEM, it must be thin (usually a specimen thickness of <100nm is considered appropriate) however thicker samples can be used. This thickness limit is to ensure that the specimen remains ‘transparent’ to electrons, and that enough electrons will be transmitted to produce a resolvable signal. How thin a sample must be is dependent on the electron energy (higher energy results in deeper penetration, but has its own drawbacks) and the atomic number Z of the specimen; in the case of very high-resolution TEM imaging (HRTEM), a sample may need to be as thin as 10nm. There are a number of sample preparation methods that offer varying degrees of control over the thickness of the specimen, often requiring a compromise with the difficulty or time investment in preparing a sample and the desired thickness. The samples for this study were produced using a physical vapour deposition technique explored in detail in Chapter 3.

The final consideration is the potential for damage to the sample when used in a TEM as electrons function as ionising radiation, which can result in damage, especially to samples such as polymers and organic specimens. Damaging effects are

also increased with increased accelerating voltages, with some specialist TEMs capable of voltages of the order of MeV only capable of imaging very specific materials [86].

2.2 Electron Diffraction and Scattering

An understanding of the theory behind the scattering events is essential to be able to characterise and identify the types of electronic scattering and signals which will be encountered while performing STM of any type. Here, we consider both the elastic and inelastic scattering events. In the case of elastic events, electrons are scattered through interaction with atoms or planes of atoms through the Coulomb interaction as shown schematically in Fig. 2.3. The number of electrons scattered through any given angle is proportional to effective area of the scattering body (often called the differential scattering cross-section). The cross-section for scattering due to the atomic nucleus is given by the Rutherford scattering cross-section in Eq. 2.6 [87]

$$\sigma_r(\theta) = \frac{e^4 Z^2}{16(4\pi\varepsilon_0 E_0)^2} \frac{d\Omega}{sin^4\left(\frac{\theta}{2}\right)} \tag{2.6}$$

Where e is the electron charge, Z is the atomic number, E_0 is the energy of the particles which are scattered through angle θ into a solid angle Ω. In general, the cross-section used is dependent on the type of scattering being observed, the Rutherford cross-section ignores low-angle electron-electron scattering and must be modified to account of screening and relativistic effects. The screened, relativistic differential Rutherford equation is shown in Eq. 2.7 and has the benefit of not going to infinity as the scattering angle tends towards zero[79].

$$\sigma_R(\theta) = \frac{\lambda_R^4 Z^2}{64\pi^4 a_0^2} \frac{d\Omega}{\left[sin^2\left(\frac{\theta}{2}\right) + \frac{\theta_0^2}{4}\right]^2} \tag{2.7}$$

Where a_0 is the Bohr radius of the scattering atom and θ_0 is the screening parameter. The Rutherford scattering cross section allows us to predict the

distribution of scattering angles for an electron beam, with the cross-section decreasing as the scattering angle approaches 180°. Therefore, scattering in thin samples is heavily forward peaked. Increasing the atomic number of the scattering atom increases the cross-section across all angles, as such thinner samples are needed when examining heavy elements in the TEM. Furthermore, increasing the beam energy decreases the scattering cross-section as the faster electrons have less 'contact' time within the interaction range of the atom.

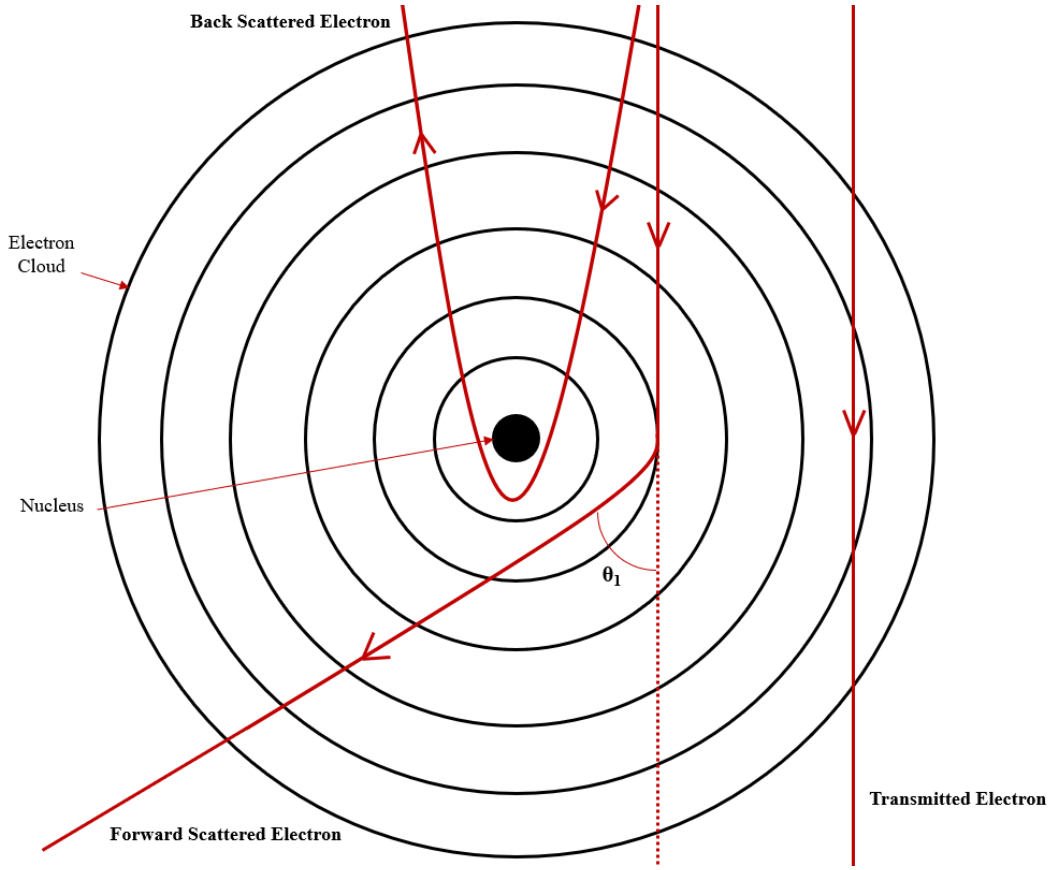

Figure 2.3 A schematic diagram of high-energy electron scattering of a single isolated atom, Coulomb interaction within the electron cloud leads to low-angled scattering while interaction with the nucleus leads to high-angle scattering and potentially back-scattering.

As the scattering cross-section is heavily dependent on both the properties of the beam, that can be well defined, and the atomic configuration of the sample, the resulting patterns can be analysed and indexed to provide a wide variety of crystallographic information about any given sample. The most common method of doing this is by comparing the patterns made by the scattered beams due to a specimen with known patterns for given materials. These diffraction patterns appear as images consisting of 'spots' with varying intensity and size in a pattern around some central maxima an example of which can be seen in Fig. 2.4.

The position and pattern of the diffraction spots can be explained by expanding the atomistic scattering model talked about previously to consider the scattering of the electron beam from a plane of atoms in a crystal. In this way the spacing between the atoms in a crystal can be thought of as a diffraction grating where the wavefront **K** is diffracted by an atomic plane. The subsequent diffracted beam will appear as a point in the diffraction pattern if the atoms are scattering electrons in phase with each other. The angle at which diffraction points appear in a diffraction pattern is given by Bragg's Law while the criteria for determining if individual scattered waves are in phase is the Laue condition[88].

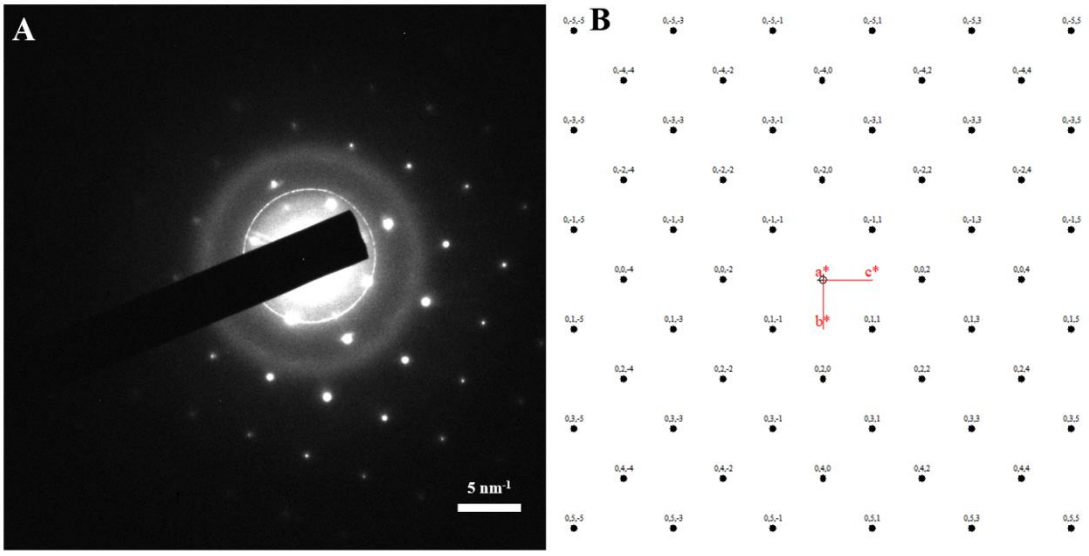

Figure 2.4 A) SAED diffraction pattern from a Fe/Fe_xO_y nanoparticle, bright ring is likely due to oxide grains, B) simulated diffraction pattern for α-Fe along the (100) zone axis.

Bragg's Law can be derived by considering the path difference of the incident and diffracted beams such that the difference in the wavevector **K** is

$$\Delta K = k_D - k_I \tag{2.8}$$

Where k_D is the diffracted wavevector and k_I is the incident wavevector, this gives us the scattering angle.

$$\sin(\theta) = \frac{|\Delta K|/2}{|k_I|} \tag{2.9}$$

$$|\Delta K| = |k_D| = |k_I| = \frac{1}{\lambda} \tag{2.10}$$

Combining the equations 2.9 and 2.10 we can derive an expression for the scattering angle when the path difference is a whole number of wavelengths (corresponding to constructive interference), as this is the position of the scattering maximum.

$$k = \frac{2\ \sin\theta_B}{\lambda} \tag{2.11}$$

If there are only two planes of atoms contributing to the diffraction, then there would be a gradual transition between constructive and destructive interference with a maximum at the Bragg angle. In real crystals however, there are many contributing atomic planes resulting in very sharp peaks of constructive interference; the diffraction 'spots' surrounded by mostly destructive interference. This is what gives rise to the diffraction patterns observed in TEM, furthermore, as the atomic spacing is unique to each crystal, the diffraction pattern for each pure crystal will be unique, allowing comparison between specimens and 'ideal' patterns. As such it is possible to determine the composition of a sample through its diffraction pattern.

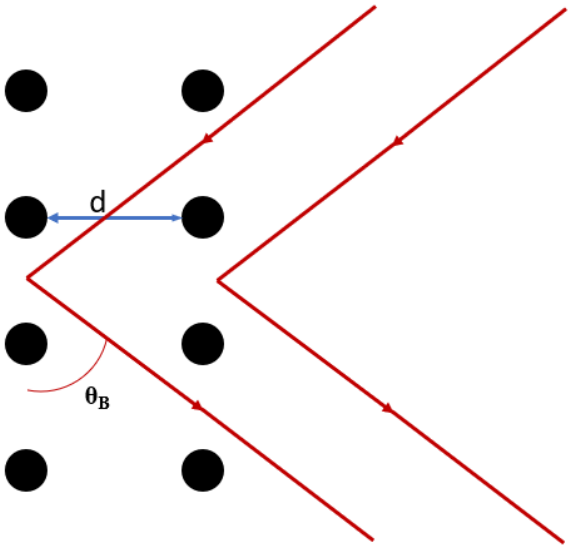

Figure 2.5 Schematic diagram depicting the scattering from two points on two different lattice planes separated by a spacing *d* the beams will constructively interfere when the path difference is an integer number of wavelengths such that $2d \sin\theta = n\lambda$.

The intensity and size of a diffraction spot can be determined through the structure factor $F(\theta)$, which is a measure of the amplitude of a wave scattered by a unit cell in a crystal. As the structure factor is unique to the unit cell in question, it provides additional crystallographic information that can be used in conjunction with the diffraction pattern to index scattered beams and identify materials. The structure factor can be expressed as the product of the atomic scattering factors $f(\theta)$ from all the atoms in the unit cell and the phase factor. The atomic scattering factor is a measure of the amplitude of an electron wave scattered by an individual atom and is given by[79].

$$|\mathrm{f}(\theta)|^2 = \frac{d\sigma(\theta)}{d\Omega} \tag{2.12}$$

When Eq. 2.12 is combined with the scattering cross-section the atomic scattering factor is given by.

$$\mathrm{f}(\theta) = \frac{\left(1 + \frac{E_0}{m_0 c^2}\right)}{8\pi^2 a_0}\left(\frac{\lambda}{\sin\frac{\theta}{2}}\right)^2 (Z - f_x) \tag{2.13}$$

Where λ is the wavelength and f_x is the scattering factor for x-rays with all other variables having been previously defined. Lastly, the phase factor takes into account the difference in phase between scattered waves due to different but parallel planes of atoms. As such the structure factor can be expressed as.

$$\mathrm{F}(\theta) = \sum_i^{\infty} f_i e^{2\pi i(hx_i + ky_i + lz_i)} \tag{2.14}$$

The amplitude and by extension the intensity of the diffraction spot due to the scattering of a plane of atoms with the Miller index (hkl) can then be calculated allowing for the simulation of diffraction patterns for ideal crystals and the indexing of unknown specimens through comparison to these simulations.

2.3 Bright and Dark Field Imaging

Generating images in both STEM and TEM is performed by selecting a scattered beam of electrons and constructing an image based on the information provided by that beam. In the case of bright field imaging (BF) the direct beam is selected, and the objective aperture is used to exclude any scattered beam. As such, the image generated has increased intensity in regions where the number of transmitted (non-scattering) electrons is higher and will have dark regions that correspond to scattering centres from the sample. The term bright field is taken from the fact that the 'background' region will have the largest intensity while the features in the sample (particles etc.) will appear dark. Conversely, in dark field images the image is constructed using one of the scattered beams, with either the objective aperture positioned to exclude the direct beam and other scattered beams, or the beam is tilted to provide the same effect[89]. This will result in an image where the highest intensity features correspond to areas in the sample which scattered electrons at the chosen angle, with the background and features that scattered electrons at

different angles being dark. Bright field images have the general advantage of showing all the features of a specimen as dark regions as all scattered beams will be represented in the image. Dark field (DF) images however offer better contrast distinctions, as only electrons scattered at the given angle will contribute to the image, however not all features can be included in the same image. This limitation is lifted somewhat in STEM where an annular dark field detector can be used to create an image summed over all the scattering angles.

The images can both be understood in terms of intensity and contrast where the former is defined as the number of electrons per unit area, regions of high intensity will appear brighter in the image representing a greater number of electrons being either transmitted (in the case of a BF image) or scattered (in the case of a DF image). Contrast is the difference in intensity between two adjacent areas and can be expressed as shown in Eq. 2.15[79].

$$c = \frac{(I_2 - I_1)}{I_1} = \frac{\Delta I}{I_1} \tag{2.15}$$

Because contrast is how features can be distinguished in an image, it is important to understand the types of contrast produced in a TEM or STEM and their causes. The two basic forms of contrast primarily associated with electron images will be discussed below, with the two forms mostly concerning the production of high-resolution atomic imaging discussed in section 2.4. The method of creating bright and dark field images in both TEM and STEM is shown schematically in Fig. 2.6.

2.3.1 Mass-Thickness Contrast

The overall term given to the contrast used to form bright and dark field images is amplitude contrast, which results from any variation in either the thickness of a specimen or the mass of the atoms. The former results in more atoms interacting with the sample thereby changing the intensity and the contrast at a given position, while the latter results in a change in the interaction cross-section resulting in more scattered electrons as discussed previously. Mass-thickness contrast results from

incoherent elastic scattering (Rutherford scattering) of the kind previously discussed[83]. As was shown in Eq. 2.6 the Rutherford scattering cross-section is a function of the atomic mass and specimen thickness. As scattering in a thin specimen is heavily forward-peaked this often includes electrons scattered through angles of less than ~ 5°. Mass-thickness contrast is an important mechanism in the study of non-crystalline materials such as polymers and organic specimens[90].

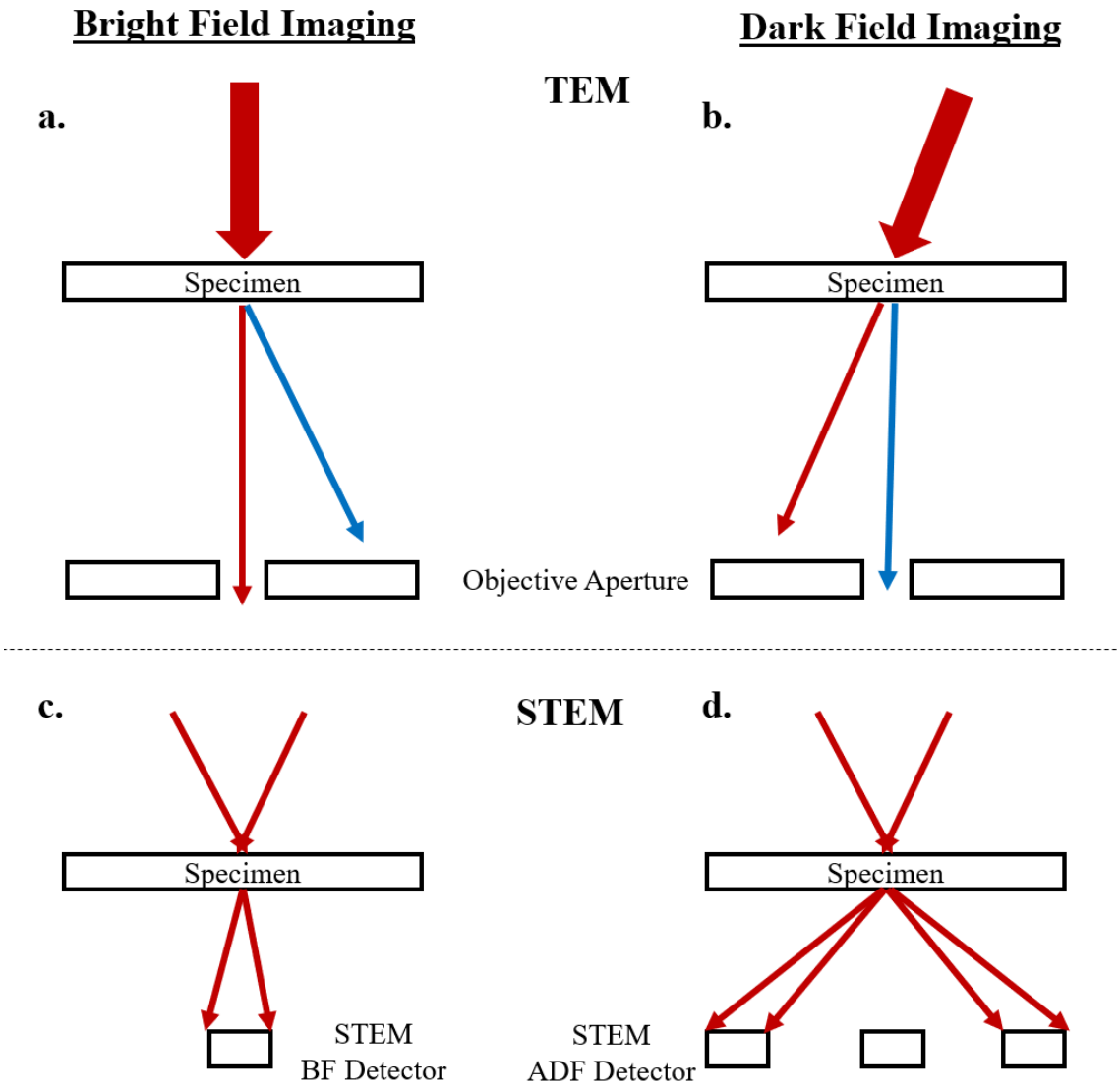

Figure 2.6 Schematic diagram showing the production of bright field images in a) TEM and c) STEM and the production of dark field images in b) TEM and d) STEM.

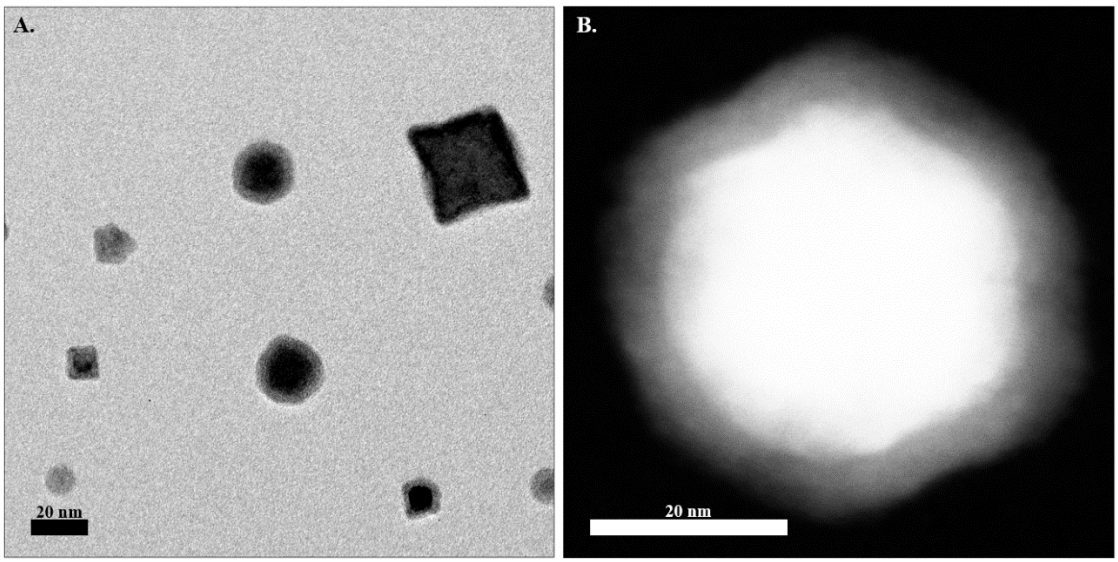

Figure 2.7 Example TEM images of iron nanoparticles with iron oxide shell in A) bright field and B) dark field.

For instance, in the case of an iron core-shell nanoparticle the iron core with its atoms arranged in a BCC structure would have a density of 2.4039 amu Å-1 while the iron oxide in the shell (assuming the phase was magnetite) would have a density of iron atoms of 0.3912 amu Å-1. While this does not account for scattering from the oxygen atoms in the magnetite structure it demonstrates the expected reduction in contrast that would be observed between the iron core and oxide shell due to the lower density of iron in the shell and oxygen being a very weak scatter by comparison. This can be seen clear in the iron core-shell particles in Fig. 2.7.

2.3.2 Bragg (Diffraction) Contrast

Contrast due to Bragg diffraction occurs in both TEM and STEM images and is the dominant contrast mechanism, particularly at lower magnifications[91]. Diffraction contrast is a form of amplitude contrast where scattering at the Bragg angles (Section 2.2) is stronger. This leads to greater intensity in the parts of an image corresponding to electrons scattered in this manner. While any diffracted beam may be used to form an image using mass-thickness contrast, the beam must be carefully selected to produce the strongest diffraction contrast. This occurs when

the specimen is tilted so that only one diffracted beam is ‘strong’, i.e. will show great intensity in the diffraction pattern compared to other diffracted beams. Alongside the already strong direct beam this is known as the two-beam condition and both BF and DF images may be formed in this manner. This form of contrast is especially useful for imaging defects in a crystal lattice. This is because the specimen can be tilted such that it very nearly adheres to the two-beam condition and is only slightly tilted away from the Bragg angle, thus any distortion of the crystal lattice (defect) which would cause any scattering of electrons, will then be scattered to the Bragg angle and will produce strong contrast[92].

The principle of forming bright and dark field images in the STEM is the same as for forming BF and DF images using mass-thickness contrast. This usually means having a BF detector to collect the direct beam and an annular dark field detector (ADF) to pick up the diffracted beam. The two-beam condition is maintained by using the objective aperture to select only one strongly diffracted beam. The diffraction contrast produced in STEM is typically much weaker than in TEM images. This is because the ratio of the beam convergence angle to the detector’s collection angle is much larger in STEM, as the beam is converged rather than parallel. Therefore, to recreate the conditions of a TEM and achieve the same strength contrast, the detector’s collection angle must be limited, which decreases the amount of signal that can be collected by the detector[79].

2.4 High-Resolution Imaging (HRTEM and HRSTEM)

2.4.1 Phase-Contrast Imaging (HRTEM)

Phase contrast imaging is the name given to the TEM image mode that allows for images of samples with atomic resolution; the resolution achievable with this imaging mode is of the order of 0.5Å, and this small scale allows for the imaging of atomic planes and defects in a crystal[93]. This contrast mechanism arises due to the difference in phase between electron beams scattered through a thin specimen and is very sensitive to changes in the thickness, orientation or scattering

of the specimen. The most notable features observable using phase contrast are the lattice fringes. These fringes arise from the interaction of a scattered electron beam and the direct electron beam such that the resulting wavefront can be expressed as a linear combination of the incident and diffracted waves.

$$\varphi = \Phi_0(z)\, e^{[2\pi i(k_I \cdot r)]} + \Phi_g(z)\, e^{[2\pi i(k_D \cdot r)]} \tag{2.16}$$

Where Φ_i is the electron beam (either direct or diffracted). The interaction between these two waves results in a pattern of constructive and destructive interference with a sinusoidally varying intensity[75,79]. In high-resolution images this effect displays as 'lattice fringes'. The periodicity of the lattice fringes is dependent on the constituent diffracted electron beam and as such, the lattice fringes allow for direct measurements of the crystal structure[94].

The limiting resolution for images generated in this manner is determined by the contrast transfer function (CTF). The CTF describes how information is transferred as a function of spatial frequency and can be used to determine the contrast generated by the microscope. This is necessary because after the incident electron beam interacts with the specimen, the phase and amplitude of the beam is altered; detectors are only able to directly measure amplitude and so phase information is often lost. However, the phase interference can be measured through the electrons' interactions with crystalline solids and, in a thin sample, the CTF can be expressed as shown in Eq. 2.17[95].

$$\mathrm{CTF} = -\sin\left(\frac{\pi}{2} C_s \lambda^3 k^4 + \pi k^2 \Delta f\right) \tag{2.17}$$

Where C_s is the spherical aberration coefficient, which measures the quality of the objective lens, λ is the wavelength of the incident electron beam, k is the spatial frequency and Δf is the defocus value (the aberration caused by the specimen being out of focus and corresponds directly to the focal value used for the image). An example of the contrast transfer function is shown in Fig. 2.8.

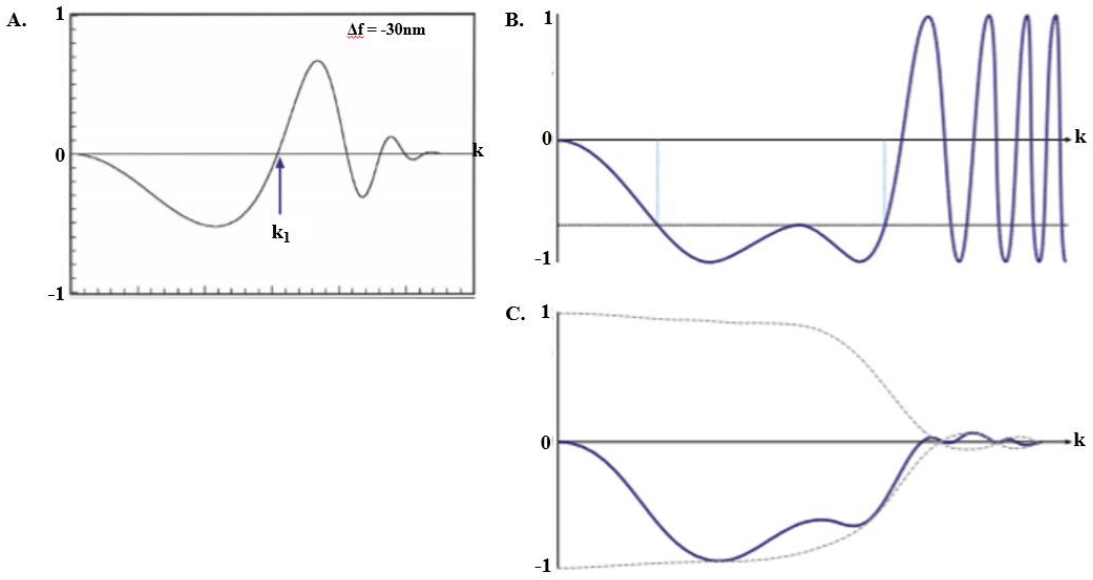

Figure 2.8 Examples of contrast transfer functions taken from *Transmission Electron Microscope, Williams and Carter* where A) CTF for a 200keV microscope with C_S of 1mm and Δf of -30nm where k_1 represents the point-resolution of the image, B) a CTF at extended Scherzer defocus without damping functions and C) a CTF at extended Scherzer defocus with damping functions[75].

The important features of the function are the oscillatory nature and the sign; where the CTF crosses the x-axis there is no information transferred at this spatial frequency and as such no contrast will be seen, when the CTF is positive, negative phase contrast will occur so that atoms will appear bright against a dark background, lastly when the CTF is negative the atoms will be dark with a bright background. The point at which the CTF crosses the x-axis for the first time represents the point-resolution limit of the microscope, beyond this point the features caused by the phase contrast can no longer be directly interpreted. This limit can be exceeded with the use of image simulation software provided the microscopes information limit is greater than the point-resolution limit. The information limit provides the maximum limit of the CTF as the expression in Eq. 2.16 allows for a continuous CTF however in practice envelope functions limit the maximum spatial frequency. These functions express the damping effects of chromatic aberrations and finite beam convergence

and can be expressed as E_c and EA respectively. The resulting effective contrast transfer function is expressed in Eq. 2.17 [96].

$$\mathrm{CTF}_{eff} = E_c E_A \cdot CTF \tag{2.18}$$

In practice, this means that a lot of focus in high-resolution imaging revolves around maximising the contrast transfer function by extending the region of spatial frequencies before the point-resolution is reached. Another method of optimising high-resolution images is by creating a contrast transfer function with high, uniform contrast in the region before the point-resolution. This is achieved by setting the defocus value to the Scherzer defocus which represents the optimal working conditions for phase contrast imaging. The value for the Scherzer defocus is dependent on the microscope in question and is a function of the accelerating voltage λ and the spherical aberration coefficient Cs as expressed in Eq. 2.18 [97].

$$\Delta \mathrm{f}_{Scherzer} = -1.2\sqrt{C_s \lambda} \tag{2.19}$$

An example of the contrast transfer function optimised for the extended Scherzer defocus is shown in Fig. 2.8.

2.4.2 Z-Contrast Imaging (HRSTEM)

Z-contrast is the name given to the high-resolution mechanism for mass-thickness used in the STEM. Images are formed by collecting low-angled elastically scattered electrons using the annular dark field (ADF) detector as single atom scatterings are incoherent, the image intensity is the combination of the individual atomic scattering contributions. As mentioned previously, this process is sensitive to the changes in the thickness of the substrate and it is impractical to a get a perfectly uniform thickness in a specimen, making the contribution from localised variations in specimen thickness indistinguishable from changes due to the atomic mass of the scattering atom. This problem is addressed in STEM by subtracting the ADF signal from the inelastic signal that would normally be used for EELS (Electron Energy Loss Spectroscopy)[98].

2.5 Energy Dispersive X-Ray Spectroscopy (EDX)

The last technique used in this study is that of electron spectroscopy, as mentioned previously, the interaction between the incident electron beam and the specimen produces a number of secondary signals. EDX spectroscopy makes use of the x-rays emitted by a specimen that undergoes inelastic scattering events that cause an electron excitation and de-excitation event producing a characteristic x-ray. All elements from Be (atomic number 4) to Uranium (atomic number 92) can, in principle, be detected, but not all microscopes are suitable for detecting lighter elements ($Z < 10$)[99]. The x-rays emitted by these elements can be quantitatively analysed to determine the concentration of the elements present by measuring the line intensities for each element and comparing it to the line intensities measured for the background regions[79].

EDX detectors are typically constructed out of semiconductors such as silicon and will be positioned to allow emitted x-rays to be collected by the detector's window. Emitted x-rays deposit energy into the semiconductor and cause valence band electrons to excite into the conduction band, creating electron-hole pairs. As the material for the detector is known the energy required for this transfer is also known (Si ~ 3.8ev)[100]. Since characteristic x-rays have energies often much larger than 1keV, thousands of electron-hole pairs can be created by a single incident x-ray, this number being proportional to the energy of the x-ray. Due to this, it is possible to determine what the energy of the incident x-ray was by detecting the number of electron-holes produced which, in turn, allows of the identification of the atom that produced the x-ray.

The accuracy of the EDX detector is limited by both the statistical accuracy, as the process relies on the counting of incident x-ray photons and the number of electron-hole pairs that are created, and the energy resolution. The energy resolution is important as the natural line width of an emitted x-ray is only a few eV, however empirically measured line widths in an EDX signal can be much greater than 100eV[101]. Detectors lose resolution as their temperature increases or the count rate is increased, this is balanced by the fact that low count rates (resulting in small peaks) can be indistinguishable from the 'background' caused by the continuous x-

ray spectrum emitted. This continuous bremsstrahlung radiation is produced as beam electrons are slowed down or stopped due to the electrostatic interactions with atoms in the specimen. The resulting continuum of x-rays is zero at the beam energy and tends to infinity at zero energy. This signal overlaps with the signals produced by characteristic x-rays and provides a limit to the size of x-ray peaks that can be identified and is more pronounced at lower energies[79].

2.6 Sample Preparation

The creation of nanoparticles through physical vapour deposition has a number of advantages over traditional chemical methods, for example, the nature of any chemical reaction requires detailed knowledge of the chemistry of all the reactants while deposition in the gas phase can be achieved through the same method regardless of materials. Furthermore, deposition of particles in this way can produce exciting, novel structures that would be extremely difficult through chemical means. The ability to create core-shell structures with, in principle, any shell material is extremely valuable, as the coating of nanoparticles allows for different possibilities in their functionalisation such as; protection from oxidation, increased catalytic activity or the design of a more functional particle surface.

All the particles in this study were created through the deposition of nanoclusters in ultra-high vacuum (UHV) conditions in a sputter gas aggregation cluster source at the University of Leicester. A schematic diagram of the cluster is shown in Fig. 2.9 and consists of four main components: the cluster production chamber, inter aperture, core-shell evaporator and the sample deposition chamber. The clusters are produced through sputtering and gas aggregation in a bath of argon (Ar) gas, which is controlled and monitored by pressure gauges across the whole of the cluster source. A systematic breakdown of the creation of the samples will now be examined from the production of the metal (iron) clusters to deposition onto the TEM grid.

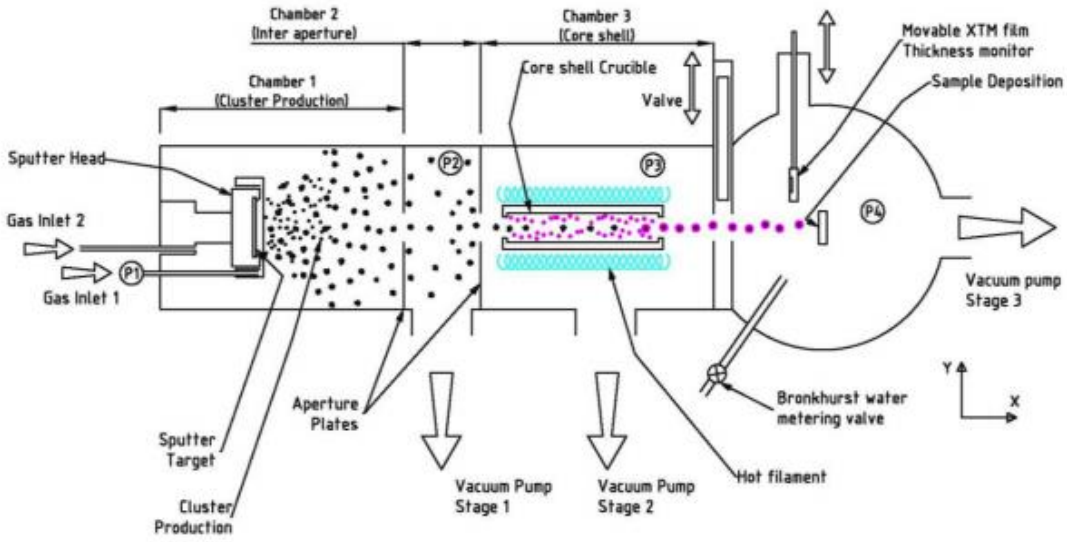

Figure 2.9 Schematic of UHV cluster source at the University of Leicester, diagram reproduced with permission[102]

To produce the nanoclusters, the target material is sputtered using an Ar bath gas. This is achieved due to the transfer of kinetic energy from the Ar atoms that have been ionised through free electrons to a negatively biased Fe (or other material) target, the application of a voltage between the target (cathode) and the magnetron cover (anode) causes the positively charged argon gas to collide with the fixed target. This provides a super-saturated region around the target, which causes the iron vapour to nucleate through subsequent collisions with argon atoms/ions. This is required as, after the sputtering event liberates Fe material from the target the resulting free Fe atoms have high momenta and cannot form clusters; further collisions with the argon reduce this momentum. The iron clusters are then steered through the system by a pressure gradient that is manipulated by regulating the amount of argon gas in the system. The rate of collision with the Fe target is further enhanced by the presence of magnets behind the target to aid the likelihood of nearby argon ions being driven in the direction of the target.

The coating of nanoparticles is done as the newly formed iron clusters are passed through a tubular crucible, this allows for the creation of a second metal vapour that will collide and adhere to the passing nanoclusters. The thickness of the deposition can be controlled through the manipulation of the temperature in the

evaporator, although the technique works best when the vapour pressure of the original material is lower than the vapour pressure of the desired coating material, as this prevents any vaporisation of the original nanoclusters. The core-shell evaporator can also be used without any shell material, in this case it will function as a furnace for the iron clusters. This is advantageous, as it allows for the studying of heating effects without the presence of oxidation as, assuming no leakage of outside oxygen from the air into the system, the particles will have yet to form their initial oxide, which usually occurs instantly after the sample is exposed to air. While it is possible to protect the nanoparticles from oxidation after synthesis through chemical methods, this will involve suspending the nanoparticles in a solution. This complicates the chemistry of the system and, subjecting the iron nanoclusters to heating during the deposition process allows for a direct study of the effects of heating on the structure of the clusters. The shell evaporator is 100mm in length with an alumina crucible which is surrounded by a heating filament, the whole region is heat shielded so that particles are heated only as they pass through the region.

The morphology of a deposited sample depends on a number of factors including: the substrate, particle material, temperature and impact energy, which will all affect the result. In general, the type of deposition expected can be divided into three categories based on the impact energy the nanoclusters have when they reach the substrate[103]. Low-energy deposition typically occurs when the energy is <1eV per atom, in the case of a thin film deposition, this will produce a weak adherence that can easily be removed. In the case of low-energy nanoparticle deposition, the impacting clusters will suffer little distortion on impact and as such will not damage the surface. If the rate of deposition is high this will produce an array of randomly stacked particles that will be hard to interpret when imaging, as such it is often necessary to limit the deposition rate, so that only one particle will occupy one local region of the substrate, to make image interpretation easier. In most cases, the impacting atoms in the cluster will not have the energy to diffuse across the substrate, as is the case in this study. However, with some substrates the diffusion of atoms post-deposition can still occur.

Medium-energy deposition occurs at impact energies roughly 1-10eV per atom, with the particles often remaining intact upon deposition. though significant changes in their morphologies may occur, including the introduction of defects into

the particle surface. Diffusion across the substrate surface must be considered at medium-energies as, depending on the materials being deposited and the material of the substrate, the atoms may be highly mobile. High-energy deposition is considered as any impact energy greater than 10eV per atom and in this case the impacting particles are often completely disrupted, with non-negligible damage to the substrate surface, this type of deposition can rarely be used to produce individual nanoparticles and will instead result in the deposition of a metallic thin film. The samples created in this study are deposited at low deposition energies, with the energy being controlled by the manipulation of the gas pressure gradient in the cluster source.

2.7 Experimental Design

2.7.1 Experiment One: Annealed Iron Core-Shell Nanoparticles

The experiment was designed to investigate the structural changes that iron core-shell (Fe/Fe_xO_y) nanoparticles undergo when oxidising. Due to iron particles requiring periods of up to two years to fully oxidise in air, however, oxidation was induced through heating in atmosphere[65]. Understanding the effects of oxidation on particles such as these is important to optimise the material properties for use in medical applications as discussed in chapter 1.

The temperature for heating was chosen to be 200°C and was picked as it offered the best mix between enhancing the oxidation process to more practical time-scales while preventing damage to the carbon-support grid, which has been found to occur at temperatures above 300°C[104]. At these temperatures, the carbon-support film becomes mechanically unstable and can break or lead to hydrocarbon contamination build-up on the grid that can severely impair image quality[105]. The temperature is not chosen to represent that used during medical processes (<45°C) but instead used purely as a means of increasing the rate of oxidation.

The heating duration was chosen to be 15 minutes based on a short preliminary experiment where samples were heated at the target temperature (200°C) for 15, 30, 60 and 120 minutes. It was found that after 15 minutes heating there were no significant changes in either the particle size or morphology with all the values for the size lying within error of the mean of all samples and with an average particle geometry ratio of 0.97 (corresponding to highly spherical). The results have been displayed in (Table 2.1).

The particles were deposited onto copper TEM grids using a holey-carbon support film with an estimated thickness of 20nm from Agar Scientific[106]. The nanoparticles were heated in an alumina tube furnace with a maximum temperature of 1500K and the ability to set the heating time. For analysis the samples were imaged and characterised in TEM and STEM due to their ability to image and resolve the samples down to atomic resolution and to carry out chemical analysis using EDX (section 2.4).

Table 4.1 Average particle size and geometry for different heating times at 200°C. Average particle size and geometry determined through the collection of 200 data points per sample with particle geometry expressed as the ratio of the particle maximum and minimum calliper distances with cubic particles at a minimum of 0.63 and spherical particles at a maximum of 1.00.

Property	15 minutes	30 minutes	60 minutes	120 minutes
Particle Size	43.8±3.4 nm	44.1±3.2 nm	39.6±3.8	47.0±3.9
Particle Geometry	0.97±0.02	0.99±0.01	0.98±0.02	0.97±0.02

2.7.2 Experiment Two: Coated Iron Nanoparticles

The particles were deposited at the University of Leicester using a cluster deposition source as outlined above. The empty crucible in the shell evaporator was loaded with ≈1g of Cu across a potential heating range from room temperature up to 1200°C. Samples of Fe@Cu were created at the temperatures of 218°C, 317°C, 442°C, 705°C, 777°C, 895°C, 994°C, 1052°C and 1131°C. The average error in the temperature reading was given as ±45°C. These temperatures were chosen as they covered the range of temperatures possible using the shell evaporator. Furthermore, the vapour pressure of Cu within the crucible was estimated using the temperature to range from ≈10-11 mbar to ≈10-3 mbar. The temperature was adjusted to allow for the comparison of the sample characteristic between the different temperatures; of particular interest are the size and shape of the particles as well as the shell thickness. The shape plays an especially important role as there is evidence linking the magnetic properties of iron nanoparticles with the geometry, with cubic particles offering highly favourable magnetic properties compared to spherical particles.

The cluster source operating parameters for these samples were: a sputter magnetron between 10W and 20W with an Argon gas bath sputtered into the system at pressures of 30 mbar for P1 and 2×10-4 mbar for P3. The terms are described in detail during the section on the cluster deposition source in section 2.6. This section aims to investigate the sample characteristics of the various samples using TEM and STEM imaging. To this end, all samples were created through low-energy deposition of the prepared Fe@Cu onto lacey or holey carbon TEM support grids. Due to copper being one of the working materials Ni TEM grids were used for this section. The presence of copper material will be inferred using Energy Dispersive X-Ray Spectroscopy (EDX) mapping, a feature available to the STEM.

Chapter 3: Heated Iron Nanoparticles

In this chapter, the thermally-induced oxidation processes of core-shell Fe/Fe_xO_y nanoparticles are examined by (S)TEM as discussed in chapter 2. An explanation of the motivation and scientific context was given in chapter 1, with a short discussion of the experimental design presented in chapter 2. In this chapter, the characterisation of the samples before and after annealing is given and the changes in the nanostructure are presented, lastly, there will be a discussion on the mechanisms governing those changes.

It was found, that after annealing at temperatures of 200°C in atmospheric conditions for a duration of 15 minutes, the sample displays a doubling of the oxide shell thickness with the average shell being 7nm thick. The oxidation of these particles was accompanied by the formation of Kirkendall voids at the metal/oxide interface that developed during the heating process. Furthermore, it was found, that the samples underwent significant morphological changes after heating, with the average size increasing and the shape of the particles in the sample dominated by spherical nanostructures as opposed to cubic structures. The rapid growth of the oxide shell cannot be attributed to the traditional Cabrera-Mott theory, which is used to characterise the initial formation of the oxide layer, as discussed in chapter 1.

We hypothesise that transport of material along grain-boundaries explains the oxidation observed, because, at such temperatures diffusion through the bulk lattice is energetically unfavourable. To determine the validity of this the diffusion coefficient of the material through the grain boundaries was empirically estimated from High-Resolution Scanning Transmission Electron microscopy (HRSTEM) images.

The particles were deposited at the University of Leicester (Department of Physics and Astronomy) and the analysis of the particles was performed using a JEOL 2011 Transmission Electron Microscope (TEM) and JEOL 2200 FS (Scanning) Transmission Electron Microscope (STEM) at the JEOL York Nanocentre of the University of York.

3.1 Pre-Annealing Iron Core-Shell Nanoparticles

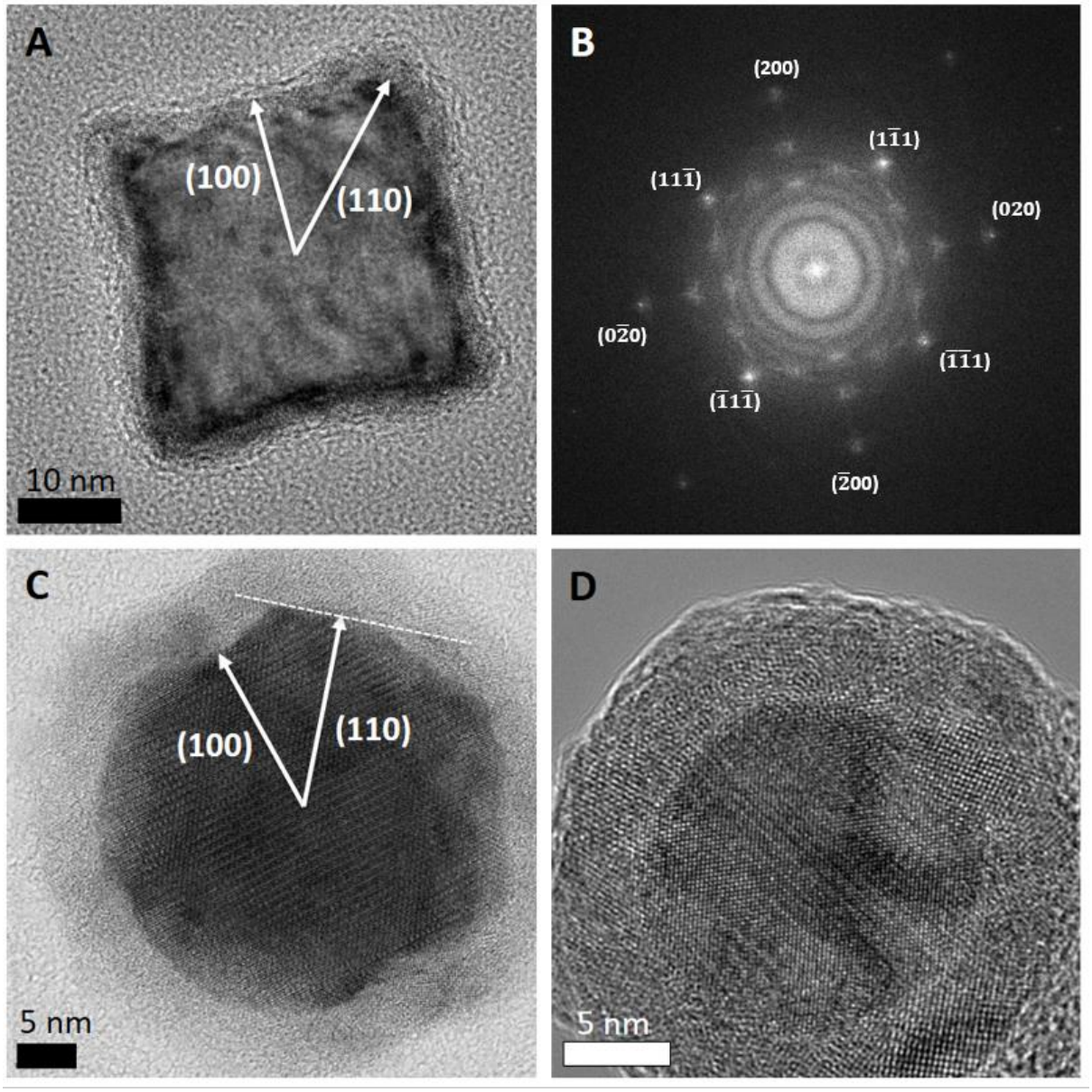

Figure 3.1 High-resolution images of unheated iron oxide nanoparticles taken using a JEOL 2200 (S)TEM, A) Bright-field TEM image of a cubic particle showing (100) and (110) directions, particle shows no truncation of the in the (110) directions and is common in samples prepared at colder temperatures. B) FFT of particle in A displaying typical structure of iron and iron oxide with iron reflections labelled, C) Bright-field TEM image of truncated cubic particle with (100) and (110) directions shown, the (110) surface facet is indicated by white dashed lines. D) Bright-field STEM image of spherical particle showing iron core and oxide grains.

3.1.1 Effect of Deposition Conditions

In the sample prior to heating, it was found that most particles possessed a 'truncated' cubic morphology. These cubes were confined by the six {100} planes and truncated by the twelve {110} planes with different degrees of truncation being observed, an example of the truncation is shown in Fig. 3.1C. However, many particles were found as cubic shapes, possessing only a small truncation along the {110} plane as shown in Fig 3.1A. At the other extreme there were particles found that possessed spherical geometries, representing the lowest surface energy configuration for the system (Fig. 3.1D). Where geometry is defined as;

$$G = \frac{X_{min}}{X_{max}} \tag{3.1}$$

Where X_{min} and $X_{max}$are the minimum and maximum calliper distances for the particle as shown schematically in Fig. 3.2. While a large number of particles were found to contain a heavily truncated geometry such as the particle in Fig. 3.1C where the truncation along the {110} plane was very large. No particles observed were confined only by the {110} planes with no {100} plane, these particles however, have been found in samples deposited at very high temperatures above 500K[107]. The deposition temperatures of the samples used here range from 81°C to 494°C making the formation of rhombohedral particles less likely.

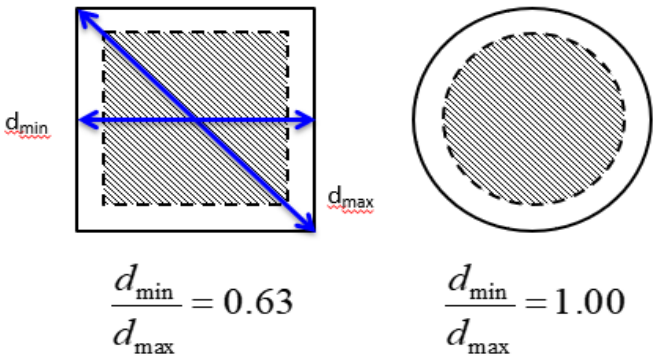

Figure 3.2 Schematic diagram of the particle geometry classifications. Particles in the sample are described by the ratio of the of the minimum and maximum feret diameters such that a perfect cubic particle (this would appear as a square in transmission) would have a ratio of 0.63. A perfectly spherical particle (which would appear as a circle in transmission) would have a value of unity.

The average particle geometry of the sample can be related to the deposition temperature of the sample, as increased temperatures results in greater amounts of thermal energy, which the clusters can utilise to re-organise into low surface energy configurations. Therefore, a larger number of spherical particles would be expected in a sample produced at higher temperatures, this can be seen in Fig. 3.3, which shows the increase in the average geometry as a function of particle deposition temperature.

Particles were deposited at temperatures between 81°C and 494°C, the former representing the lower limit for the temperature achievable using the cluster deposition method (see chapter 2). The highest temperature was chosen due to a combination of limits in the deposition method; only four samples can be deposited, and the temperature range of interest. Temperatures used in medical settings are much lower than the temperatures used here, however, the mechanisms behind oxidation are still debated at temperatures below 500K, where grain boundaries are assumed to play a significant role.

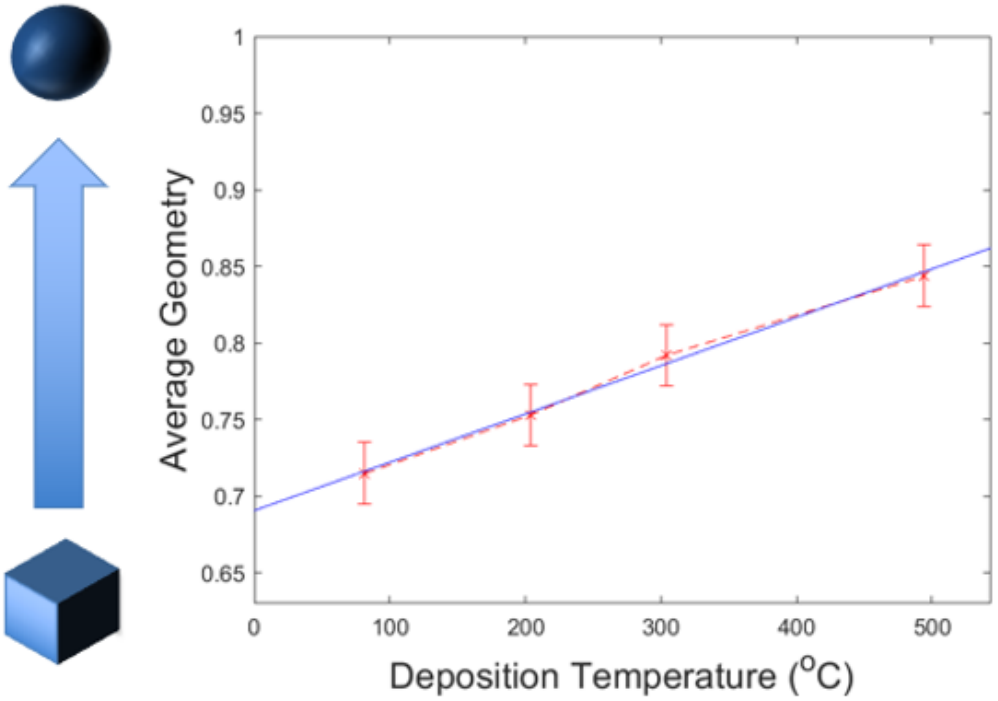

Figure 3.3 Graph showing measurements for the average particle geometry depending on the deposition temperature for the sample. The averages for each sample were calculated on the basis of 200 particles. The geometry was manually determined with the error bars representing the standard deviation.

The samples deposited at higher temperatures showed a greater proportion of large, truncated and spherical particles compared to those deposited at lower temperatures. This is shown by measuring the diameters and geometry of between 100 and 200 particles for each sample as shown in Fig. 3.3. The breakdowns of the size, geometry, and initial oxide thickness distributions are shown in Fig. 3.4 and Fig. 3.5, with the oxide thickness discussed later as its formation is, in theory, not effected by deposition temperature. The range of particles observed across all samples was between 10nm and 60nm, with the lower limit of the particle size increasing to 20nm at 304°C and 494°C. The size histograms show an average size of 19.7±0.6nm for the sample deposited at 81°C, 24.8±0.5nm for the sample deposited at 204°C, 31.7±0.6nm for the sample deposited at 304°C, and 36.4±0.6nm for the sample deposited at 494°C. Representing a 184% increase in the size of the average particle across the range of temperatures, assuming that zero or negligible oxidation occurs during deposition due to the ultra-high vacuum conditions this increase cannot be attributed to growth of the oxide shell and is a result of the deposition conditions.

It has long been established that the best way to model the distribution of particle sizes is using the *lognormal* distribution, this originates from early studies regarding aerosols and has since been found to be a common trend in nanoparticle distributions as well[108]. A quantity is described as lognormal when its natural logarithm is normally distributed. The origin of lognormality is thought to be due to the nature of any change in particle size away from the mean is due to random processes; modelled as a random walk on an exponential scale. As a random process can be modelled by a normal distribution, a random process on an exponential scale can be modelled by a lognormal distribution[109]. Mathematically the lognormal distribution can be fitted through the equation;

$$f(x \mid \mu, \sigma) = \frac{1}{x\sigma\sqrt{2\pi}}\, exp\left(\frac{-(ln(x) - \mu}{2\sigma^2}\right) \tag{3.2}$$

Where μ is the sample mean and σ is the standard deviation. The goodness-of-fit for a lognormal distribution is often taken to be the goodness-of-fit of the data's natural logarithm to a normal distribution, this can be measured through a chi-squared test[110]. The chi squared test is appropriate when the sampling is random,

and the variable is categorical, the threshold for the number of counts is roughly 100 which is the number of counts per sample in this study[111]. The test is conducted by comparing χ^2 which is calculated as shown in Eq. 3.3 against the desired significance level, the significance level used for the distributions in this study was 0.05 (95% goodness-of-fit).

$$\chi^2 = \sum \frac{(O - E)^2}{E} \tag{3.3}$$

Where O represents the observed frequency (number of counts) and E represents the frequency predicted by the normal distribution. All chi squared tests fell within the significance range stated previously and thus the distributions presented offer a good model for the distribution of particle sizes in the pure Fe nanoparticle samples.

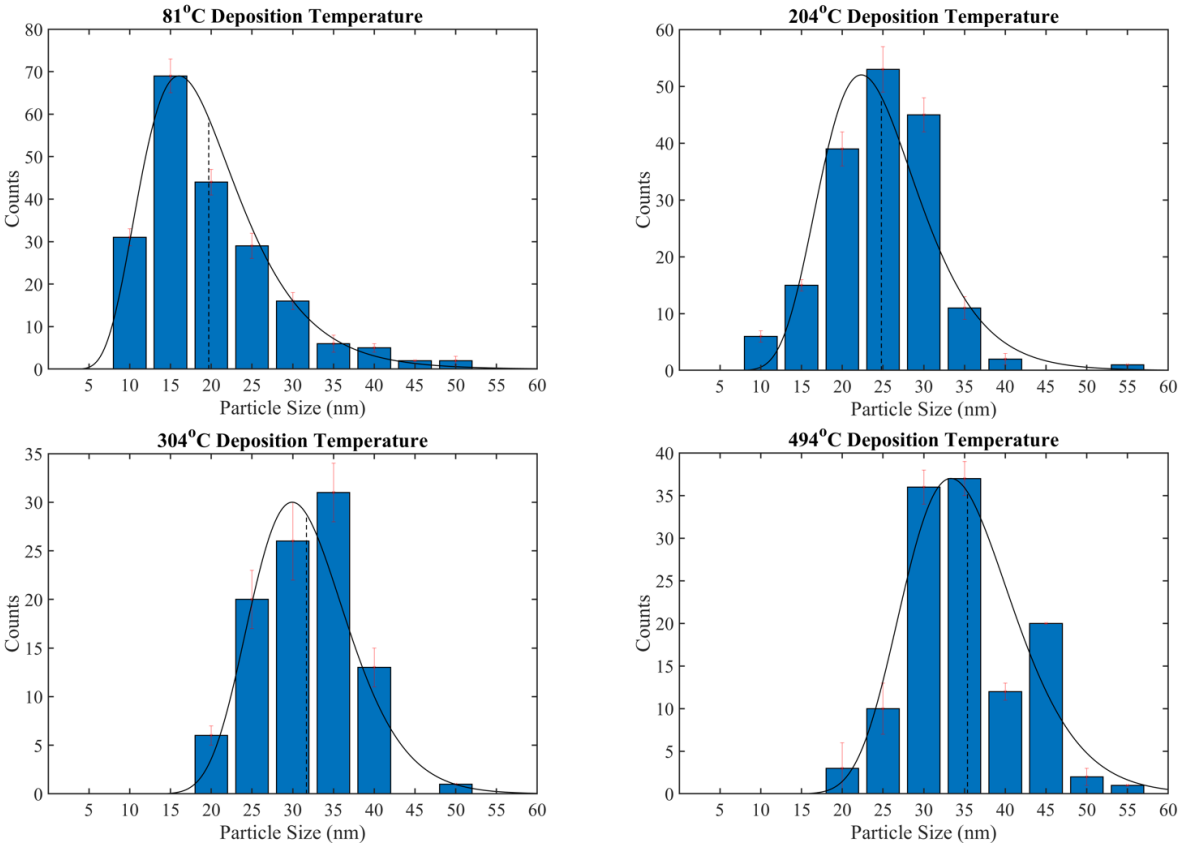

Figure 3.4 Size distribution histograms for samples created at four deposition temperature 81°C, 204°C, 304°C and 494°C. Average particles sizes were found to be 19.7±0.4nm, 24.8±0.5nm, 31.7±0.6nm and 36.4±0.6nm respectively with the average for each histogram denoted by a black dashed line. The number of particles measured was a) 200, b) 172, c) 101 and d) 121.

The error in measuring the size of an individual particle was determined by comparing the size determined using a threshold value calculated as described above with upper and lower limit thresholds which were determined by hand. The upper threshold limit was determined as the value at which the derived particle size would not increase anymore while the lower limit was determined by the point at which the oxide shell was no longer included in the binarised image. The errors calculated this way were of the order of 1nm. The error in the bin counts was determined by measuring the number of particles that fell within 1nm of the bin edges.

The classifications for the qualitative description of particle morphology were based on the ratio of the of the maximum and minimum calliper distances as shown in Fig. 3.2. The particles were considered cubic if their calliper ratio was between the minimum of 0.63 and 0.75, while a particle was classed as spherical if the ratio was between 0.85 and 1.00. Any transitional geometries with ratios between these two classifications were classed as 'truncated' particles. This term describes both 'truncated cubic' shapes, characterised by significant {110} truncations but where the length of the {110} planes was still lower than the {100} planes. As well as, 'truncated octahedral' shapes which contain even larger {110} truncations such that the length of the {110} is approaching or exceeding that of the {100} planes. The errors for the histograms in both Fig. 3.4 and 3.5 were calculated through counting the number of particles that were within 10% of the bin edges, with the error for the sample averages determined by the standard error in the mean.

As can be seen in Fig. 3.5, a particle is more likely to possess a spherical or truncated geometry at high deposition temperatures. The average particle geometry in the coldest deposited sample (81°C) was determined to be 0.7533±0.005, representing the ratio of the minimum and maximum Feret diameters. For the sample deposited at 204°C the average was found to be 0.775±0.006, with 0.792±0.008 for the sample deposited at 304°C, and lastly, 0.844±0.008 for the hottest deposition temperature of 494°C. This represents a 12% increase in the Feret ratio and shows an evolution to spherical particle geometries.

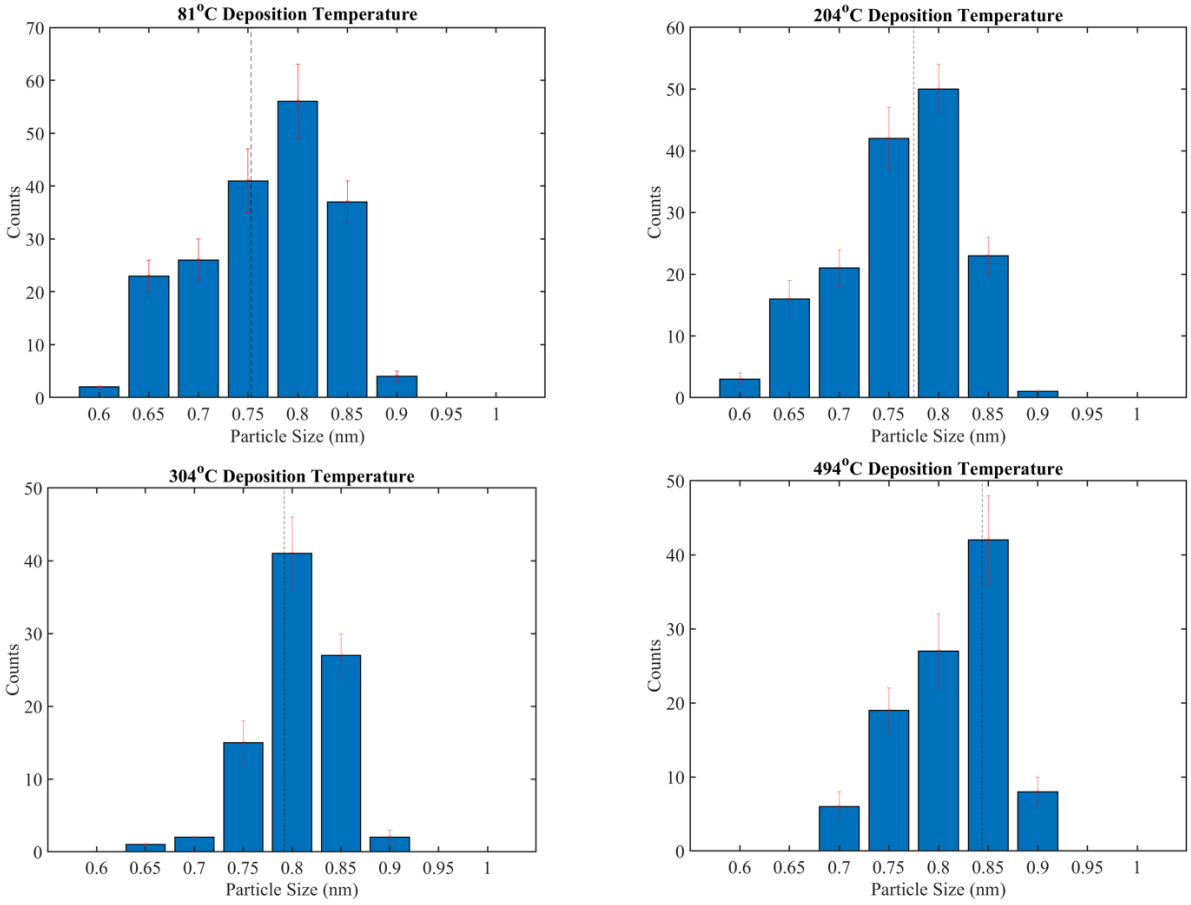

Figure 3.5 Geometry distribution histograms for samples created at four deposition temperature 81°C, 204°C, 304°C and 494°C. Average particles sizes were found to be 0.753±0.005, 0.775±0.006, 0.792±0.008 and 0.844±0.008 respectively with the average for each histogram denoted by a black dashed line. The number of particles measured was a) 200, b) 172, c) 101 and d) 121.

A comparison of the respective increases in particle size and geometry due to deposition conditions can be seen in Fig. 3.6. The increase in size due to deposition temperature must arise from a separate process than the increase in size due to oxidation because, as stated previously, oxidation should not have occurred at this stage (during deposition). It is believed that the increase in size can be attributed to increase in the collision frequency between iron nanoclusters and molecule iron in the deposition chamber, combined with re-evaporation of material from the chamber walls, as discussed later.

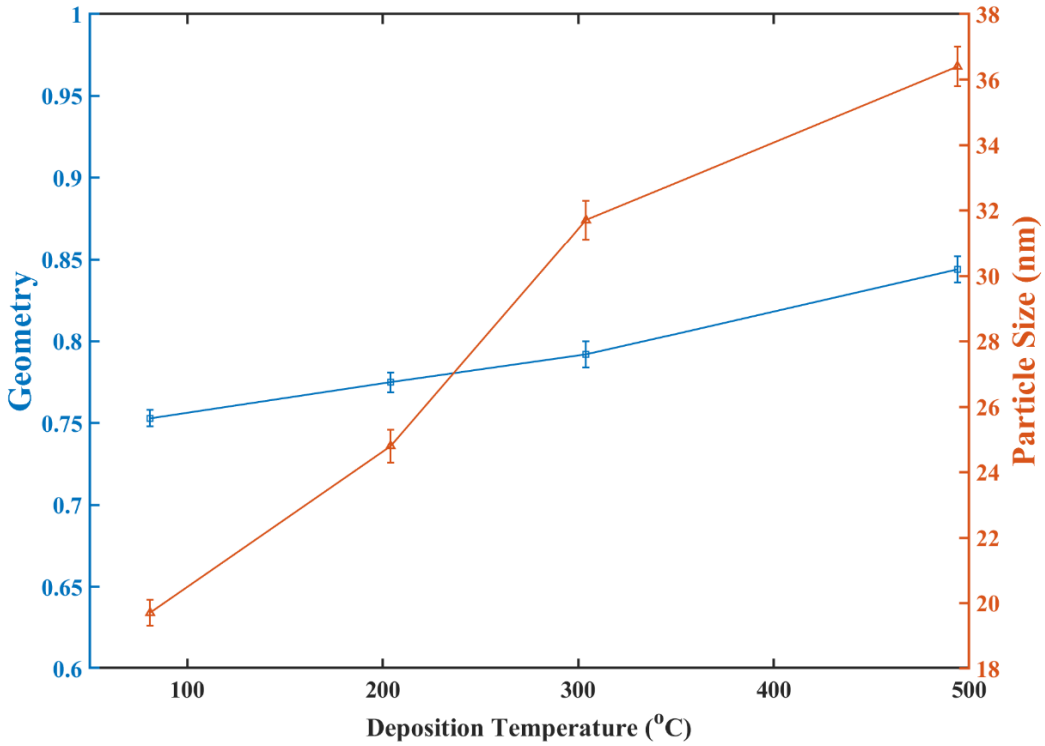

Figure 3.6 Summary of the change in particle size and geometry as a function of the deposition temperature, clearly seen is the significant increase in particle size across the temperature range with average size increasing by 186%. Particle geometry ratio increases by 12% with the average particle increasing in the degree of truncation along the <110> facets.

The construction of a particle's 3D structure can be done through the Wulff construction where, in an unrestricted environment the growth rate along various directions will determine the overall shape of the crystal. Similar to the surface energy in a Wulff construction and the various ratios along the <100> and <110> directions can be used to construct the observed geometries as shown in Fig. 3.7. It has been found that the main factor determining the dominant morphology is the deposition temperature, with samples deposited at room temperature more likely to have a cubic structured particles, with few heavily truncated particles and no rhombohedral particles[112]. Conversely it has been shown that particles deposited at high temperatures contained no cubic morphologies[113]. This fits well with what has been observed here with the cooler samples which contain particles with smaller degrees of truncation than those in the hotter samples.

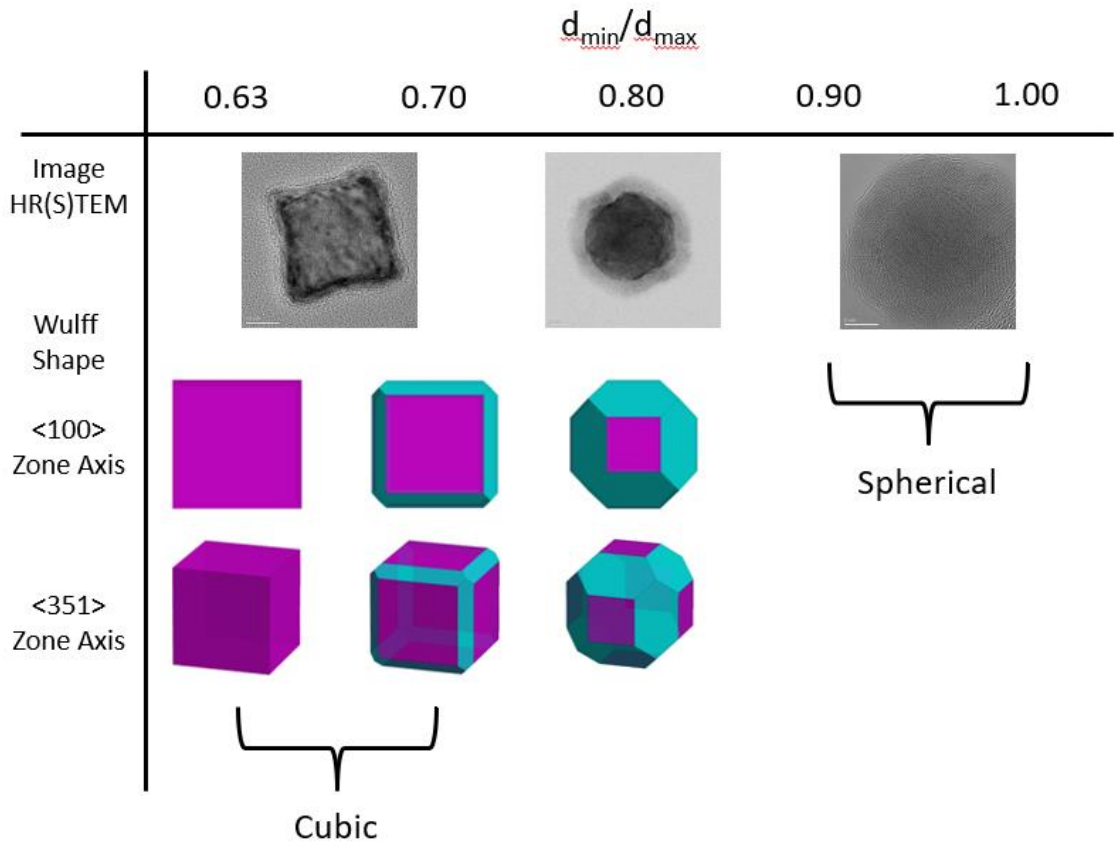

Figure 3.7 Schematic diagram showing the variation in particle morphologies by their calliper ratio with accompanying Wulff construction (constructed through publicly available Mathematica code[114]) where the surface energy ratio is equal to the calliper ratio.

The qualitative classifications described above can separate the different geometries, with cubic (geometry ratio <0.75), spherical (ratio >0.85), and truncated particles investigated separately to determine the effect of increased temperature on each type of particle. The relationship between the particle geometry and the particle size has been explored in more detail in Fig. 3.8. The majority of particles occupy the top-left side of the diagram representing smaller, spherical or truncated particles, however, there is a general tendency for larger particles to be more spherical in shape with few large particles exhibiting cubic geometries. This suggests that as the sample's average particle size increases, due to either the deposition temperature or the natural variance of particle size in the sample, the possible range of geometries for these particles narrows.

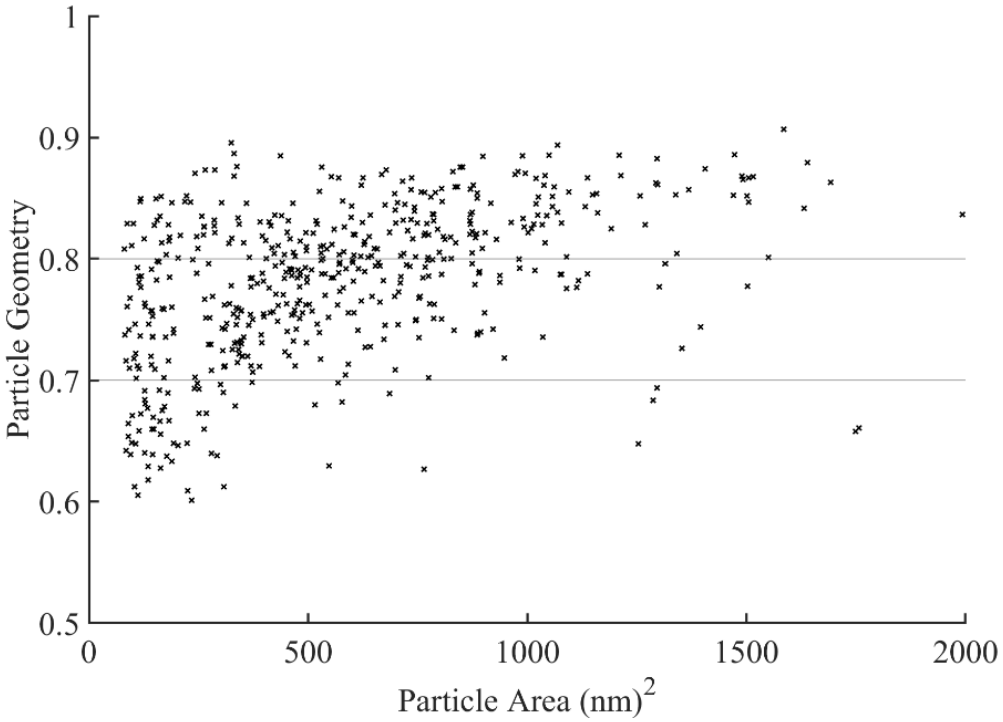

Figure 3.8 Particle geometry as measured by the ratio of the minimum to maximum calliper distance for 546 iron nanoparticles deposited at temperatures from 81°C to 494°C against their particle area measured in transmission.

As such the evolution of the particle geometry with deposition temperature appears to be driven by the increase in the proportion of spherical particles as opposed to truncated particles. This is inferred because of the established increase in the average particle size with deposition temperature and the fact that larger particles predominantly occupy the spherical region in Fig. 3.8. This is confirmed in Fig. 3.9 where the percentage breakdown of the particle geometries is given as a function of particle size. As can be seen in the figures the percentage of both cubic and truncated geometries decreases while the percentage of spherical particles increases from 17% of the smallest particles to 94% of the largest particles.

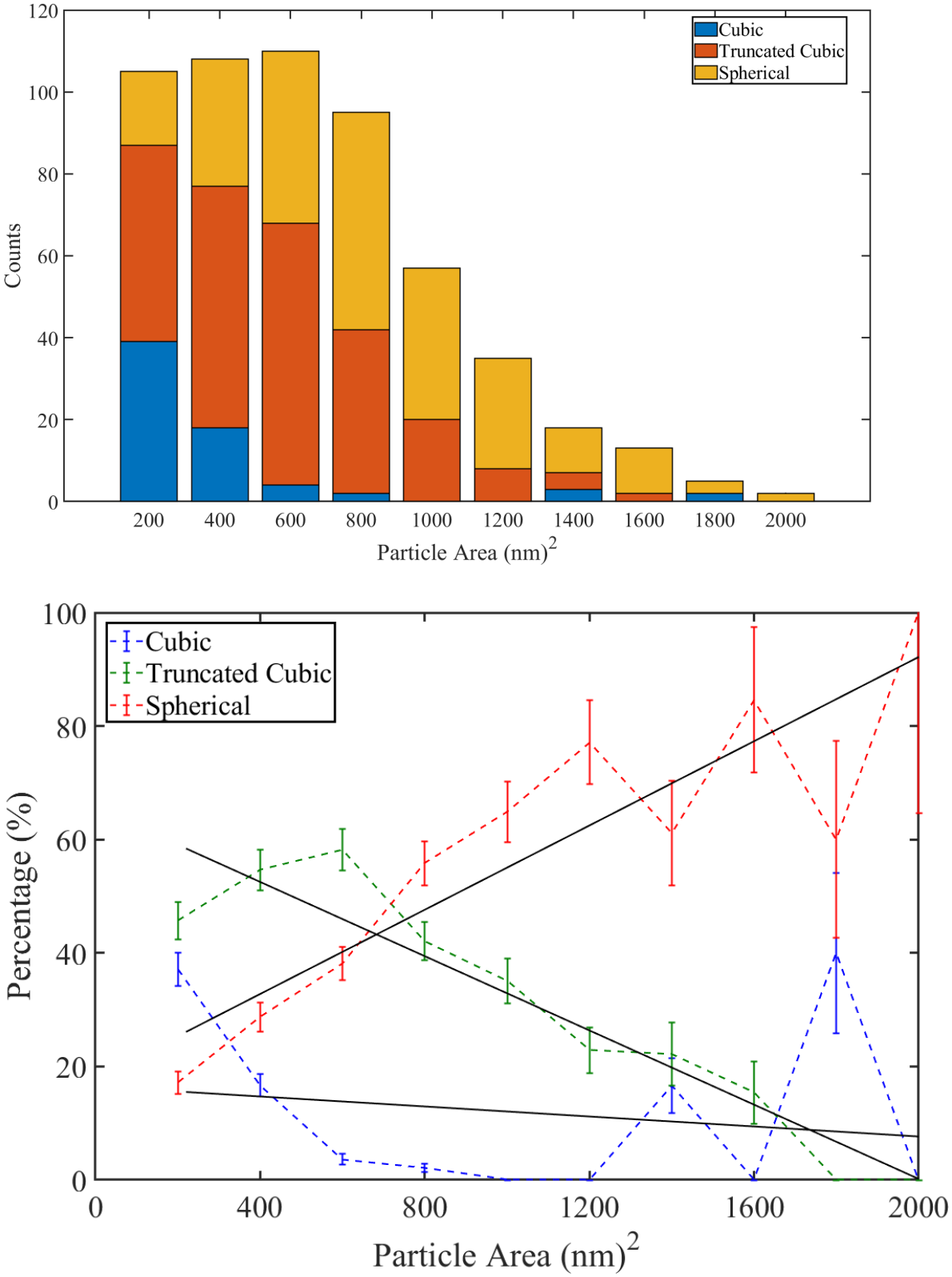

Figure 3.9 (Top) Histogram showing the number of cubic (blue), truncated (orange) and spherical (yellow) particles that appear at increasing particle size. (Bottom) Percentage of particles that display cubic (blue), truncated (green) or spherical (red) geometries as a function of particle size. Linear regressions are fitted to highlight the decrease in cubic and truncated particles and increase in spherical particles.

3.1.2 Initial Oxidation

Assuming that no oxidation occurs prior to the deposition of iron clusters onto the TEM substrate, the initial oxide will be formed after the samples have been removed from the chamber. As such any variations in the oxide thickness between samples should not be related to the deposition temperature but to the physical properties of the particles being oxidised. The oxide shell thickness distributions for all four deposition temperatures can be seen in Fig. 3.10 with an average oxide thickness of 3.11±0.19nm, 3.40±0.11nm, 4.24±0.21nm and 3.66±0.12nm for the 81°C, 204°C, 304°C and 494°C samples respectively. Except in a small number of case the oxide shell thickness lies within a range of 2nm to 6nm with no particle observed with an oxide shell of 6nm or greater. This initial oxide is well explained through Cabrera-Mott theory and has been observed on a number of occasions[29,49,115].

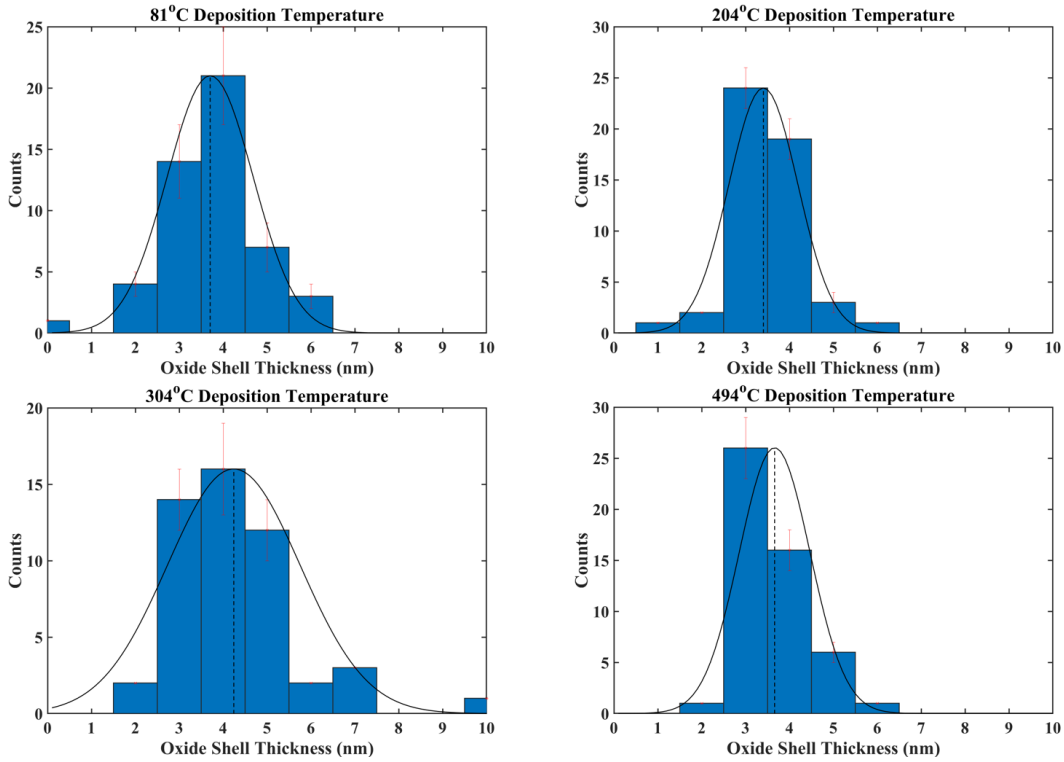

Figure 3.10 Shell thickness distribution histograms for samples created at four deposition temperature 81°C, 204°C, 304°C and 494°C. Average oxide shell thickness were found to be 3.11±0.19nm, 3.40±0.11nm, 4.24±0.21nm and 3.66±0.12nm respectively with the average for each histogram denoted by a black dashed line. The number of particles measured for each sample was 50.

The histograms in Fig. 3.10 have been fitted with a normal distribution that was confirmed using a chi squared goodness-of-fit test to be within the 95% confidence bounds for fitting. There was no significant divergence in the extent of the oxide thickness which would be expected if the oxide formed post-deposition.

3.2 Post-Annealing Iron Core-Shell Nanoparticles

3.2.1 Particle Size and Geometry Post-Annealing

The result of the annealing can be seen in Fig. 3.11 which displays in Fig. 3.11A an image from the coldest deposited sample (81°C). The coldest sample was chosen because it offered the largest variety of particle morphologies with cubic, spherical, and truncated particles being represented in the sample. Assuming that the oxide shell formed after the deposition process it allows for comparison of the oxidation behaviour for different particle geometries. Fig. 3.11A shows examples of cubic, truncated, and spherical particles while Fig. 3.11B and 3.11C show a high-resolution image of a particle, an interesting feature being the formation of interface voids and oxide ridges connecting the core to the shell. The sample was annealed at 200°C for 15 minutes and in the resulting sample it can be seen in there have been significant changes in the particle's size, shape, and oxide shell thickness. The resulting characterisation of the sample is displayed in Fig. 3.12 which shows the size, geometry, and shell thickness distributions measured from the sample post-annealing. A comparison with the sample prior to annealing is provided with the average particle size having increased to 43.8nm from 19.7nm, the average geometry ratio increasing to 0.9753 from 0.7533, and the average oxide shell thickness increasing to 7.4nm from 3.1nm. The represents an increase of 122% in the particle size, a 138% increase in the shell thickness, and an evolution to spherical geometries which has been observed in other oxidation experiments[116].

The increase in the oxide shell thickness depends on the 'type' of particle in question with some particles having dramatically increased oxide shell thickness

(such as in the case for the fully oxidised particles observed in the sample) and some particles retaining a smaller, but still increased by comparison to the sample pre-annealing, oxide shell. This is represented in the change in oxide thickness range from 2-5nm before annealing to 3-14nm afterwards. Overall the changes to the sample after heating can be summarised in the following manner, with three general conclusions being drawn.

1) An increase in the average particle size pre-annealing from 19.7nm to 43.8nm post-annealing, the particle sizes range from 10nm to 50nm before and 20nm to 100nm afterwards.
2) A shift towards more spherical geometries can be seen in Fig. 3.12; almost no cubic particles exist in the sample post-annealing, with only spherical particles or highly truncated particles being observed. However, this shift only applies surface geometry with the geometries of the iron cores still retaining some degree of their cubic structure.
3) A large increase in the oxide shell from the average of 3.1nm (within the 2-5nm range predicted by Cabrera-Mott theory in chapter 1) to 7.4nm determined empirically post-annealing. Before annealing the range of sizes for the oxide shell was between 1nm and 5nm, after annealing, the range has increased from 3nm to 14nm depending on the extent of the particles oxidation.

A breakdown of the various particles will now be given before an analysis of the changes to the samples characteristics (e.g. size, geometry, and shell thickness), this will allow for a discussion on the various transport pathways that facilitate the enhanced oxidation that has been observed post-annealing (see chapter 5).

An interesting feature observed post-annealing is the development of Kirkendall voids at the metal-oxide interface[117]. The presence of small void structures is very interesting for medical-driven material physics as such particles are being considered as drug delivery agents [19]. Typically, studies involving 'hollow' particles focus on the type of particle that is completely hollow as opposed to the partially oxidised particles observed in these samples, these particles however, may be able to provide useful magnetic properties due to retaining their iron core.

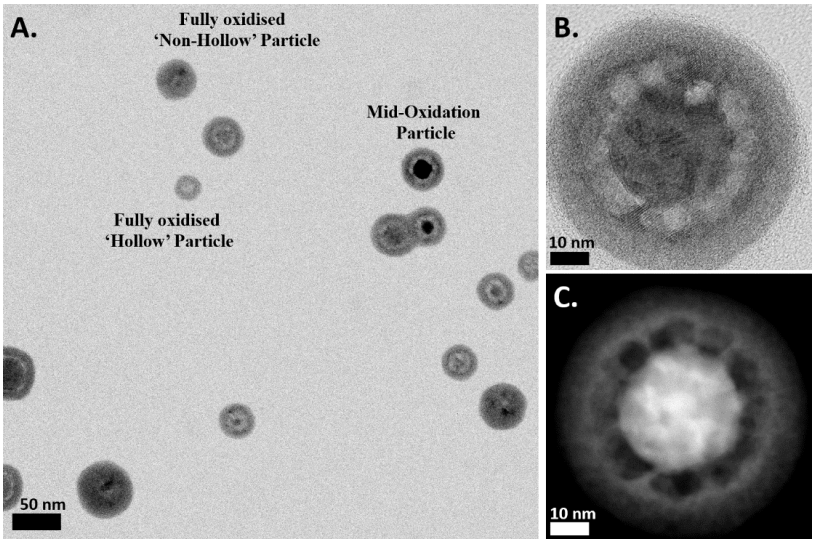

Figure 3.11 A) Post-annealing bright field TEM image of the sample showing the variety of particle types, B) HRSTEM image of a particle having formed interface void and oxide 'ridges', C) Dark field STEM image of B.

The particles post-annealing can be classified into three rough types of particles as shown in Fig. 3.11A. The first type are smaller particles that appear to retain no iron core and have fully oxidised in a manner that has resulted in a completely iron oxide nanoparticle. These particles are characterised by highly spherical geometries and particle sizes spread across the whole range of particle sizes as shown in Fig. 3.13. The average particle size for particles that have transitioned into iron oxide nanoparticles is 45.99±2.24nm with an average geometry of 0.952±0.004 corresponding to highly spherical shapes as viewed in transmission.

A notable feature of these particle is the presence of small central Kirkendall voids, the voids measured and compared with the area of the particles as measured in transmission images and were found to account for on average 19.3±0.9% of the particle volume assuming a spherical geometry. The distribution of the Kirkendall width percentages is shown in Fig. 3.14, the extent to which the Kirkendall voids compose the width of the particles is similar to those that have been allowed to oxidise gradually in air over extended periods[65]. This is much lower than reported in previously literature, with Kirkendall voids composing up to 60% of the deposited particles total width[32].

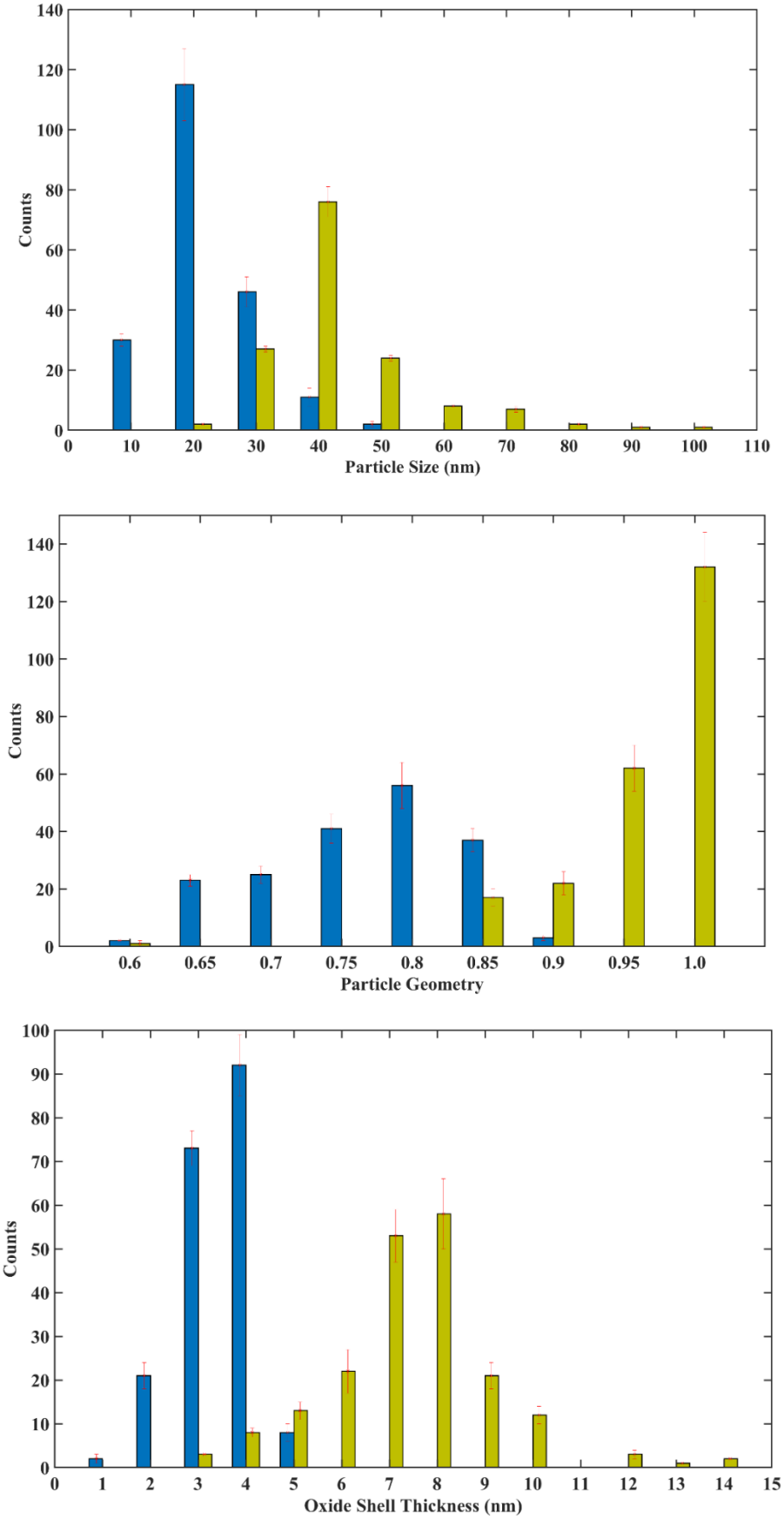

Figure 3.12 Size, shape, and shell thickness distributions of the samples before and after heating. With the errors calculated through the error in the mean.

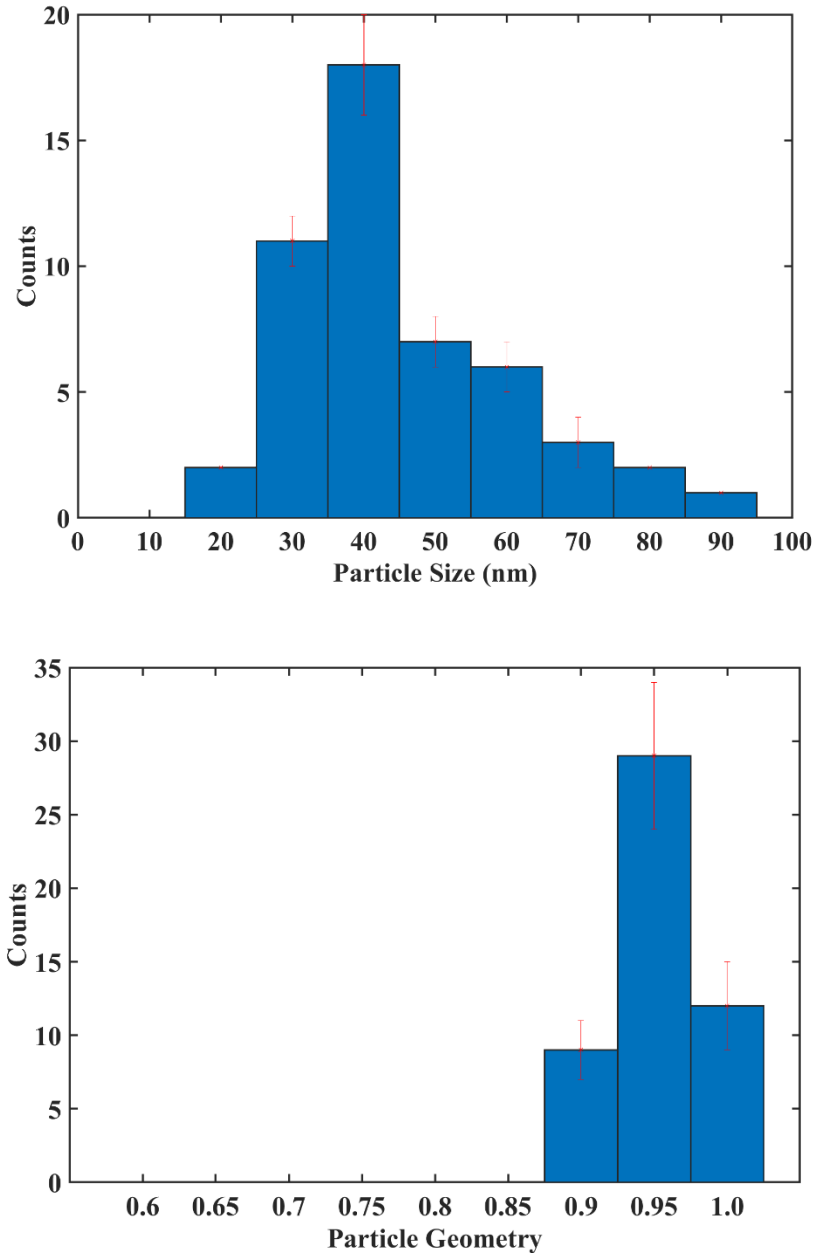

Figure 3.13 Particle size and geometry distributions for fully oxidised 'non-hollow' iron oxide nanoparticles with an average particle size of 45.99±2.24 nm and average geometry ratio of 0.952±0.004.

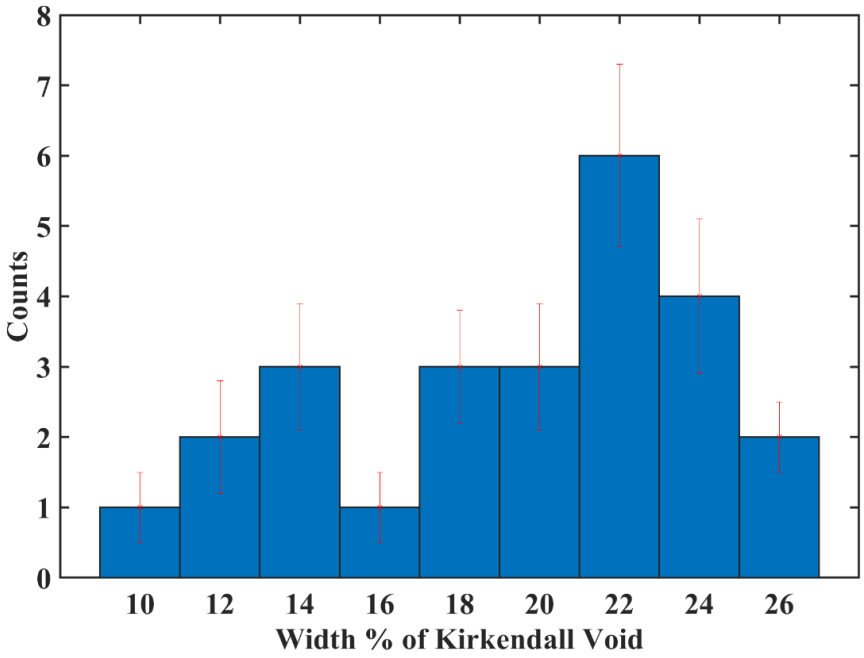

Figure 3.14 Calculation of the width percentage taken up by Kirkendall void in fully oxidised 'non-hollow' nanoparticles as shown in Fig 4.9.

3.2.2 Enhanced Oxidation

The progression from iron/iron oxide particle to full iron oxide particle has been observed to occur in cubic particles, as such it is likely that particles that have been oxidised in this manner originally started as cubic particles. This suggests that the oxidation front for these particles occurs at both the oxide/gas interface (accounting for the general increase in average particle size) and the metal/oxide interface allowing for the total oxidation of the iron core. This is surprising as in most cases the iron ions are the only diffusing species considered mobile at low temperatures while the oxygen anions are considered immobile. Therefore, the O ion diffusivity must be enhanced for these particles as the formation of Kirkendall voids relies on the faster out-diffusion of iron ions.

The second type of particle observed in the sample are particles characterised by being slightly larger than the previously mentioned particles and with the absence of an iron core. The average particle size and geometry for this type of particle can

be seen in Fig. 3.15 with values of 32.21±0.71 and 0.945±0.005 respectively, as such, these particles tend to be smaller than the average particle in the sample with no examples being found with sizes over 45nm. The oxide shell in these particles enclose a very large Kirkendall void, the distribution of the oxide shell thicknesses has been determined and displayed in Fig 3.16, with an average oxide shell thickness of 6.67±0.25nm with a range between 2-11nm. This represents a roughly 10% decrease in the average oxide thickness compared to the sample average after annealing. As with the 'non-hollow' iron oxide particles previously shown the width percentage of the Kirkendall void was measured for 50 particles and the distribution is shown in Fig.3.16.

The average width of the Kirkendall void that has developed in these particles was found to be roughly 60%, this is much closer to the value for particles in previous reports for iron nanoparticles oxidising in air[118]. This implies that the unlike in the previously seen particles, the diffusivity of the oxygen in-diffusion was not significantly enhanced; this is despite originating from the same sample as the aforementioned 'non-hollow' particles. As was determined in the case of cubic particles oxidising in atmospheric conditions, the enhanced oxidation was attributed to strain fields in the oxide shell. No such fields have been observed in spherical particles, as such, it is likely that particles of this type originate from spherical particles pre-annealing, this would explain why the oxygen in-diffusion has only been enhanced in certain particles (resulting in the difference in Kirkendall void size).

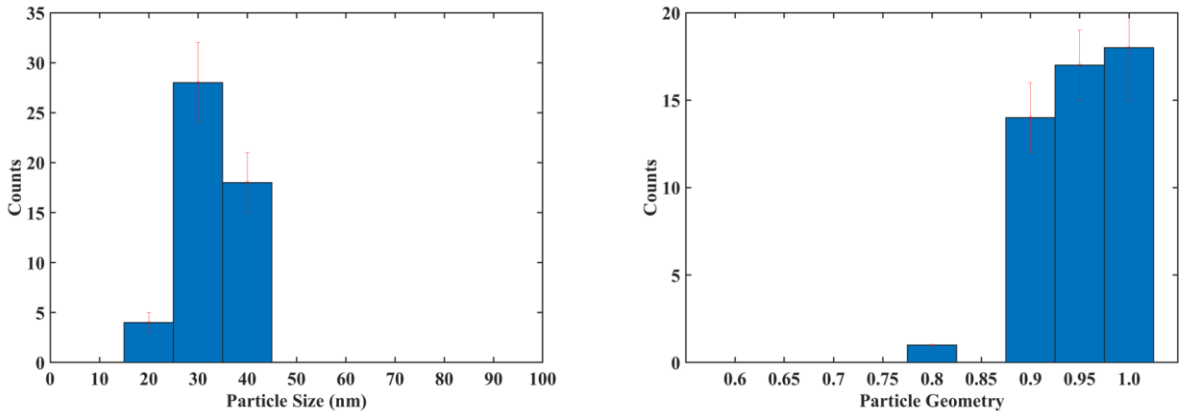

Figure 3.15 Particle size and geometry distributions for 'hollow' iron oxide nanoparticles with an average particle size of 32.21±0.71 nm and average geometry ratio of 0.945±0.005.

The heating of iron nanoparticles resulted in the formation of 'hollow' Kirkendall voids due relativity diffusivities, as oxygen in-diffusion is typically considered to be immobile when compared to iron out-diffusion, as such material leaves the core faster than enters it. The resulting Kirkendall void can be clearly seen in the dark field image in Fig. 3.16C which shows the iron oxide shell along with three small islands in the core. In the particles presented here it appears that the main pathway for the thickening of the oxide shell is the outward expansion of the oxidation front at the oxide/gas interface. This is in opposition to the previous particles where the enhanced O ion diffusivity that produces smaller Kirkendall voids suggests a more mobile oxidation front at the metal/oxide interface.

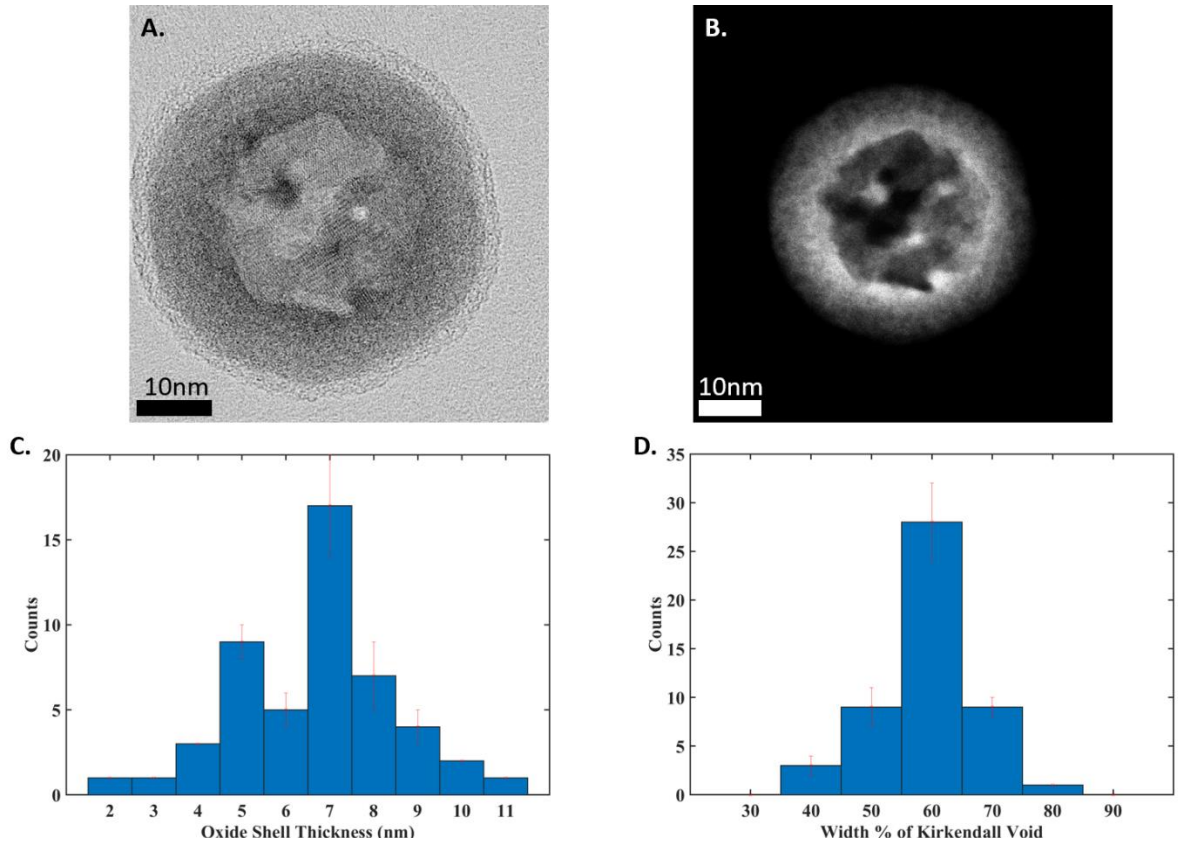

Figure 3.16 A) Bright-field STEM image of 'hollow' iron nanoparticle, B) dark-field STEM image of particle imaged in A. C) Shell thickness distribution for fully oxidised 'hollow' particles with an average oxide thickness of 6.67±0.25nm D) distribution of Kirkendall width percentages with an average of 58.9±1.1% calculated for 50 counts.

The last type of particle observed post-annealing are characterised by the growth of Kirkendall voids at the metal/oxide interface, the average size and geometry of these particles is shown in Fig. 3.17. The average particle size was determined to be 43.89±1.11 nm with an average geometry of 0.975±0.006, representing a greater average particle size than the 'hollow' particles and sample average, no example of a particle retaining its iron core was found below 26 nm. These particles are interesting as typically Kirkendall voids are expected to form at the centre of the particle due to the relative rates of anion and cation diffusion. In the particles observed here however, it appears that the increase in oxidation rate due to heating was enough to create vacancies at the interface.

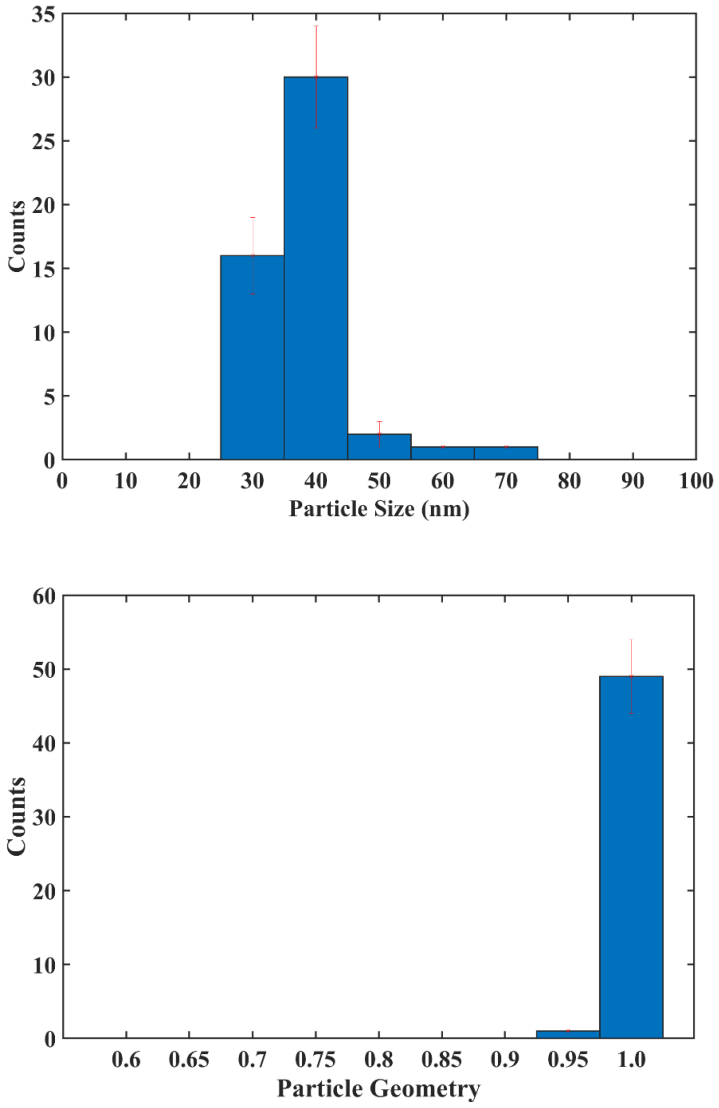

Figure 3.17 Particle size and geometry distributions for iron/iron oxide nanoparticles that have formed Kirkendall voids at the metal/oxide interface with an average particle size of 43.89±1.11 nm and average geometry ratio of 0.975±0.006.

Furthermore, the particle's iron core appears to be surrounded by a ring of these interface voids, which are in-turn terminated by 'oxide-ridges' connecting the remaining iron core to the oxide shell. It should be noted, that there appears to be a critical size with which these particles appear in the sample shown in Fig. 3.18, below this size particles are fully oxidised as either iron oxide particles or 'hollow' particles. Above this size 'hollow' and 'non-hollow' fully oxidised particles can still be observed alongside this type of particle as shown in Fig. 3.13. The degree to which the iron core is retained is dependent on the particle size with smaller particles being more sensitive to the effects of heating. In this manner, it may be possible in principle to tune the size of the iron core of these particles by controlling the annealing temperature and time. This could allow for the tuning of the particles magnetic properties as both the fully oxidised and 'hollow' particles do not retain their iron cores and by extension the desirable magnetic properties of iron. It is likely that had the heating temperature been higher or the duration longer then some of the particles that had been partially oxidised, forming metal/oxide voids, would have transitioned into the 'hollow' particles described previously. This is due to the coalescence of the smaller metal/oxide Kirkendall voids into larger islands and eventually into a hollow core.

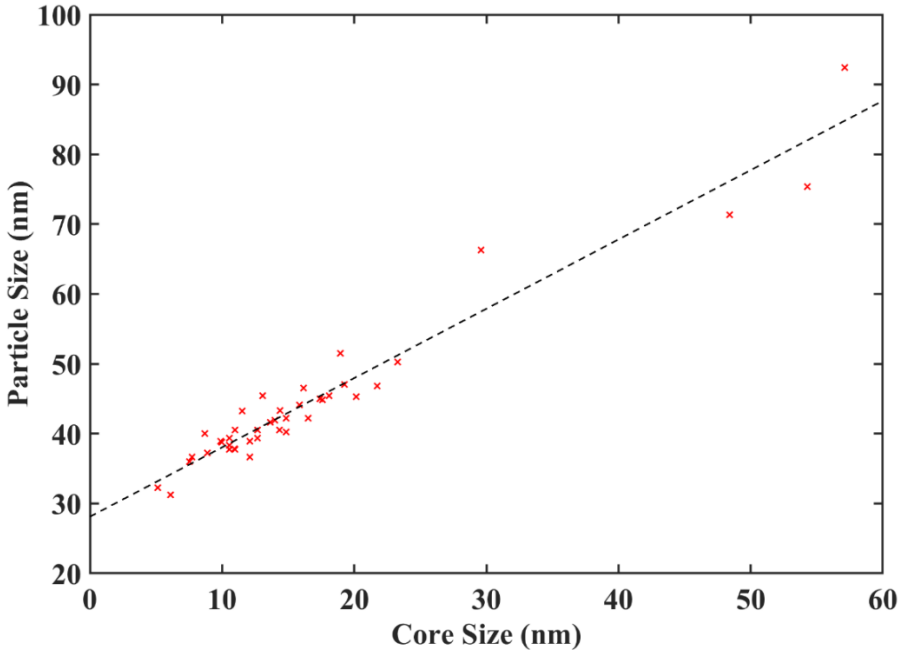

Figure 3.18 Graph of core size against particle size with line of best fit plotted in black with a gradient of m = 0.9927 and a y-intercept of 28.12 nm which represents the cut-off point for iron core retention with no particles retaining their cores being found below this size.

After heating, the sample underwent many significant changes and the resulting particles were classified into one of three types. Of the particles that fully oxidised the first type were iron oxide nanoparticles and were found to cover the complete range of particle sizes ranging from 15 nm in size to 90 nm. In some cases, these particles were found to have developed central Kirkendall voids occupying roughly 20% of the whole particle width similar to iron/iron oxide nanoparticles oxidised gradually in air. As such it is likely that this type of particle accounts for the oxidation of cubic nanostructures in the sample at a faster than rate due to the annealing. The other type of fully oxidised particles were those that had retained an oxide shell around a large depleted core, these particles had no iron core left and tended to be smaller particles ranging from 15 nm to 40 nm in size. The 'hollow' nature of these particles suggests they underwent rapid oxidation. With the relative diffusivity of out-diffusing iron ions being much greater than in-diffusing oxygen ions as this would account for large Kirkendall voids formed in these particles. Particles of this nature have been observed to occur in nanoparticle samples at temperatures around 250K from spherical particles that have been synthesised chemically. As such it is likely that this type of particle arises from the smaller spherical particles in the sample with the diffusion rates enhanced by the presence of grain boundaries in the particles.

The last type of particle observed were larger particles that had developed clearly defined Kirkendall voids at the metal/oxide interface, these particles range from 30 nm to 75 nm with the critical size of core retention observed to be roughly 28 nm. These particles are consistent with the model for the formation of 'hollow' nanoparticles due to the coalescence of interface voids. It is likely that these particles were originally spherical or highly truncated cubic particles as in some cases the particles core retains some of its original geometry. This can be seen in Fig 3.19. A comparison of the samples properties with regards to the average size, geometry, and the thickness of the oxide shells before and after annealing have been presented in table 3.1.

Table 3.1 Summary of the characterisation data for samples before and after annealing along with a comparison of the characterisation for the different types of iron oxide particles that result.

	Size	Geometry	Oxide Shell
Before Annealing	19.7 ± 0.4 nm	0.753 ± 0.005	3.1 ± 0.19 nm
After Annealing	43.8 ± 0.5 nm	0.975 ± 0.004	7.4 ± 0.22 nm
'Non-Hollow' Particles	45.99 ± 2.24 nm	0.952 ± 0.004	-
'Hollow' Particles	32.21 ± 0.71 nm	0.945 ± 0.005	6.67 ± 0.25nm
Mid-Oxidation Particles	43.89 ± 1.11 nm	0.975 ± 0.006	7.6 ± 0.18nm

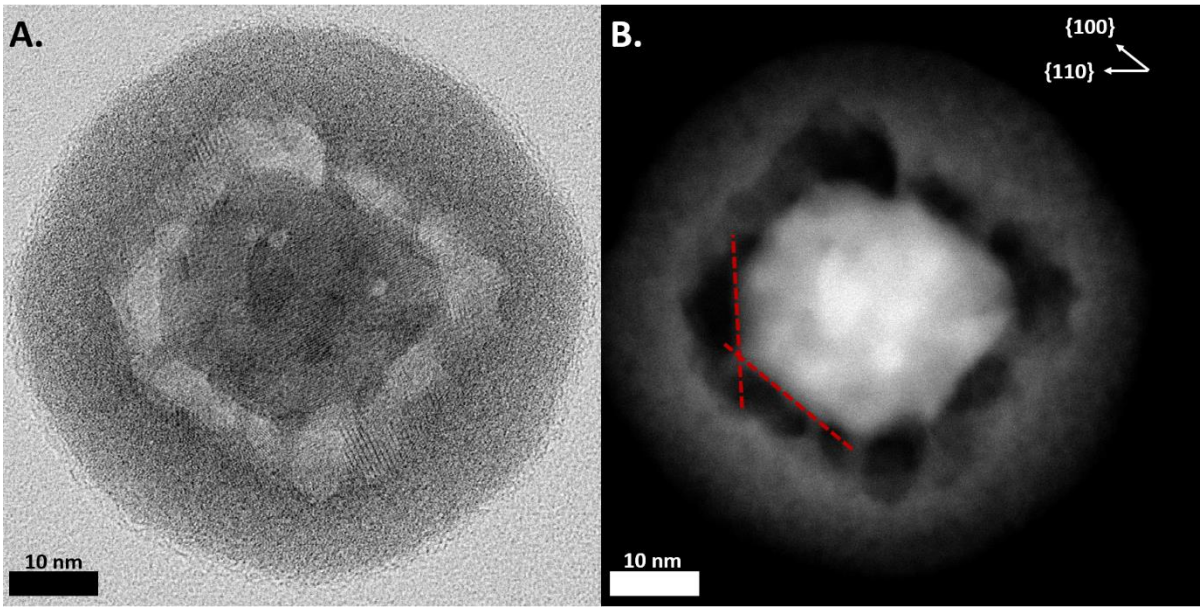

Figure 3.19 A) Bright-field STEM image of a particle at the transitional point between initial oxidation and full oxidation, formation of Kirkendall voids at the interface can be seen clearly as well as oxide 'ridges' connecting the shrinking iron core to the spherical oxide shell. B) Dark-field STEM image of the particle in A which shows clearly the retention of the original truncated core-geometry with the original {100} and {110} facets marked by the red dashed line.

3.3 Magnetometry

The magnetic properties of the iron samples were tested using a SQUID magnetometer by our collaborators at the University of Leicester with the total sample moment measured as a fraction of the applied magnetic field; at 5K and 300K with the field ranging between +/- 5T. The raw data was gathered at the University of Warwick and processed by our collaborators at the University of Leicester, the results of which are summarised here to highlight the viability of oxidised iron oxide nanoparticles in biomedical settings. The moment per gram of iron (Am2/g) was plotted against the magnetic field (T) and the resulting magnetisation curve from which the magnetic properties of the samples can be obtained are shown in Fig. 3.20.

The magnetisation curves for samples created at different deposition temperatures can be seen and the overall trend shows an increase in the observed magnetic moment with decreasing deposition temperature. Furthermore, the graphs in Fig. 3.20 show a degree of hysteresis in the M-H curves, as such the saturation magnetism was calculated by fitting a Langevin function of the form described in Eq. 3.4.

$$L(x) = \coth(x) - \frac{1}{x} \tag{3.4}$$

The Langevin function was used as the classical limit of the Brillouin function that describes the dependency of the magnetisation M on the applied magnetic field for a collection of non-interacting paramagnetic atoms or ions. The exchange interaction of the atoms locks the atomic moments so that the Fe nanoparticles act as a single magnetic moment, as such it will behave as a classical magnetic dipole. The temperature dependency of the saturation magnetism is shown in Fig. 3.21 as can be seen there is a sharp drop off around 300K which is above the annealing temperature used in this study. The nanoparticles measured here were not annealed post-deposition although the constituent iron nanoclusters were subjected to a similar temperature during deposition. It would be interesting in further studies to investigate how the magnetic saturation of the particles annealed post-deposition compares with those used in the magnetic measurements presented her.

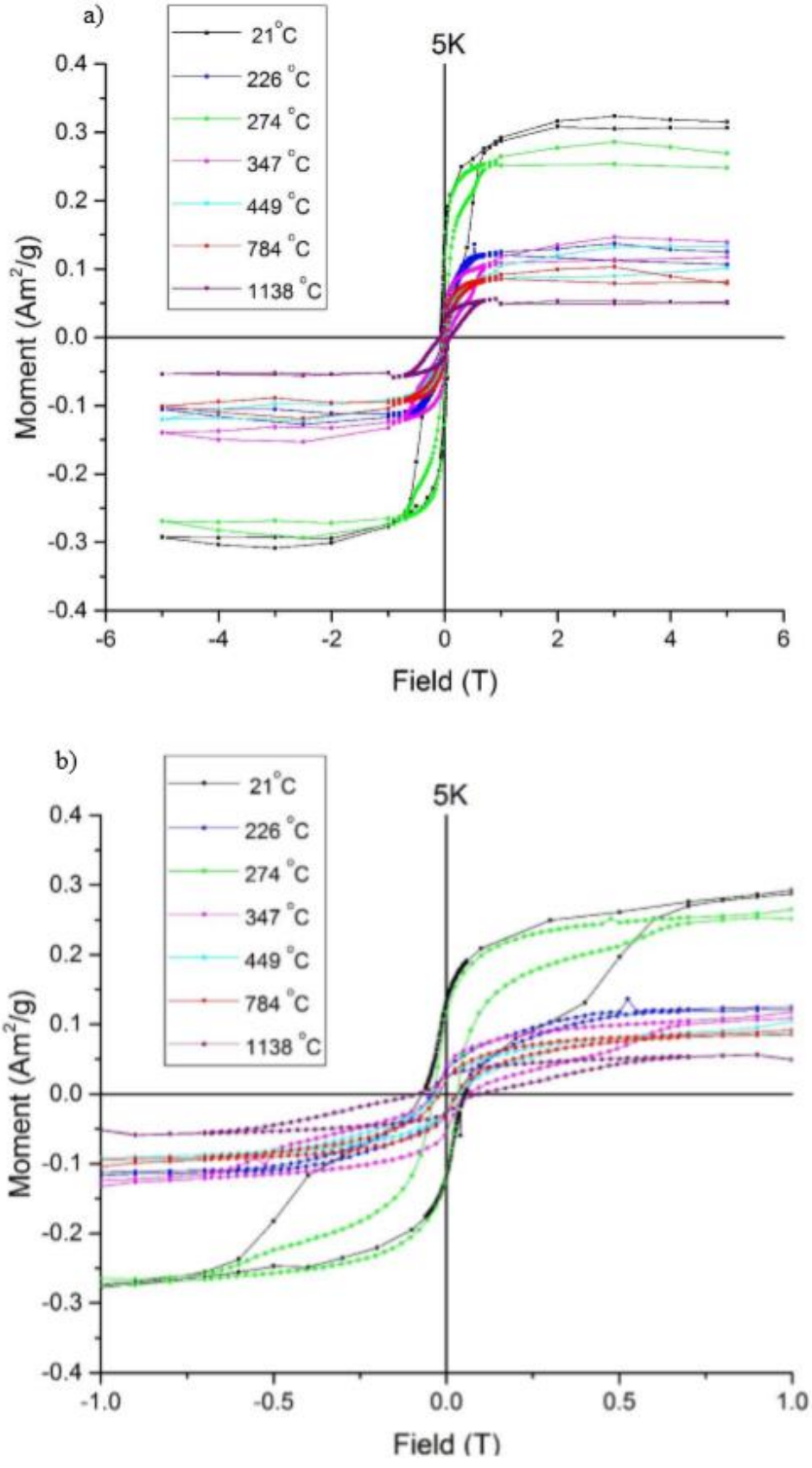

Figure 3.20 Raw magnetometry data obtained via SQUID and processed by collaborators at the University of Leicester (reproduced with permission)[102].

Compared to the average size of iron cores after annealing and the increase in the amount of iron oxide it would be expected that the magnetic saturation would be lower for particles post-annealing however understand to what extent this would be would be useful for the continued development of medically-functionalized nanoparticles.

The expected heating output of the un-annealed particles was also calculated by our collaborators at the University of Leicester as the area subtended by the hysteresis curves is directly linked to the heating output of the particles with the area under each hysteresis curve being presented in Fig. 3.21. A similar relationship to the measure saturation magnetism was observed with the expected heating output being greater for particles deposited at low temperatures. As such it the effect of the enhanced oxidation that can be observed occurring in the particles in chapter 4 that are heated post-deposition may have significant effects on the resulting magnetic response of iron nanoclusters that would undergo low levels of heating in some medical settings such as Hyperthermia or MRI or moderate heating when used as cell separation techniques that do not have the same limits for heating conditions as discussed in chapter 1. As such understanding how, the oxidation processes occur in different types of nanoparticles will be needed if efforts to created highly novel and tailored nanoparticles is to be realised.

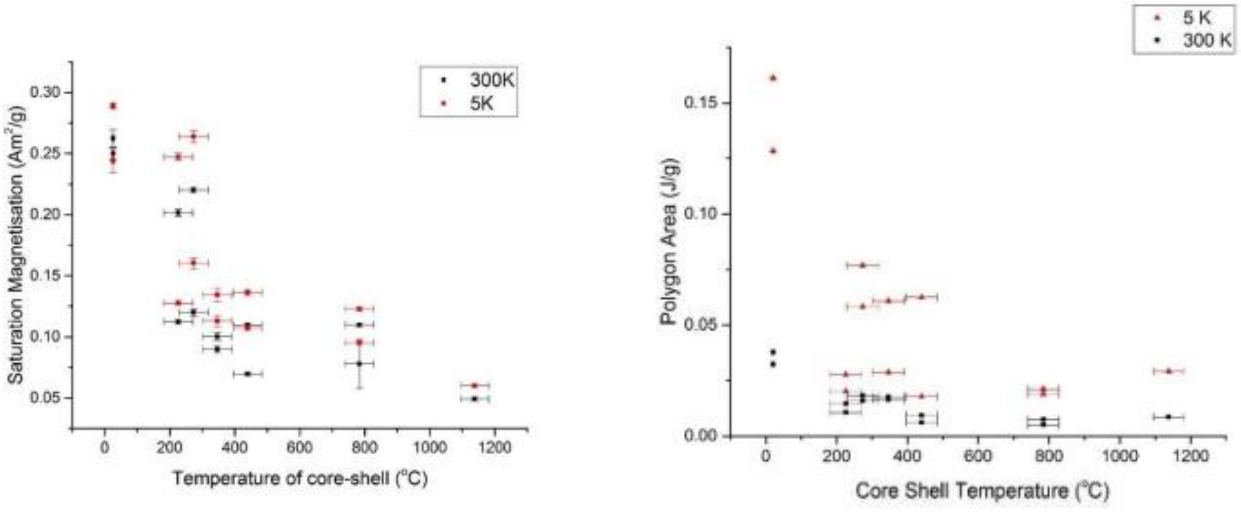

Figure 3.21 A) Saturation magnetism calculated through Langevin fitting of the raw hysteresis curves in Fig.5.14 as a function of deposition temperature, B) calculated area subtended by hysteresis curve showing a rough prediction of expected heating output of the particles in the sample as a function of deposition temperature. (Reproduced with permission)[102].

3.4 Discussion

The change in the particles physical characteristics (size, shape, and oxide thickness) as a function of deposition temperature (the temperature of the empty core-shell evaporator as described in chapter 2) is interesting to consider. It is possible to control the deposition conditions; for example, pressure, temperature, and time and as such understanding the effect the deposition conditions can have is a step towards developing better tailored nanoparticles for any application. The particles size and shape distributions have been presented in Fig. 3.4 and 3.5 respectively with the initial oxide formed post-deposition shown in Fig. 3.8. The change in physical characteristics with deposition temperature can be summarised as an increase in the average particle size from 19.7nm to 36.4nm and a change in the ratio between the particles maximum and minimum calliper distances from 0.75 to 0.84 representing an evolution from cubic particles to truncated particles.

The increase in the average particle size may be attributed to a number of processes centered either around the nanoclusters themselves or the deposition method. For instance, it is possible that the expansion of the iron lattice due to heating could result in an increase in the overall particle size when summed over the number of individual iron unit cells in the material. To investigate this possibility the increase in the iron unit cell lattice parameter at 494°C was determined to be 0.02Å for a lattice constant of 2.88Å, this increase was then applied to the average particle from the coldest sample at 81°C such that;

$$\frac{\Delta L}{L} = \alpha \cdot \Delta T \tag{3.5}$$

where α is the thermal expansion coefficient ($15.5 \times 10^{-6}\ C^{\circ -1}$ for iron)[119], ΔT is the change in temperature and L is the original lattice parameter. The result for an average particle of 13.5nm (average particle size of 19.7nm minus the average shell thickness) was found to provide a 0.2% increase in the particle size for a total of 19.8nm. As such it is unlikely that the thermal expansion of the particles has a major effect on the physical characteristics during deposition.

It is more likely that the increase in size arise from an increase in the collisional frequency of the particles in the molecular beam as they pass through the heated core-shell region. This can be due to two different sources; the first is an increase in the collisions between the iron nanoclusters and molecular iron as a result of the non-monoenergetic velocity distribution in the beam, the second is due to the re-evaporation of iron material from the chamber walls. In both cases a quantitative understanding of the kinetics is very difficult and is highly sensitive on the type of molecular beam and its properties, however, it is possible to offer a qualitative explanation for the increase in particle size.

One of the main advantages of molecular beams is that in principle no molecular collisions will occur along the beam path. This is however a very idealised model as it relies on the distribution of velocities in the beam to be mono-energetic, this would result in all molecules in the beam moving along the beam path at a uniform speed and not interacting[120]. In non-ideal cases however, molecules in the beam can possess a distribution of velocities for instance due to non-uniform particle sizes. The wider the velocity distribution the greater the chance of molecular collisions in the beam. The temperature dependence of the collisional frequency can be determined through the application of Kinetic theory where a mobile particle sweeps out a cylinder populated by a species of other static particles as shown in Fig. 3.22. In this regard the number of collisions per unit time is equal to;

$$Z_i = \frac{V \cdot \rho}{\Delta t} \tag{3.6}$$

where V is the volume of the cylinder which is equal to the atom's collisional cross section and is πd^2(the area of the circle) multiplied by the length which is the product of the relative speed and the change in time $\sqrt{2}\langle v_{rel}\rangle \Delta t$.

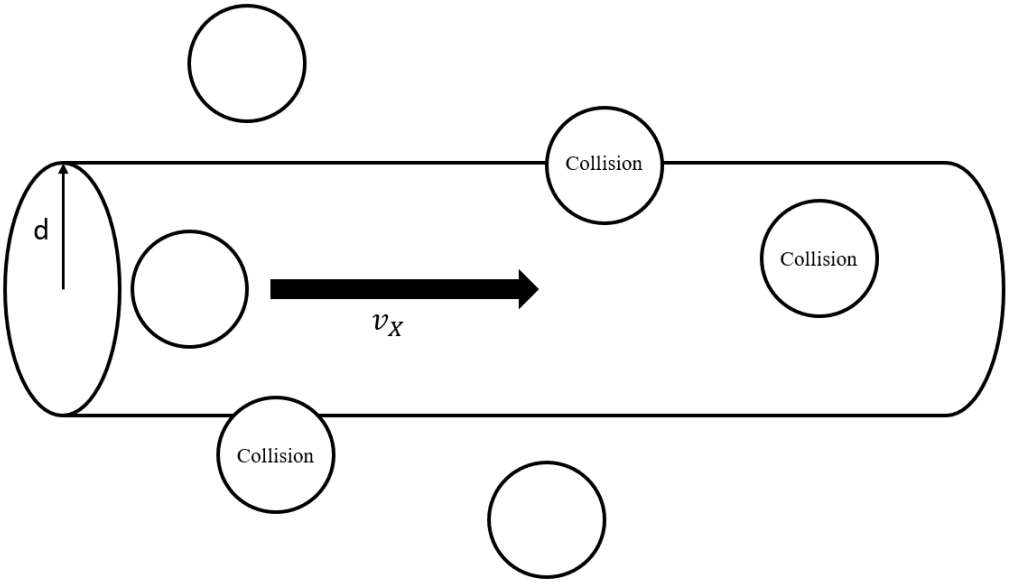

Figure 3.22 Schematic diagram of a target particle in a cylinder with static particles.

The density of the cylinder must account for all the atoms in the path of the particle that can be hit and assuming uniform density will equal the density of the gas given by the number density per unit volume. As such Eq. 3.6 may be re-written as;

$$Z_i = \frac{\sqrt{2}\pi d^2 \langle v_{rel} \rangle N}{V} \tag{3.7}$$

By allowing for two different species of particles and using the relative mean speed as taken from Kinetic theory the equation can be further modified to the more familiar version with a temperature dependence.

$$Z_i = N_A N_B (r_A + r_B)^2 \pi \sqrt{\frac{8 k_B T}{\pi \mu_{AB}}} \tag{3.8}$$

where N_i is the number of atoms of type i in the system, where r_i is the radius of the atom, k_B is the Boltzmann constant, T is the absolute temperature and μ_{AB} is the reduced mass.

Although the ideal gas assumptions used to derive the equation in 3.8 are not valid for molecular beams the temperature and mass dependences of the relative speed are important to note. Molecular beams are special in that a lower number of atomic collisions should occur however, it has been estimated that the ratio of the collisional frequency in a molecular beam and the frequency in a gas is such that up to a third fewer collisions are predicted[121]. This however, still allows for an increasing number of collisions with increasing temperature and is compounded when the re-evaporation of material from the deposition chamber walls is considered.

As the iron clusters are sputtered onto the TEM grids it follows that some will collide with the walls of the deposition rather than hit the target grids, these particles will then be re-evaporated as molecular iron if the temperature in the deposition chamber is raised such that the atoms can break away from such clusters. This material will then collide with free nanoclusters passing through the chamber and coalesce into larger iron particles. This effect has been seen in the deposition of Au-coated Fe nanoparticles where a second Fe shell was observed under high-resolution STEM. This second shell of iron was attributed to the re-evaporation of iron clusters from the deposition chamber demonstrating that in theory multiple shells may be deposited onto a single particle.

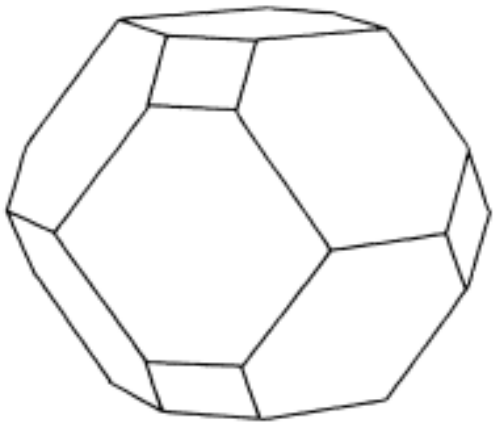

Figure 3.23 Equilibrium shape at T=0K for a BCC crystal composed of {100} and {110} facets[122].

The change in the particle geometry during deposition is likely due to the redistribution of surface atoms due to increased thermal energy. This allows the particle to re-organise its surface atoms to create lower energy configurations which for BCC iron result in a progression towards more spherical geometries which as explored later minimise the surface energy. This will manifest as an evolution of particles towards their equilibrium shape as defined by the Wulff construction, the equilibrium shape for a BCC crystal such as iron is shown in Fig. 3.23. This is supported by the fact that particles deposited at various temperatures show a similar distribution of particle shapes, with more cubic geometries being formed at lower temperatures. As a result, it is common for sample deposited closer to room temperature to consist of cubic and truncated cubic morphologies, while samples deposited at higher temperatures have an increasing number of truncated and rhombohedral particles[123.124].

The transition to the more spherical morphologies is driven by an increase in the size of the nanoparticles as the deposition temperature increases, it was further found that as the particle size increased the geometry became increasingly spherical. It is highly likely that the two changes in physical properties are linked. As outlined previously, the increase in particle size is likely due to the increased number of collisions between iron nanoclusters and molecular iron during deposition caused by the re-evaporation of material from the walls of the deposition chamber. This colliding iron atoms will also possess a greater amount of thermal energy as the deposition temperature is increased leading to a greater chance of spherical clusters forming to minimise surface energy. The resulting particle geometry appears to be a critical factor in determining the future oxidation behaviour of the particle, with cubic structures having been shown to develop significantly strained lattice structures along the side facets to enhance the rates of oxygen anion in-diffusion. On the other hand, spherical particles display oxidation behaviour that results in the formation of large Kirkendall voids that eventually coalesce into a large central vacancy. As the deposition temperature can be used to control the type of morphology that dominates a sample it is possible in principle to exercise a degree particle selection by adjusting the deposition conditions to promote the formation of desirable geometries.

Chapter 4: Cu coated Iron Nanoparticles

One potential method of protecting pure Fe nanoparticles from the effects of increased oxidation is to coat the particle in a shell material that is either resistant to oxide formation or else forms oxides that have little effect on the overall magnetic properties of the particle. The aim as laid out in previous chapters is to create the best performing magnetic iron nanoparticles for magnetic nanoparticle hyperthermia (MNH), MRI contrast, drug delivery and/or magnetic particle imaging (MPI).

In this chapter, the attempted deposition of elemental copper onto the surface of the iron nanoclusters is investigated. The sample characteristics are examined in a similar style to the pure Fe samples in the previous chapter with a focus on how the particles size, shape and oxide thickness evolves with deposition temperature. It was found that the addition of copper material during deposition changed the way the particles change with increasing temperature with the average particle growing larger and more cubic as opposed to spherical. The presence of copper was confirmed through EDX measurements and an attempt was made to determine the location of the copper in the particle; if a copper oxide shell was present or the copper alloyed with the iron at the surface.

The particles were deposited at the University of Leicester (Department of Physics and Astronomy), particles were imaged and analysed using the JEOL 2011 TEM and JEOL 2200 FS (S)TEM at the JEOL York Nanocentre at the University of York. Magnetic data obtained by our collaborators is briefly summarised to provide context.

4.1 Sample Characterisation

Particles were characterised using information extracted from images taken using a JEOL 2011 TEM with high-resolution images taken using a JEOL 2200 (S)TEM. Particles were characterised by their size, geometry and the thickness of the oxide shell that formed post-deposition, sample characteristics are compared against their deposition temperature and where appropriate against other characteristics. Particles in the sample were observed to possess geometries ranging from cubic to spherical. With cubic particles being confined by the six {100} planes and truncated by the twelve {110} planes with different degrees of truncation. As such the geometry was quantified using the ratio of the particles calliper distances (the maximum and minimum between two opposing points on the particles surface). Where geometry is defined as

$$G = \frac{d_{min}}{d_{max}} \tag{4.1}$$

Where d_{min} and $d_{max}$are the minimum and maximum calliper distances of the particle respectively as shown schematically in Fig. 4.1.

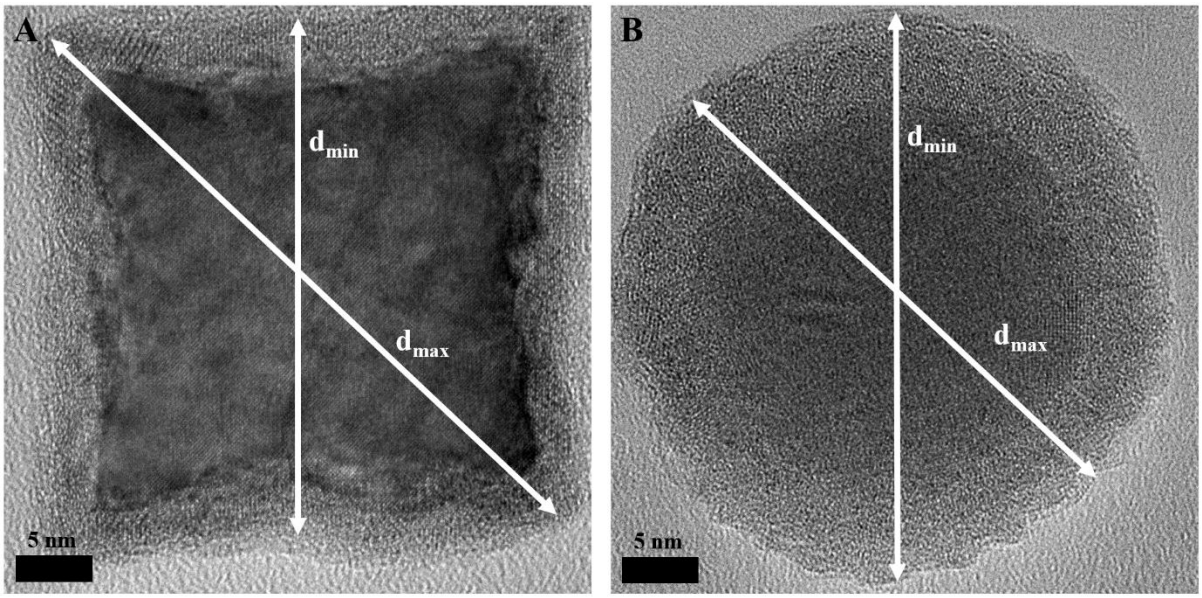

Figure 4.1 Schematic diagram of the particle geometry classifications. Particles in the sample are described by the ratio of the of the minimum and maximum feret diameters such that a perfect cubic particle (this would appear as a square in transmission) would have a ratio of 0.63. A perfectly spherical particle (which would appear as a circle in transmission) would have a value of unity.

To match the geometry ratio as shown above to qualitive descriptions of the particles geometry cubic particles were considered to be those with a ratio of <0.75 and spherical particles were considered to have ratios of >0.90 with particles that fall between these values being described as truncated cubic particles due to their appearance in transmission (Fig. 4.2). The particle sizes were determined by measuring the particles dimensions in ImageJ after binarising the images to remove the background. Images were first converted to 8-bit greyscale and binarised using a threshold value determined by the software's 'max entropy' method which offered the best thresholding values that included the less dark shells[125].

The model is based on Otsu thresholding which separates the image into two classes of pixels: foreground pixels and background pixels. The threshold value is then determined by minimising the inter-class variance of the two groups as determined by the weighted sum of the two variances[126]. The model is useful for thresholding images where the image histogram has a bimodal distribution, in the case of the TEM images used here it is possible to define two separate groups of pixels, those belonging to a particle and those belonging to the background[127]. Particle shell thickness was measured by comparing the particle size determined through the above method with the size of the core determined by setting the threshold manually to encompass only the particles core. Measurements are then compared with the original image to make sure no double particles were counted, the process is highlighted in Fig. 4.2.

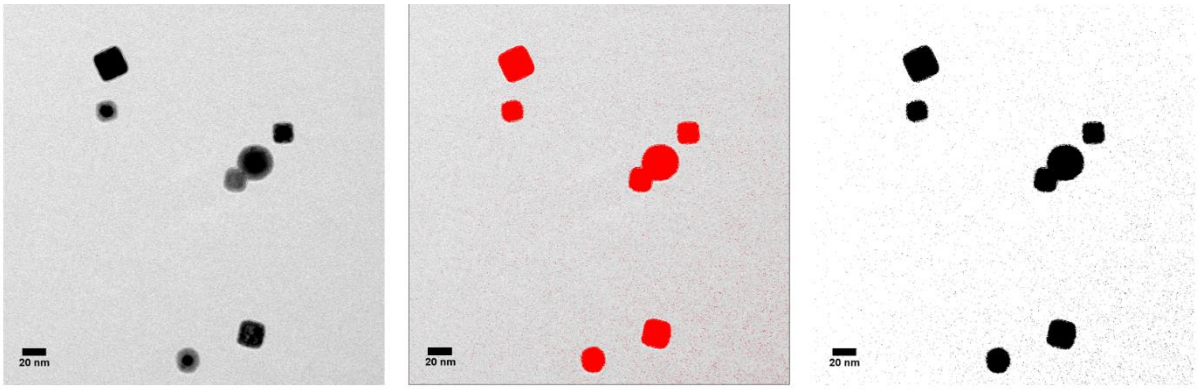

Figure 4.2 A) Bright-field TEM image of Fe@Cu particles, B) image with filter set at the threshold value determined by the Max Entropy method in ImageJ and C) final image after binarisation, measurements obtained are compared to original image to remove anomalies such as the 'double' particle.

Fig. 4.3 shows the distribution of 100 particle sizes for samples deposited at 435°C, 792°C, 978°C and 1191°C, the particles range in size from 10nm to 50nm however large cubic particles are sporadically observed with sizes greater than 50nm. The average particles sizes for the samples were determined to be 15.6±0.8nm, 17.6±0.5nm, 22.5±0.7nm and 24.1±0.6nm respectively and shown as a function of the deposition temperature in Fig. 4.4. The error in measuring the size of an individual particle was determined by comparing the size determined using a threshold value calculated as described above with upper and lower limit thresholds which were measured by hand. The upper threshold limit was determined as the value at which the derived particle size would not increase anymore while the lower limit was determined by the point at which the oxide shell was no longer included in the binarised image. The errors calculated this way were of the order of 1nm. The error in the bin counts was determined by measuring the number of particles that fell within 1nm of the bin edges.

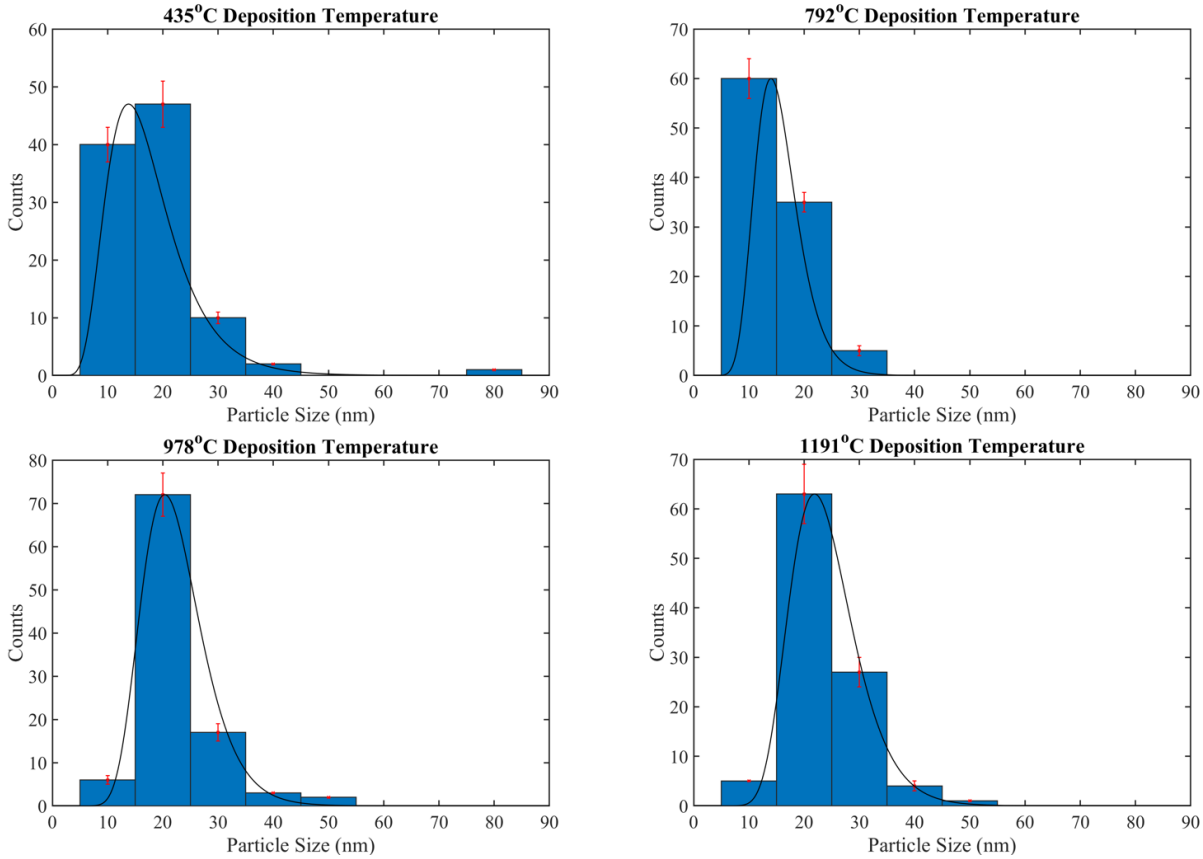

Figure 4.3 Size distribution histograms for samples created at four deposition temperature 435°C, 792°C, 978°C and 1191°C. Average particle sizes were found to be 15.6±0.8nm, 17.6±0.5nm, 22.5±0.7nm and 24.1±0.6nm respectively with the average for each histogram denoted by a black dashed line with 100 particles being measured for each sample.

As with the pure Fe nanoparticles in the previous chapter the average particle size distributions were fitted with lognormal functions with the equation, explained in detail in chapter 3;

$$f(x|\,\mu,\sigma) = \frac{1}{x\sigma\sqrt{2\pi}}\, exp\left(\frac{-(ln(x)-\mu}{2\sigma^2}\right) \tag{4.2}$$

All chi squared tests fell within the significance range stated previously and thus the distributions presented offer a good model for the distribution of particle sizes in the Fe@Cu samples.

Overall the samples show a slight increase in particle size with temperature increasing from 15.6nm to 24.1nm within the temperature range from 445°C to 1191°C. This represents an increase of 54% across the temperature range and is significantly lower than the average particle size increase observed in pure Fe nanoparticles across a temperature range of 419°C. A comparison between the observed increase in the particle size of the pure Fe samples and the Fe@Cu samples is shown in Fig. 4.4.

The range of the deposition temperatures only overlaps at the lower end of the temperature scale, so more data points are needed to draw concrete conclusions. However, the graph does illustrate the difference in the rate of increase of the particle size with increasing deposition temperature. This increase in temperature is expected due to the addition of Cu material to the particle surface resulting in either the formation of a copper shell or a Cu/Fe alloy. Furthermore, absorption of material due to the re-evaporation of iron and copper from the deposition chamber walls should also increase the average size of the particles with higher temperatures resulting in more re-evaporated material. Interestingly a much lower increase in particle size across the temperature range was observed in this case. This effect may be attributed to the difficulty of constructing multiple shelled particles. If the copper adheres to the surface of the iron nanoclusters any re-evaporated iron would have to adhere to the new copper surface. It is possible that this is energetically unfavourable and the contribution to the particle size by re-evaporated material is subsequently very low. This would leave only the addition of copper material (either direct or re-evaporated) as the main driving mechanism behind the increase in the particle size with temperature.

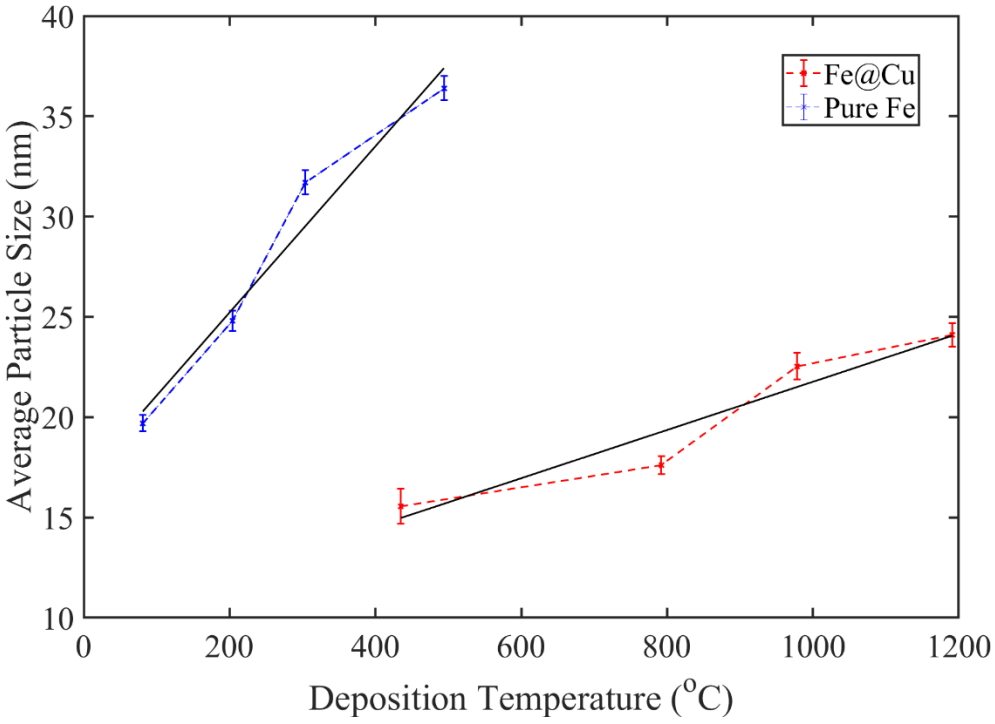

Figure 4.4 Graph showing the comparison between the rate of particle size increase with increasing deposition temperature for Fe@Cu particles (red) and pure Fe (blue). Linear regression fits are used to highlight the difference in the rate of increase as a function of temperature with R^2 values for the fit of 0.96 and 0.91 for the Fe@Cu and pure Fe respectively.

The rate of increase in average particle size can be seen in Fig. 4.4, linear regressions have been plotted to highlight the difference with a gradient (rate of increase in size as a function of temperature) of 0.01 nm/C° for the Fe@Cu particles and 0.04 nm/C° for the pure Fe particles. This represents a 400% decrease in the rate of particle growth through increased deposition temperature due to addition of copper material. The linear regressions had goodness-of-fit R^2 values of 0.96 and 0.91 for the Fe@Cu and pure Fe respectively, suggesting that the linear fit is reliable across the respective temperature ranges. However, as the samples only overlap between 400°C and 500°C more data points would be needed to aid a deeper understanding of how the copper material effects the relationship between average particle size and temperature.

Fig. 4.5 shows the distribution of particle geometries in the samples deposited at 435°C, 792°C, 978°C and 1191°C, unlike in the pure iron samples, which displayed a clear evolution towards spherical geometries the overall geometry

of the samples has remained constant. The average particle geometries can be seen in Fig. 4.6 with all average geometries lying within the truncated cubic to spherical range. Given that this behaviour differs from the pure Fe samples which experience significant changes in the average particle geometries during deposition based on the temperature this suggests the addition of Cu material has a significant effect on the properties of the sample. The average shape of the particle when was roughly hexagonal with the majority of particles deposited at higher temperatures possessing roughly equally sized {100} and {110} facets as seen in Fig. 4.7. Furthermore, as shown in the histograms in Fig. 3.5 there appears to be a decrease in the number of highly spherical particles (geometry ratio >0.9) as the deposition temperature is increased.

The distributions in Fig. 4.5 were fitted using the two-parameter Weibull distribution as this was found to match best with the data when the chi squared goodness-of-fit tests were performed against normal and lognormal distributions. The distribution for the average particle geometry mirrors the distribution for average particle size, in that the former case shows a clear negatively skewed distribution (right-of-centre sew). Whereas the lognormal distribution shows a 'skew' to the left-of-centre. The Weibull distribution is often used to describe very narrow particle size distributions as it predicts far fewer smaller particles than the standard lognormal distribution. The distribution is also commonly found in the analysis of life data and product reliability however, the distribution is highly flexible and can be fit using the expression in Eq. 4.3.

$$f(x \mid a, b) = ba^{-b}x^{(b-1)}exp\left(-\frac{x}{a}\right)^2 \tag{4.3}$$

Where the parameters a and b represent the scale and shape parameters respectively, with the former describing the spread of the distribution and the latter describing the shape. In the case of the scale parameter a larger value indicates a larger spread, one the other hand, the shape parameter denotes the skew of the distribution. A shape parameter between 3 and 4 results in a bell-curve similar to a normal distribution while a parameter value greater than this results in a negatively skewed distribution like those shown in Fig. 4.5. The goodness-of-fit or the distributions was determined using the chi squared test as described previously. In all

cases the distributions were found to lie within the 5% significance band suggesting a that the distributions offer a good description of the observed data.

Across the range of temperatures there was no significant change in the particles average geometry with the samples average values lying between 0.87 and 0.89, this represents a very narrow range of morphologies with the particles in this region being highly truncated. Whereas the particles in the region between 0.7 and 0.8 are often characterised by the presence of sizeable {110} facets these facets remain smaller than the {100} facets when observed in transmission. The Fe@Cu particles observed here however adopt geometries where the {100} and {110} facets are of roughly equal length.

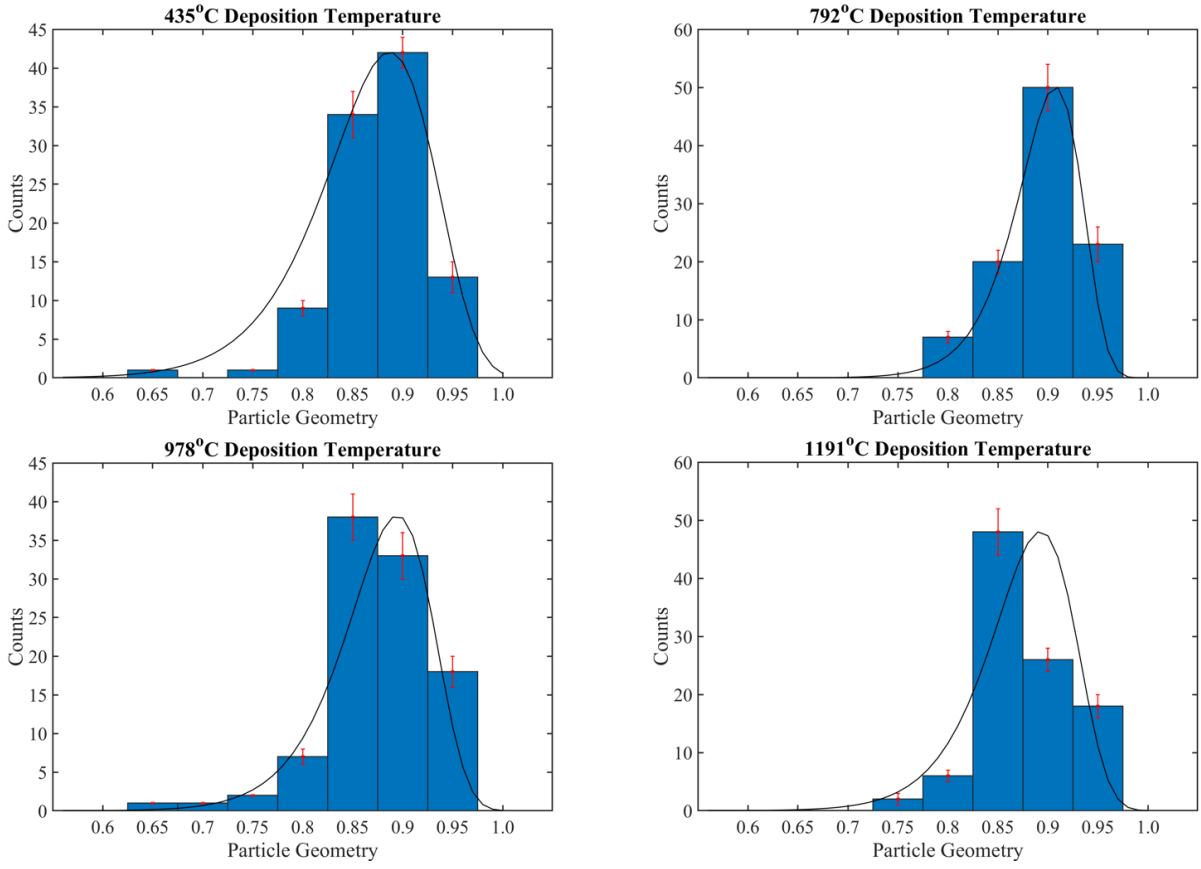

Figure 4.5 Geometric distribution histograms for samples created at four deposition temperature 435°C, 792°C, 978°C and 1191°C. Average particle geometries were found to be 0.874±0.005, 0.892±0.004, 0.875±0.005nm and 0.874±0.004nm respectively with the average for each histogram denoted by a black dashed line with 100 particles being measured for each sample.

The errors for the histograms in Fig. 4.5 were calculate in the same manner as the histograms in Fig. 4.3 where the average error in the measurements for the geometry ratio was found to be ±0.01. The errors for the averages in Fig. 4.6 were calculated from the standard error in the mean. To investigate the effect of the deposition conditions on the geometry further the relationship between the particle size and the particle geometry was examined by comparing the values for all 400 particles across all samples (Fig. 4.7). The result shows a largely uniform distribution of the majority of particles between geometry ratios of 0.75 and 0.95 with sizes between 10nm and 40nm. However, it can also be seen that almost all the highly cubic structures are larger particles, as the average particle size increases slightly with deposition temperature it is possible there is increase in the number of cubic particles alongside this in hotter samples.

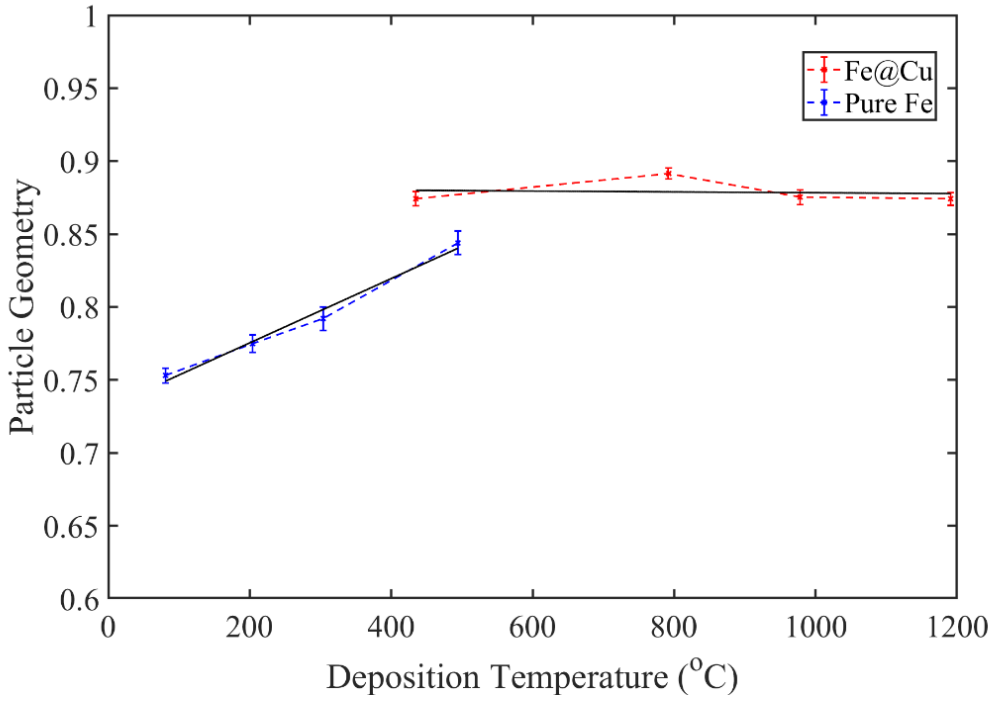

Figure 4.6 Graph comparing the change in average particle geometry with increased deposition temperature for Fe@Cu particles (red) and pure Fe (blue). Linear regressions were fit to show the lack of significant evolution in average geometry in Fe@Cu samples compared to the cubic to spherical transition observed in pure Fe particles. Regressions had a goodness-of-fit R2 value of 0.98 for Fe@Cu and pure Fe.

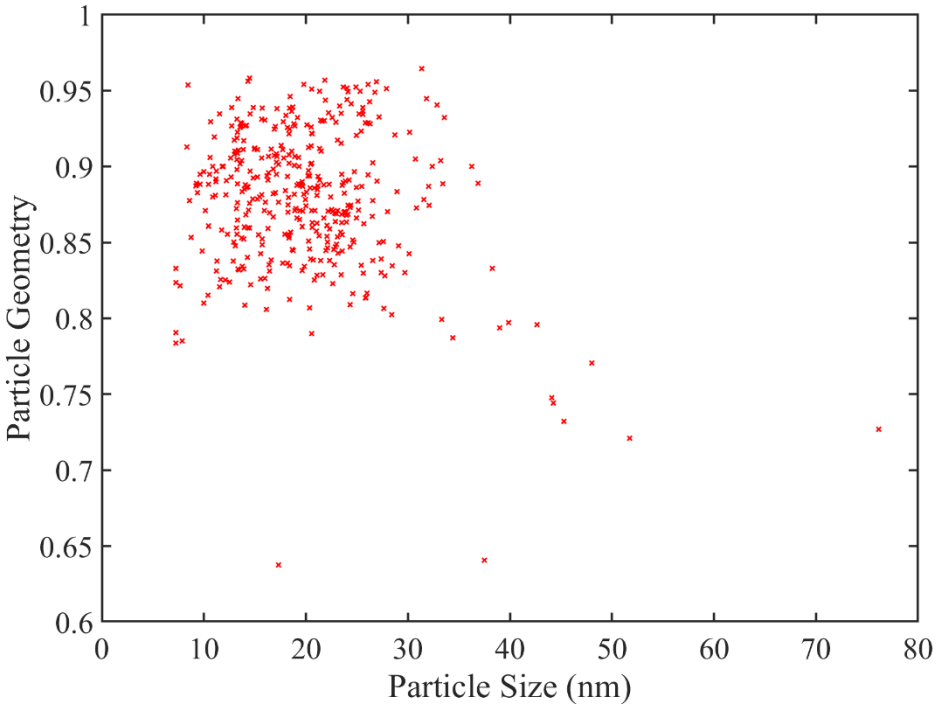

Figure 4.7 Particle geometry ratio against particle size for 400 nanoparticles deposited at a temperature range of 435°C to 1191°C with dashed lines to highlight the qualitive descriptions of the particle shapes with cubic particles (<0.7), truncated cubic particles (0.7<x<0.8) cuboctahedral particles at (0.8<x<0.9) and spherical particles (>0.9).

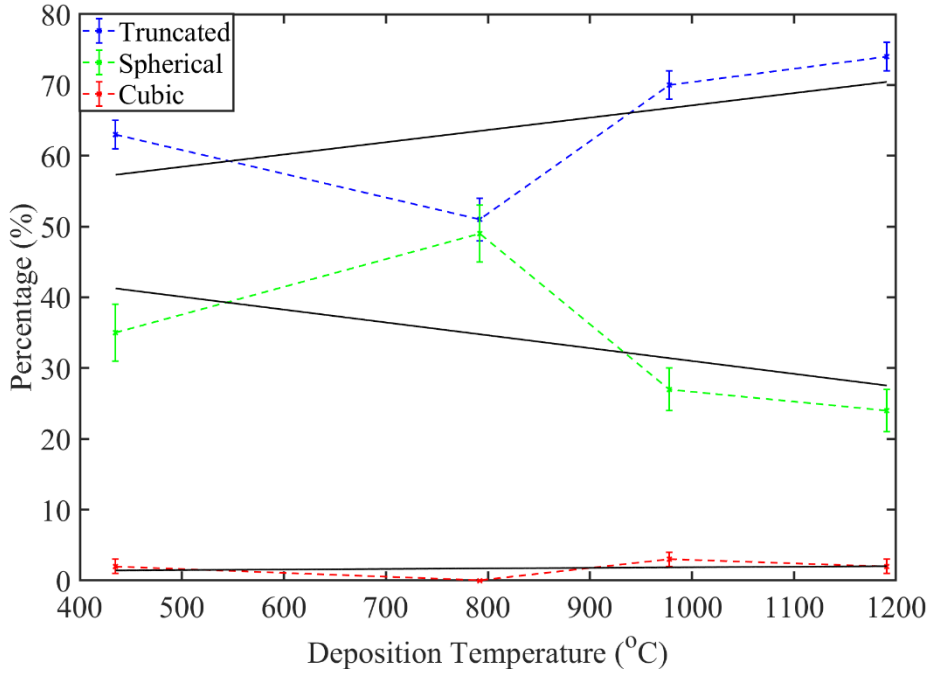

Figure 4.8 Graph showing the variation of particle geometries across the different deposition temperatures with cubic particles (red), truncated particles (blue) and spherical particles (green) with dashed lines to aid the eye. Line regressions are fitted to aid the eye.

Fig. 4.8 shows the change in the percentage of particles adopting cubic (<0.75), truncated (0.75<x<0.90) or spherical (>0.90) geometries with increasing deposition temperature. It can be seen from the graph that the most dominant geometry is that of truncated cubic (hexagonal as viewed in transmission) particles. The least common type of particle is the cubic particle. However, it is interesting to observe that as the deposition temperature is increased the percentage of truncated cubic particles increases. This is the opposite of what was observed in pure Fe particles where the number of cubic and truncated particles decreased rapidly as the number of spherical particles rose. For Fe@Cu particles however the reverse is observed with the number of spherical and truncated particles decreasing and the number of cubic particles increasing. This is likely linked to the gradual increase in size caused by increased temperature coupled with the observation that the largest particles tend to adopt cubic geometries. This can be shown in greater detail in Fig. 4.9 where the percentage of cubic, truncated, and spherical particles is shown as a function of particle size. The figure shows a clear and significant increase in the percentage of larger particles that adopt cubic geometries, with the percentage of truncated and spherical geometries decreasing sharply with increased particle size.

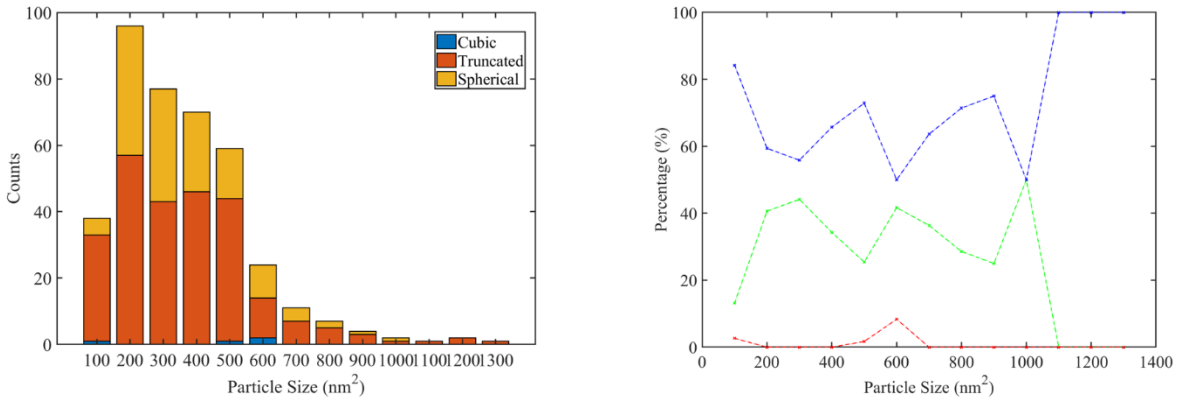

Figure 4.9 Distribution of particle geometries across different particle sizes with histogram (left) showing the distribution of cubic, truncated, and spherical particles and the percentage of particle for each size range that each geometry classification makes up (right) with cubic (red), truncated (blue) and spherical (green) particles with dashed line to aid the eye.

The drastic change in behaviour of the Fe@Cu nanoparticles compared to pure Fe particles suggests that the addition of copper material into the nanostructures has a major effect on the nanoparticles at higher deposition temperatures. The main difference is in how the evolution of particle geometry from cubic to spherical particles does not occur after the addition of Cu material. A potential explanation of this could be the reduction in surface energy of the nanoparticles resulting in higher temperatures being needed to drive particle geometries to more spherical shapes. This is supported by the fact that the percentage of truncated cubic particles does not decrease with increasing deposition temperature while the percentage of spherical particles does. The lowest energy close-packed surface in FCC Cu is the (111) and has a surface energy of 1409 Jm^{-2} which is far below the surface energy for the lowest energy surface in BCC Fe (110) which is 2123 Jm^{-2}[128,129]. As such the addition of copper material onto the iron nanoclusters will serve to lower the total surface energy of the particle in the event of a Cu shell forming or alloying of the Fe and Cu material. The ability to retain the cubic geometries of particles despite deposition at higher temperatures is a useful feature, as mentioned in chapter 1 cubic particles have desirable catalytic properties as well as packing density and orientability[130].

4.2 EDX Results

EDX was employed to first determine the extent to which uptake of copper onto the iron clusters has occurred. This spectroscopic method in conjunction with electron microscopy provides an excellent method for determining the element composition of samples with nanometre resolution. A theoretical treatment of the technique is given in Chapter 2 and will only briefly be described here in terms of the EDX functions used. The data presented here was taken from the samples created at 435°C, 792°C, 978°C and 1191°C, the EDX functions used were as follows.

1) EDX *'point and shoot'* scans were performed to obtain EDX spectra of the localised area around the particle This was done to create a background reference for the determination of the copper content. The advantage of this method is to allow for spectrum acquisition from small areas within the

region of interest. This however, comes at the cost of signal-to-noise ratio. If the region is too small or the element of interest too sparsely distributed these small-area EDX scans may not be sensitive enough.

2) EDX line-scans were obtained across the areas of the nanoparticle comprising shell and core, the aim of which was to determine if a noticeable increase in copper signal was detectable across the shell.

3) Lastly EDX maps were created over the course of 30 minutes per map to attempt to detect the if the copper was homogeneously distributed around the particle or concentrated at the 'edges'. This would suggest the formation of a shell while the former case would be more suggestive of alloying.

Fig. 4.10 shows the EDX spectra gathered for a particle in the coldest sample (deposition temperature of 435°C) alongside the spectra corresponding to the background region. The particle measured was between 30-40nm in diameter with a spherical geometry. The spectra for the background region shows the expected mix of C, Ni (Ni TEM grids were used as opposed to standard Cu ones), and Si, as these elements are all present in the sample and expected as background. For instance, the carbon signal is likely generated from the support film which for these samples was a holey-carbon support. The nickel and silicon signals are due to the TEM grid and the TEM holder respectively. Interestingly there is a small amount of copper picked up in the background regions, this signal is small but consistent and was determined to be approximately 0.04±0.01% of the elemental weight and 0.01% of the atomic weight of the signal from both background regions. This suggests that there has been some degree of elemental copper deposition that has occurred. This is likely due to not all the copper being absorbed onto the iron clusters during deposition and as the clusters move through the shell evaporator region of the deposition chamber some elemental copper will be deposited alongside the clusters. Elemental copper is likely to be deposited onto the TEM grid along with the nanoparticle clusters. Interestingly this signal is present in the background regions regardless of temperature and remains at a very consistent atomic percentage.

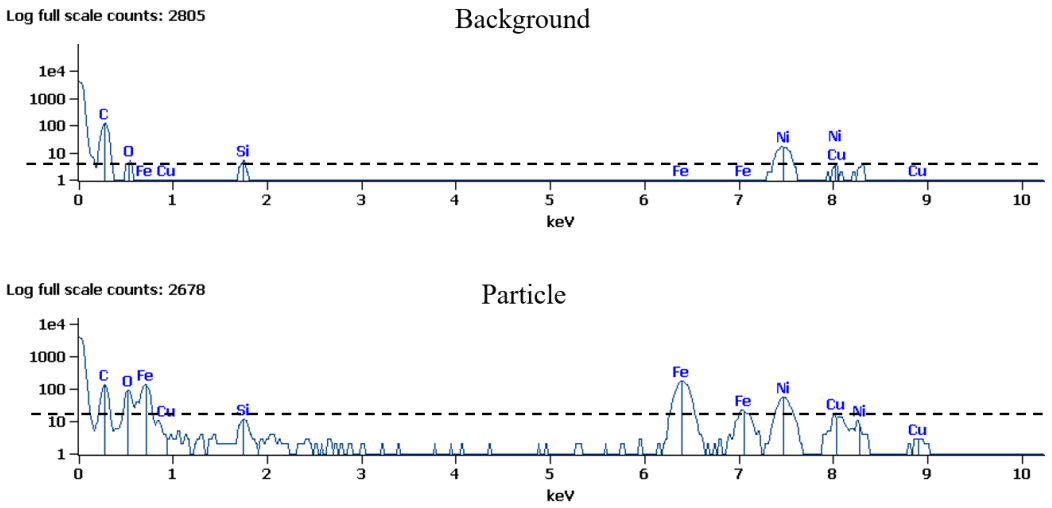

Figure 4.10 EDX spectra for a random particle for the 435°C deposition temperature sample with spectra taken from a background (top) and particle (bottom) region, with characteristic peaks labelled. The intensity of copper peak has been denoted by a black dashed line to highlight the increase in the copper signal from background to particle regions.

When compared to the spectra collected from the region of interest we can see the addition of O and Fe peaks as expected, the origin of the iron is obvious as the core of the particle will be made purely of iron. With the oxygen coming from the oxidation that will invariably occur when the sample is removed from the deposition chamber and exposed to air. It is not possible with this current technique to determine if the oxide comes from iron oxide (likely magnetite) or copper oxide. It is also noticeable that the copper peak in the region of interest spectra is significantly more pronounced. This suggests that there is an increase in the amount of copper being detected in the region corresponding to the nanoparticle. This comparative increase in the copper signal from the nanoparticle over the signal from the background region is present across all samples and for all particles. This suggests that there has been a consistent degree of copper uptake onto the particle as desired. Interestingly the amount of copper detected from the nanoparticle region varies greatly with deposition temperature (Fig. 4.11). This variation of copper content as measured through the analysis of the EDX spectra suggests that the both the coldest and hottest samples (377°C and 1131°C respectively) have the largest copper-to-iron ratio with an atomic weight for copper of 20.96±2.38% and 16.40±4.23% respectively.

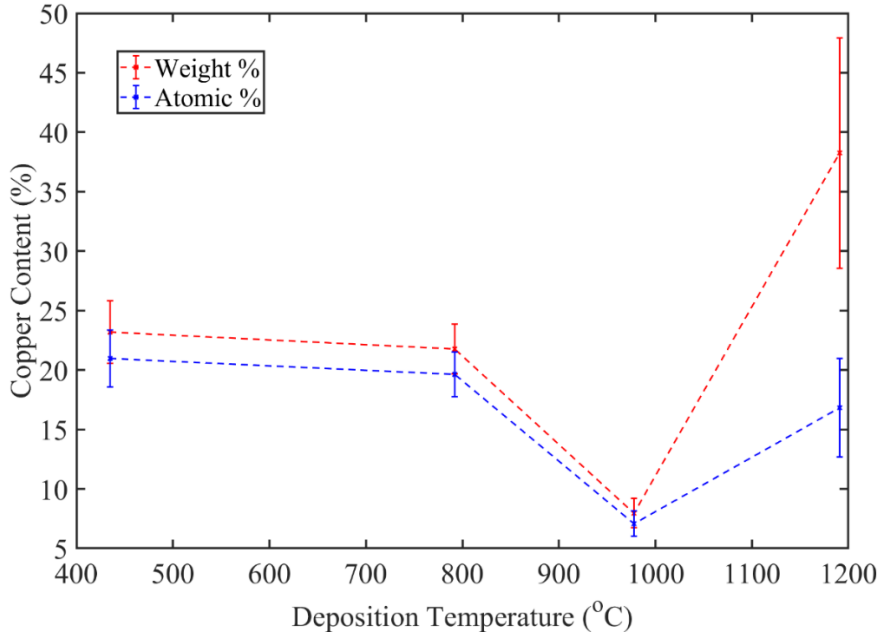

Figure 4.11 Graph displaying the copper content as a percentage of the signal from the particle, signal is filtered to show copper content as a percentage of the combination of Cu, Fe and O signal with the weight percentage (red) and atomic percentage (blue).

For a nanoparticle with an iron-core and a diameter of 30nm, which represent good approximations of the average particle in the sample. Having an atomic copper percentage of 21% would result in the formation of a homogeneous copper shell with the thickness of a few monolayers. It should be noted however that the formation of such a homogeneous shell is unlikely as spectra gathered from different areas along the edge of the nanoparticle result in wildly varying amounts of copper detected as can be seen in Fig.4.12. While such scans are highly sensitive to drift, as even a small particle movement may take it out of the scan region and such small regions generate very little signal.

To attempt to determine the location and concentration of the copper in the sample EDX maps were generated of a collection of particles in each sample, the resulting maps are displayed in Fig. 4.13. The maps confirm the idea that there is a distribution of copper across the whole sample as observed in the background spectra, as mentioned this is likely due to leakage of Cu material from the core-shell evaporator into the deposition chamber. This would result in the deposition of elemental copper on the TEM grid and explain the observation made here.

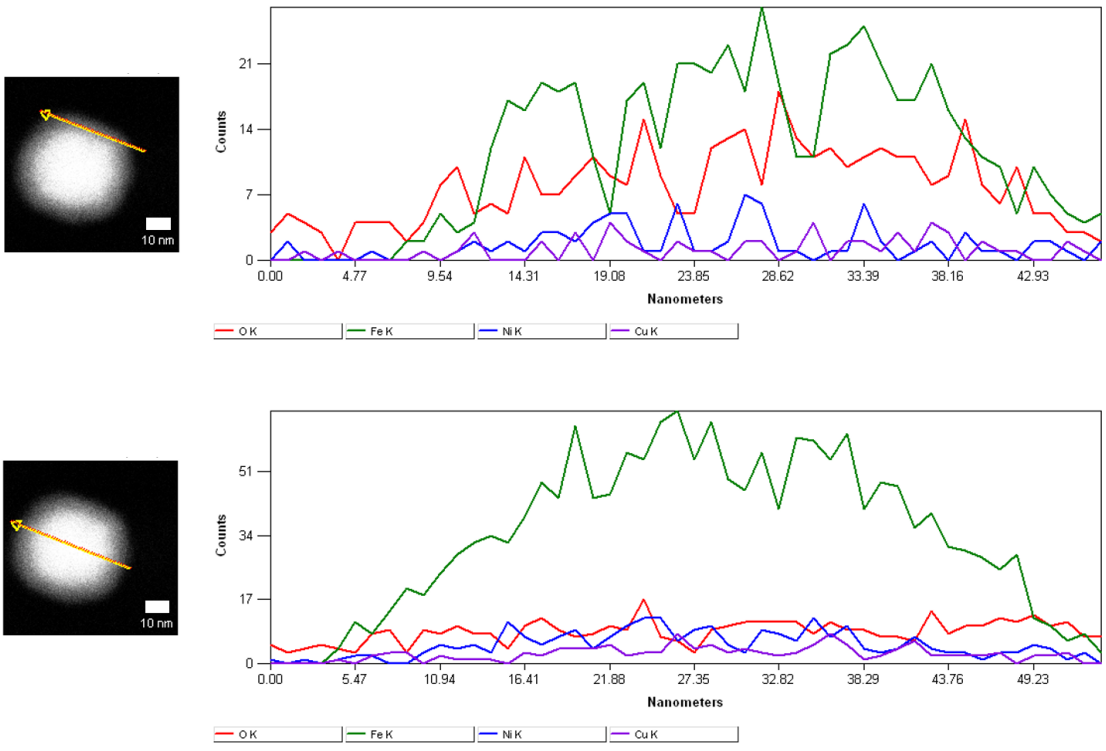

Figure 4.12 EDX linescan spectra the core and shell regions of a particle in the coldest sample (435°C deposition temperature) with oxygen signal (red), iron signal (green), nickel signal from the TEM grid (blue) and copper signal (purple).

Fig. 4.13 also shows an increase in copper signal within the area of the particle, this has been highlighted qualitatively by comparing the density of signal in the EDX maps in the particle region (highlighted by the dashed lines) and the background. As can be seen by in Fig 4.13 the particle region is marked on the EDX maps by a black dashed line, it should be noted, that drift has not been accounted for. As can be seen in Fig. 4.13 the Cu signal inside the particle region is significantly larger than that outside the region suggesting a degree of copper uptake by the Fe@Cu nanoparticles. This suggests that there has been a degree of copper uptake by the Fe nanocluster and although it is not possible to determine if the material has formed a shell or alloyed (more likely) with the Fe material, the increase in Cu signal generated in the particle region is a positive result.

Overall the EDX analysis of the samples shows that the presence of the Fe material is confined to regions corresponding to a Fe@Cu particle. This is useful as it suggests that the particles are being deposited with little to no elemental iron in the molecular beam, indicating that all the iron material in the core shell is forming

clusters. As such this can imply the presence of little to no elemental iron in the molecular beam, suggesting that the main method for particle size growth during deposition as shown in both pure Fe and Fe@Cu particles is the re-evaporation of material from the walls. Furthermore, there is enough increase in the Cu signal around the particle regions to suggest that a degree of uptake has occurred although it is unlikely that a full 'protective' copper shell has formed around the iron nanocluster. This is further supported by the fact that the copper content does not show any significant variation across the width of the particle. This is more consistent with the idea of alloying than with shell deposition where it would be expected for the copper to aggregate around the particle edges and for signal to be increased there. This is not present in Fig. 4.12 or 4.13 where the copper signal is largely homogeneously distributed with an increase in density around the particle regions. To investigate this further it is possible to use high-resolution images gathered in TEM and STEM modes to compare the lattice spacings in the particles shell with the expected lattice spacings for copper and iron oxides.

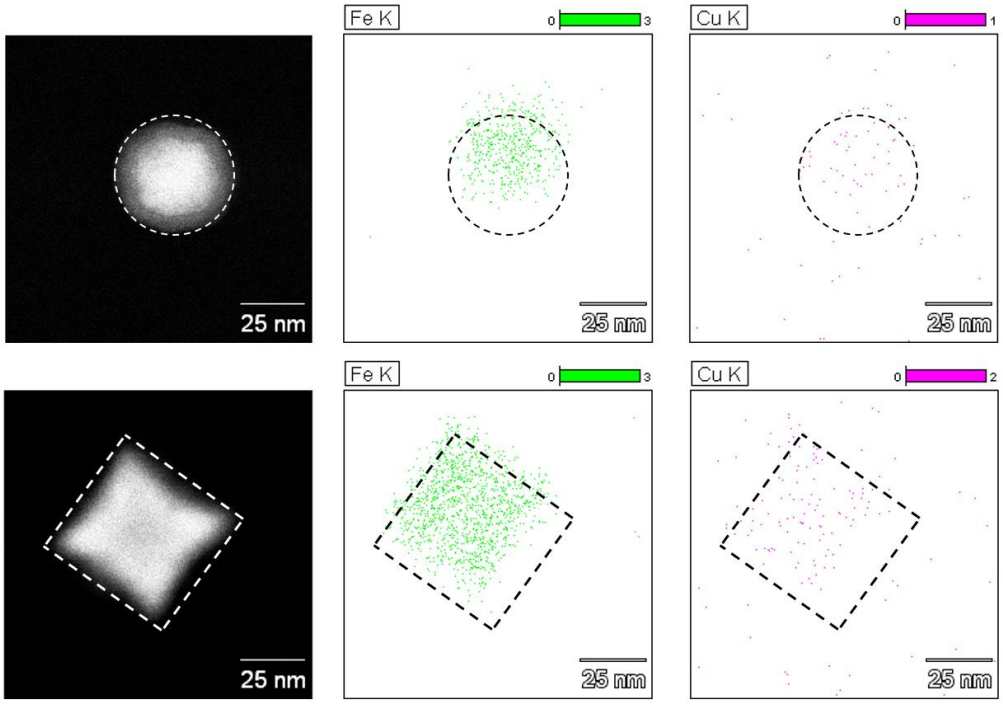

Figure 4.13 EDX maps of two particles with spherical (top) and cubic (bottom) geometries, particle region has been marked by dashed lines on both the HAADF image and the maps for Fe (green) and Cu (purple). The effect of particle drift has not been accounted for but can be seen clearly in the EDX maps with the signal generated from the particle drifting outside of the dashed line. EDX maps were created over a period of 15 minutes with both Fe and Cu maps generated simultaneously.

4.3 Magnetometry

As with the pure Fe samples in chapter 3 magnetometry information was obtained using a SQUID magnetometer and analysed by our collaborators at the University of Leicester. The data presented in this section was reproduced with permission to add context to the discussion surrounding the production of coated Fe@metal nanoclusters. A description of how the magnetometry data is analysed is provided in chapter 3 with the plots shown in Fig. 4.14 displaying the magnetisation curves of thee samples with deposition temperatures of 442°C, 774°C and, 1137°C deposited on Si (100) substrates. The plots show the magnetisation curves across field ranges from -5T to +5T and -1T to +1T respectively. Unlike with the pure Fe samples there is no significant change in the magnetic response or hysteresis of the particles with the curves for samples at 5K and 300K shown. The data was taken as a measurement of the total sample moment (emu) as a function of the applied magnetic field at the two temperatures mentioned (5K and 300K). The magnetic moment is expressed in Fig. 4.14 as the moment per gram of iron with the mass of iron determined by XTM measurements during and after the sample deposition.

As with the iron samples the saturation magnetism was determined by fitting Langevin functions such that;

$$L(x) = \coth(x) - \frac{1}{x} \tag{4.4}$$

The Langevin function was used as the classical limit of the Brillouin function that describes the dependency of the magnetisation M on the applied magnetic field for a collection of non-interacting paramagnetic atoms or ions. The exchange interaction of the atoms locks the atomic moments so that the Fe nanoparticles act as a single magnetic moment, as such it will behave as a classical magnetic dipole. The saturation magnetism is shown in Fig. 4.15 and unlike with the pure Fe samples does not seem to decrease with higher deposition temperatures. However, this conclusion is not certain as more data points are needed to confirm the magnetic behaviour at higher deposition temperatures. Furthermore, there is not a major difference between the saturation magnetism of the pure Fe and Fe@Cu samples, this could imply that the diamagnetic copper does not interfere with the

ferromagnetic Fe. This is useful as the presence of the Cu material has a significant effect on the physical properties as a function of deposition temperature as discussed previously. As such it may be possible to tailor the physical properties of the samples through the addition of metallic material onto the surface of the Fe nanocluster while maintaining the desirable magnetic response characteristic of iron nanoclusters.

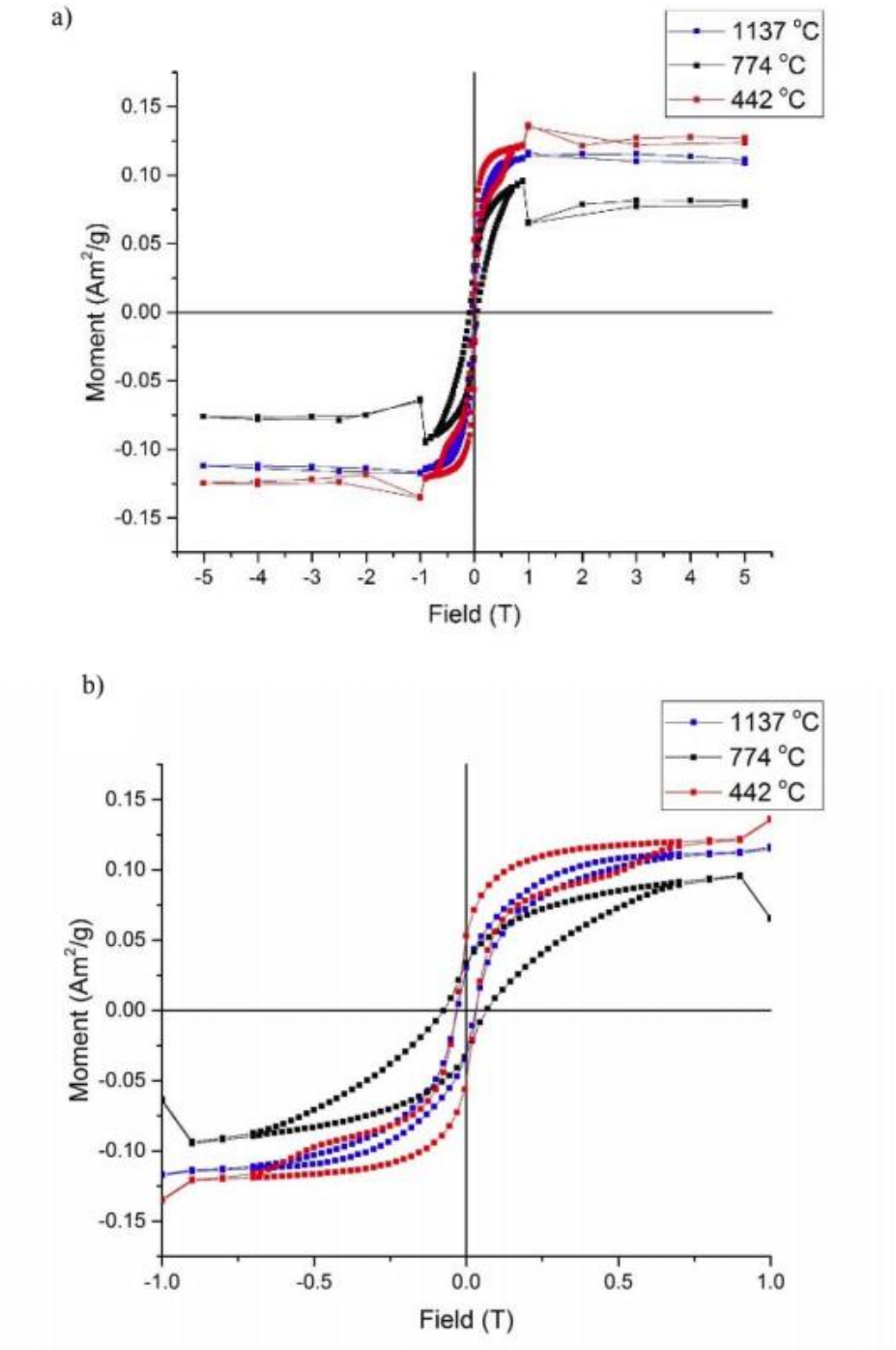

Figure 4.14 Raw magnetometry data obtained via SQUID and processed by collaborators at the University of Leicester (reproduced with permission)[102].

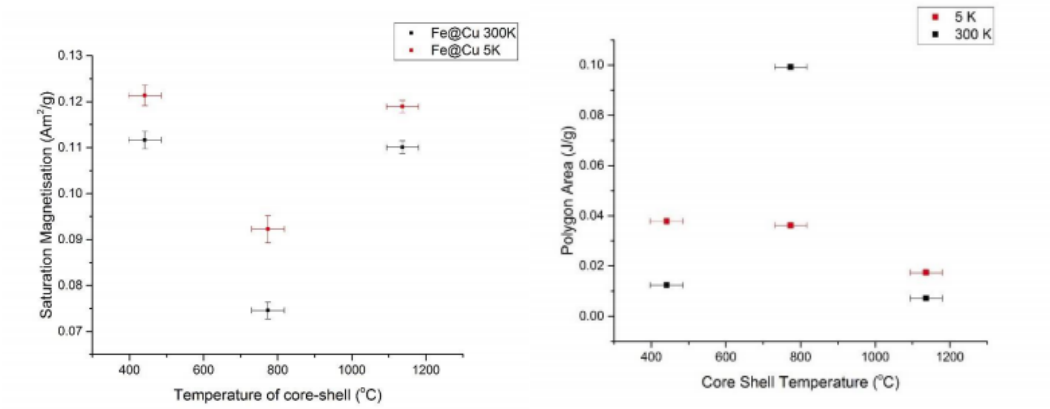

Figure 4.15 A) Saturation magnetism calculated through Langevin fitting of the raw hysteresis curves and plotted as a function of deposition temperature, B) calculated area subtended by hysteresis curve showing a rough prediction of expected heating output of the particles in the sample as a function of deposition temperature. (Reproduced with permission)[102].

Chapter 5: Investigation of Oxidation Pathways

The coating nanoparticles with metallic, protective shells is one potential method to control the oxidation process of the pure Fe nanoparticles as the addition of copper material has been shown to preserve cubic geometries at higher deposition temperatures. However, much more work needs to be done on identifying, depositing, and analysing various potential coatings. As such understanding the oxidation pathways of the pure Fe nanoparticles is important for building a fuller understanding of nanoscale oxidation.

The oxidation of cubic nanoparticles has been studied as described in chapter 1 as such the oxidation mechanisms that govern the process in spherical particles is examined in this chapter. To this end the diffusion co-efficient of the particles in the samples is estimated statistically based on the observed oxidation behaviour post-annealing. This is then discussed in context of the diffusion along the grain boundaries that are more common in spherical particles.

Particles were imaged and analysed using the JEOL 2011 TEM and JEOL 2200 FS (S)TEM at the JEOL Nanocentre at the University of York.

5.1 Effect of Annealing

5.1.1 Increase in Average Particle Size

After annealing at 200°C for 15 minutes the average particle size increased from 19.7nm to 36.4nm with a range of sizes between 10nm and 50nm prior to the annealing and a range of sizes between 20nm and 100nm afterwards. The increase in size across the temperature range can be attributed to the increase in the oxide shell thickness due to oxidation. We can estimate the increase in the oxide shell and therefore the increase in the particle size due to oxidation by comparing the sample averages before and after annealing. Assuming an average particle before annealing undergoes oxidation and fully oxidises its iron core then we can estimate the expected amount of oxide this process would add assuming that iron transported to the surface is immobile and instantly oxidises. As such this estimate provides an over estimate of the contribution to the particle size increase due to oxidation. The number of atoms in the iron core can be estimated by comparing the volume of the core to that of the α-Fe unit cell.

$$N_j = \frac{V_j}{V_0} \times n \tag{5.1}$$

Where N_j is the number of atoms in either the core or shell, V_j is the volume of the core or shell and V_0 is the volume of the unit cell while n is the number of atoms in the unit cell (2 for α-Fe). In the case of the completely depleted core then the number of atoms that have diffused out to the surface for oxidation is equal to the number of atoms in the core. As such the theoretical increase in the oxide shell based on the assumption that all the iron atoms stay on the surface and oxidise can be calculated.

$$V_{oxide}^{f} = \Omega \times N_c \tag{5.2}$$

Where the final volume of the oxide is equal to the amount of oxide formed per atom (Ω) and the number of atoms in the core (N_c). In the case of fully oxidised particles with both ‘hollow’ and ‘non-hollow’ cores the increase in the amount of oxide from an original average of 3.1nm was compared with the potential increase in the oxide thickness due to full oxidation of the core. Furthermore, it is important to

consider the direction of the oxidation front, it was discussed in chapter 4 that the relative rates or iron and oxygen diffusion determine the direction of the oxide shell growth; outwards from the oxide/gas interface, or inwards from the metal/oxide interface. In practice, there will be non-zero growth at both interfaces however, for simplification only the dominant direction will be considered.

In the case of 'hollow' iron oxide nanoparticles it is clear that oxidation is dominated by growth at the oxide/gas interface due to the large central Kirkendall void (~ 60% of the particle). A simple model for the amount of oxide growth assumes that oxidation proceeds only through the oxide/gas interface as such this allows the position of the original metal/oxide interface to be estimated as the position of the void/oxide interface in the particle and from this the size of the iron core to be determined. For an average 'hollow' particle of 32.21nm with an oxide shell of 6.6nm this predicts an iron core of 19nm which would provide enough iron material to result in the out-diffusion of $2.46 \times 10^6\ atoms$ if the whole core is depleted. This would result in the formation of $6.1 \times 10^4\ nm^3$ of additional iron oxide which for this particle should result in an oxide shell of 6.16nm.

This prediction is within 10% of the observed average shell thickness and is consistent when expanded across a number of observed 'hollow' nanoparticles. The predicted oxide shell based on the assumption of an immobile metal/oxide interface and the complete oxidation of iron material on the surface of the particle is shown in Fig. 5.1. The difference between the observed thickness and predicted thickness is also shown in Fig. 5.1. As such it is likely that in the case of 'hollow' iron oxide nanoparticles there has been a fast diffusion of iron material out of the core with a significantly slower rate of oxygen in-diffusion as is traditionally claimed. As such the idea that the change in particle size is driven by the increase in the oxide shell thickness holds for 'hollow' iron oxide particles.

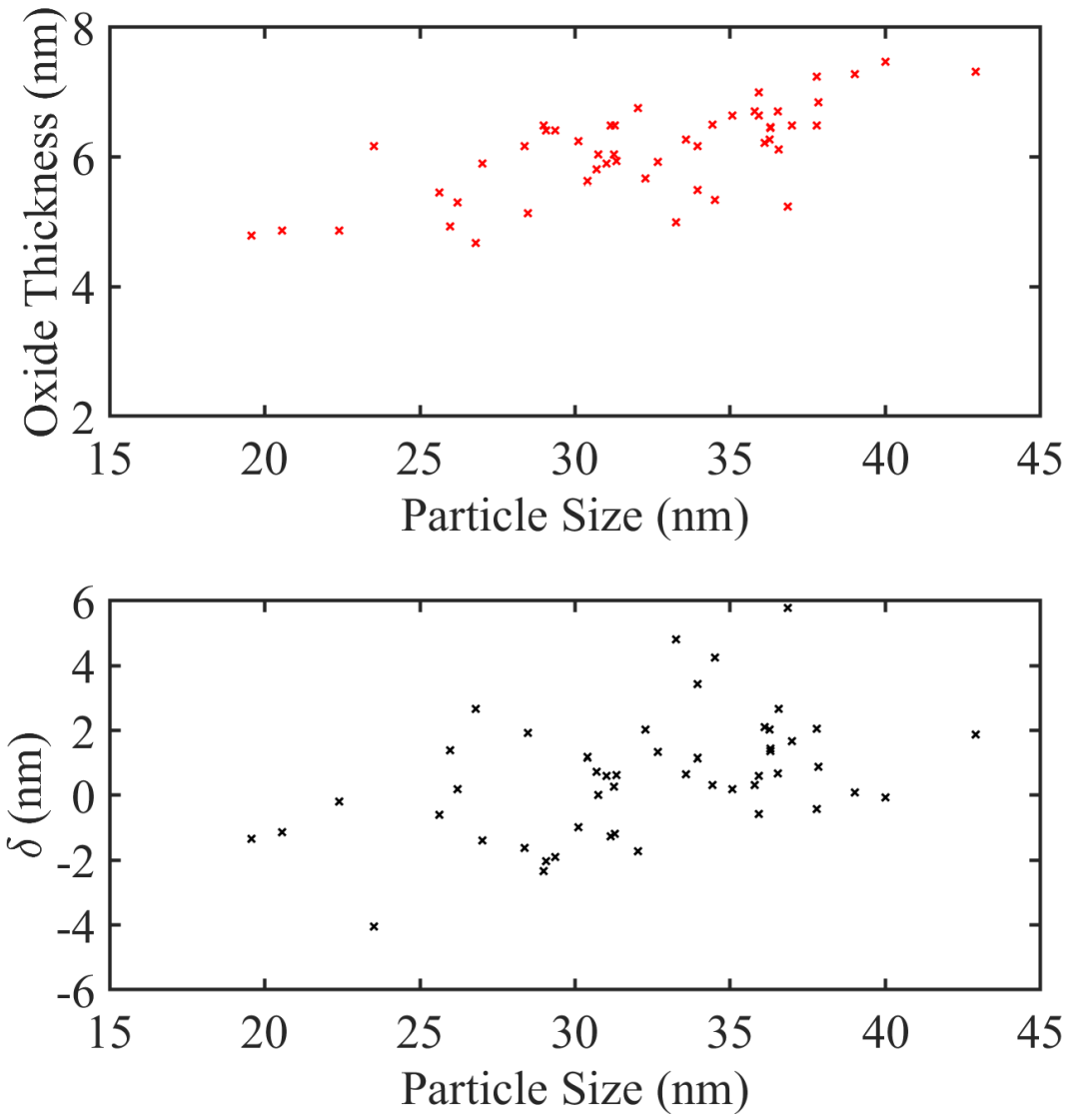

Figure 5.1 Predicted oxide thickness (red) for 50 'hollow' iron oxide nanoparticles assuming oxidation proceeds outwards from the oxide/gas interface and the difference between the observed thicknesses and the predicted values (black).

5.1.2 Evolution of Particle Shape

It is clear from chapter 3 that the particles have undergone significant morphological changes after heating resulting in a complete lack of cubic and truncated cubic particles remaining in the sample. The resulting sample is composed of almost purely spherical particles (geometry ratio of >0.85); this average is derived from the geometry of the whole particle and as can be seen best in the dark field

images the geometry of the core does not always match that of the shell. This is likely dependent on the original morphology of the particle in question as material added in oxidation will be distributed in such a way to create the lowest surface energy configuration (spherical) resulting in the highly spherical oxide shells. However, material is not added to the core but is rather being lost and is hence less able to re-arrange from a previously cubic iron core to a spherical one. Therefore, it seems likely that in the case of particles large enough to oxidise only partially under heating that forming oxide ridges, if the particle was originally cubic, it retains a more cubic core geometry after heating. For this group of partially oxidised particles, the resulting iron core after heating can in some case retain a certain degree of its morphology with some of these particles possessing highly truncated cores. The truncated cores in these particles are similar, in nature, to the highly truncated particles before heating in that they are terminated by 6<100> planes and truncated by 12<110> planes. It should be noted that no particles were found with perfectly cubic cores or cores with only slight truncations. In the cases where the core was found to not be perfectly spherical it was highly truncated cubic with very large <110> side facets.

Cubic particles have been shown to contain mostly monocrystalline side facets, the only grain boundary dense regions of the oxide shell will be at the corners. Spherical particles, on the other hand, will have shorter side facets and more breaks in the oxide shell where grain boundaries will form. It follows that particles that began as spherical particles will oxidise faster than those that began as cubic shaped particles and will be more likely to oxidise fully.

The shift in the sample from cubic particles to spherical particles can be explained based on surface energy minimisation. It has been long established that a system will attempt to arrange itself such that the Gibbs free energy of the system is a minimum. Where the Gibbs free energy is defined as;

$$\Delta G = \sum_j \gamma_j A_j \tag{5.3}$$

Where γ_j is the surface energy and A_j is the area of the surface/crystal plane and ΔG is the difference in energy between a real crystal composed of many molecules with a surface to that of a similarly configured number of molecules in an

infinitely large crystal. As such the quantity ΔG is representative of the energy associated with the surface. In practical terms it represents the energy required to form 'dangling bonds' at a crystal surface and can be estimated as the total energy required to add an atom or molecule to that surface. The definitions of surface energy and its counterpart surface tension are dependent on the phase of the material in question, for a solid such as a nanoparticle the surface energy can be described as the reversible work with which a new surface can be created at constant volume, temperature, and chemical potential μ. When considering the addition of material to a nanoparticle through oxidation it follows that the material will be distributed at the most energetically favourable locations. As such the growth rate of the particle's crystal planes can be in this way linked to their surface energies in that the largest facets of a crystal will be the planes with the lowest surface energy (ie. low index facets such as (100) and (110) for BCC crystals). In the case of BCC α-Fe the surface energy of its lowest order planes is well studied[131]. The typical approach to calculating the surface energy of a crystal plane is to use the slab model, wherein a supercell of a crystal is orientated to the plane of interest and atoms are removed to form a vacuum. For a given slab the surface energy can be defined as;

$$\gamma_{(hkl)} = \frac{E_{slab}^{(hkl)} - E_{bulk}^{(hkl)} \times n_{slab}}{2A_{slab}} \tag{5.4}$$

Where $E_{slab}^{(hkl)}$ is the total energy of the slab for a given Miller index (hkl) and $E_{bulk}^{(hkl)}$ is the energy per atom of an 'orientated' unit cell where the conventional unit cell is transformed such that the lattice vectors are parallel to the plane in question. Furthermore, 'n' is the total number of atoms in the slab, 'A' is the associated surface area and the factor of '2' is used to account for both the top and bottom surfaces. Analysis of the iron system using this model has been done previously and while the exact value for the associated surface energies of the crystal planes often varies, the relationship between them holds constant such that for BCC α-Fe.

$$\gamma_{(110)} < \gamma_{(100)} < \gamma_{(111)}$$

5.1.3 Oxide Shell Growth

It is possible to obtain a rough estimate for the effective diffusion coefficients for the particles in the samples by comparing the decrease in the size of the iron core during heating and considering the amount of iron core material that must out-diffuse to account for this. The value for the diffusion coefficient is often determined empirically from ln(D) vs 1/T plots as such this phenological approach is a rough estimate based on observations of the particles made in TEM and STEM after annealing. In the absence of samples created at different temperatures an estimation of the effective diffusion coefficient can be obtained from the mid-oxidation particles. This is possible as the critical size for core depletion has been determined to be 28.12nm, this marks the size that the annealing conditions were such that full oxidation of the iron core was achieved. Particles below this size could in principle have completed the oxidation process faster than the annealing time and therefore the calculated diffusion rate would be slower than the real diffusion rate. This problem can be addressed by considering a particle on the critical size limit for depletion of the iron core as no particles with iron cores were observed below this size.

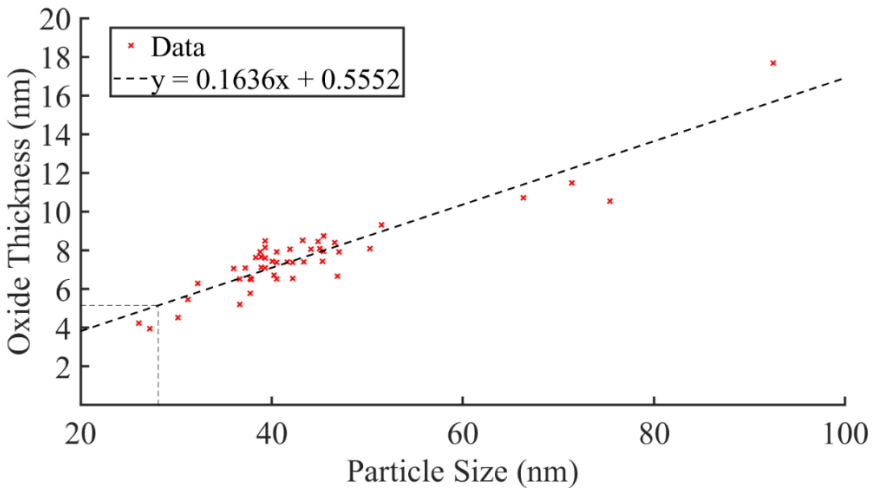

Figure 5.2 Change in oxide thickness as a function of particle size for 50 mid-oxidation particles (red) observed in the sample after annealing, the linear regression (black) has been fitted to allow for the calculation of the expect oxide shell thickness for a particle at the predicted critical size limit for core retention of 28.12nm (grey). The fitted regression has a R^2 value of 0.845 suggesting that the linear regression fitted predicts 85% of the variance in the oxide thickness.

The particle considered would have an average size of 28.12nm with an oxide shell thickness determined from the linear regression in Fig. 5.2 which shows the increase in the oxide shell thickness for particles retaining their iron cores against particle size. As such we can estimate the oxide shell thickness of a particle at the critical limit for core retention to be 5.15nm thick. This would result in an original iron core of 17.82nm which is slightly larger than the average iron core size prior to annealing. It is assumed again in this case that as the oxide shell grows the metal/oxide interface remains static while the oxide/gas interface moves outwards. This assumption comes from the idea that oxidation occurs through the out-diffusion of iron ions rather than the in-diffusion of oxygen ions, this is based on the difference in the diffusion coefficients for iron and oxygen ions in magnetite which at differ by several orders of magnetite for example, at temperatures of 823K the values are 10^{-13} cm^2/s and 10^{-18} cm^2/s respectively[132]. A schematic diagram of the evolution of the particle during annealing is shown in Fig 5.3 and shows the outward expansion of the oxide shell and the shrinking of the iron core forming interface Kirkendall voids.

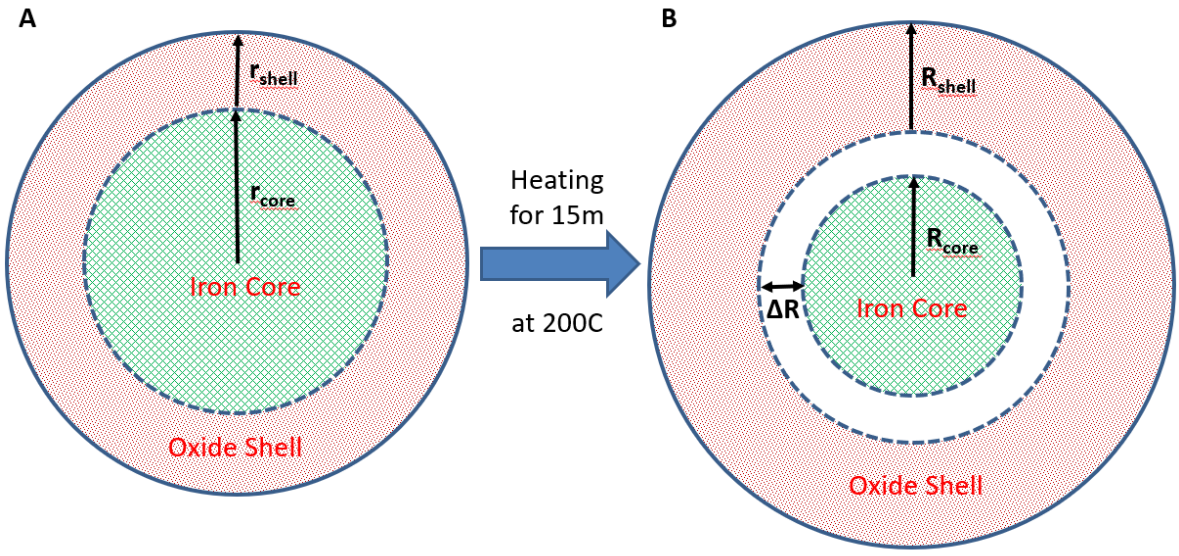

Figure 5.3 Schematic diagram showing an overview of the change in the particle during heating with A] before heating and B] after heating. The radius of the core shrinks as material diffuses out to the surface adding to the thickness of the oxide shell. The heating is conducted in atmospheric conditions resulting in instant oxidation of the material on the surface. The void region is formed through the comparative diffusion coefficients for iron out-diffusion and oxygen in-diffusion, with the latter being up to 5 orders of magnitude slower[132].

As oxidation progresses these voids are expected to coalesce together to form a ring at the metal/oxide interface that will expand as the core shrinks further due to heating, the final result will be the 'hollow' iron oxide particles described previously. As such we can predict the flux of iron atoms that have diffused out-wards per unit area and unit time where the area is equal to the surface area of the particle and the time is equal to the annealing time. This results in a diffusing flux of $2.1 \times 10^{-12}\ kg\ cm^{-2}s^{-1}$. If we then assume that the concentration profile for iron goes from a maximum at the metal/oxide interface to zero at the oxide/gas interface as shown in Fig. 5.4 we can then estimate the effective diffusion coefficient using Fick's law.

$$J = -D\frac{dC(x)}{dx} \tag{5.5}$$

This leads to an estimated diffusion coefficient for a 28.12nm thick particle with 5.15nm thick oxide shell assuming that oxidation proceeds through the out-diffusion of iron of $1.37 \times 10^{-12} cm\ s^{-1}$. The concentration gradient was estimated as the density of iron atoms at in α-Fe at one side of the oxide and zero at the surface of the particle. The same analysis can be expanded to include all particles that have retained some portion of their iron core, this is possible as the amount of material that has been oxidised from the core during annealing can be estimated from the size of the Kirkendall interface voids. Assuming an immobile metal/oxide boundary the distance between the void/oxide boundary and the metal/void boundary should be equal to the volume of iron core that has been oxidised. The distribution of the calculated diffusivities has been presented in Fig. 5.5 which displays an increase of the diffusivity with increasing particle size. The average diffusion coefficient was found to be $8.41 \times 10^{-12}\ cm^{-2}s^{-1}$ which represents a significant increase the diffusion coefficients measured in previous literature.

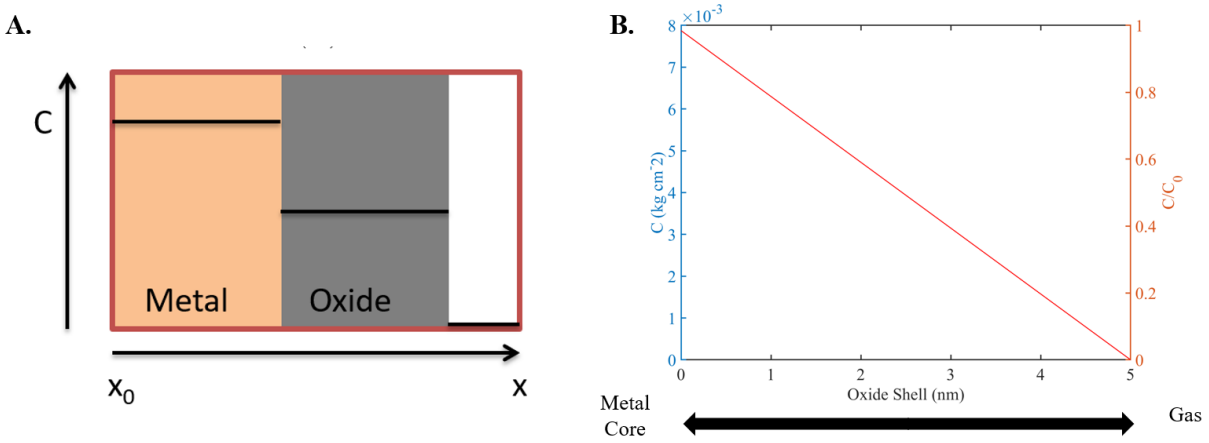

Figure 5.4 A) Schematic diagram of the Fe concentration gradient across a particle and B) calculated concentration gradient across the predicted oxide shell for a 28.12nm particle.

The diffusivities calculated are close to the levels of liquid metal and have been seen in high temperature studies with Dieckmann et al[133] finding diffusion coefficients for bulk iron at temperatures between 900-1400K of between $10^{-11}cm^{-2}s^{-1}$ and $10^{-14}cm^{-2}s^{-1}$. Atkinson et al[134] studied the diffusion of bulk iron at the lower temperature of 773K and found diffusivities of $10^{-16}\ cm^{-2}s^{-1}$. For Fe diffusion at temperatures similar to the study here, Sidhu et al[135] found the coefficient to be of the order of $10^{-15}\ cm^{-2}s^{-1}$at 190 K which makes it an order faster than Atkinson's coefficient despite the much lower temperature. Hence, the rates of oxidation observed in the nanoparticles studied here are greatly enhanced over what would be expected for annealing at 200°C while still remaining in the range of diffusivities that have been observed at other temperatures.

The increase in the observed diffusion rates with particle size is likely due to the fact that as spherical particles increase in size more grain boundaries are introduced into the oxide shell due to the larger particle being able to sustain a greater number of grains in the shell. It is predicted that the contribution to the oxidation provided by a greater number of grain boundaries in a particle plays a significant role in the oxidation process spherical nanoparticles. As such understanding how, grain boundaries fit into the oxidation model is important and will be explored in the next section.

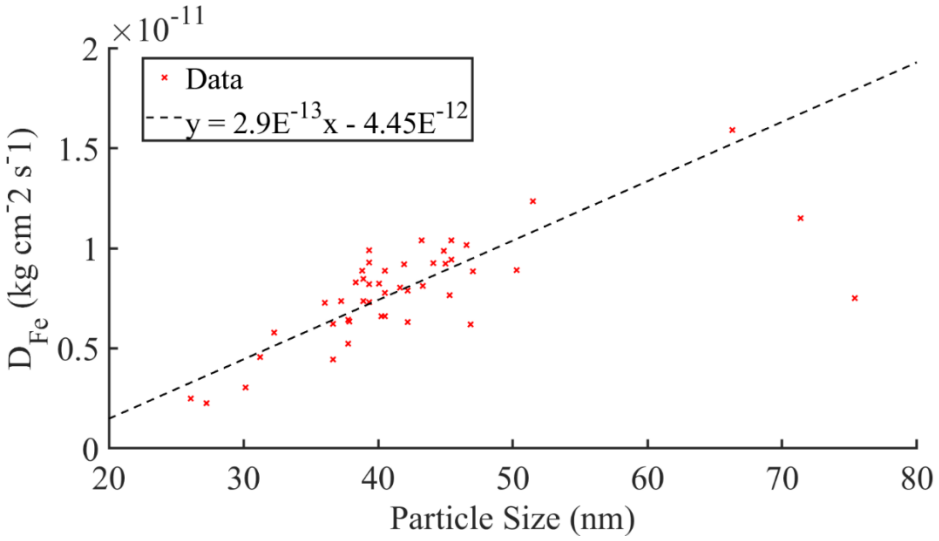

Figure 5.5 Graph showing the calculated diffusivities of 50 partially-oxidised particles that have retained their iron cores and developed Kirkendall voids at the interface, the average diffusion coefficient was found to be $8.41 \times 10^{-12}\ kg\ cm^{-2}s^{-1}$. The linear regression was plotted to show the general increase in the diffusivity with particle size and has a R^2 value of 0.67.

5.3 Contribution from Grain Boundaries

The role of grain boundary diffusion has been shown to have a significant role in diffusion at temperatures below 500K with the contribution to the overall diffusion of the sample increasing as temperatures are lowered. This is compounded by the density of grain boundaries in the sample with spherical particles possessing a much larger fraction of grain boundaries when compared to the bulk lattice. A grain boundary is the interface between two crystal grains in a polycrystalline material, they are 2D defects that are often associated a reduction in conductivity and an increase in the rate of diffusion. To describe a grain boundary crystallographically several variables need to be used[136]. The standard way of describing the boundary is through the rotation of a grain by angle θ about a rotation axis **o** which is often described by its Miller index [h,k,l]. The orientation of the grain is described by the Miller index of the normal to the boundary plane. As such the common way of expressing a grain boundary takes the form $\theta[h_i,k_i,l_i](h_{ni},k_{ni},l_{ni})$ where θ is the misfit or misorientation angle.

In a grain boundary, individual atoms are displaced from their regular lattice sites compared to the crystal structure of the bulk lattice. Grain boundaries occur in one of or a combination of two types; the first is the twist boundary where one grain is rotated about the normal of the boundary plane and the second tilt boundary is where one grain is rotated by an angle perpendicular to the boundary plane. Furthermore, grain boundaries can be distinguished by two different groups, low-angle grain boundaries and high-angle grain boundaries. In some literature the terms small-angle and large-angle are used respectively although the definitions are the same and can be used interchangeably, the former descriptions will be used here.

If the angle between two grains is sufficiently small enough, typically $\theta < 15°$ then the boundary can be adequately described through the model proposed by Burgers in 1940[136]. In this model it was proposed that a low angle tilt boundary joined through two simple cubic grains with a common axis can be thought of as composing of a series of edge dislocations parallel to the cube direction. The spacing between the dislocations is given as;

$$\lambda_d = \frac{b}{2\,sin\left(\frac{\theta}{2}\right)} \cong \frac{b}{\theta} \tag{5.6}$$

Where b is the Burgers vector for the lattice. This is the vector that describes the difference between the distorted lattice around a dislocation and the perfect lattice by denoting the direction and magnitude of atomic displacements due to dislocation.

The dislocation spacing λ_d will decrease with increasing angle θ with the spacing between individual dislocations becoming so small that they will eventually be unresolvable and will appear as extended clusters of dislocations. Generally, this point is taken to be around 13° to 15° corresponding to a value of $\lambda_d \approx 4|b|$[137]. This represents the upper limit for the validity of the dislocation model of grain boundaries and the transition point between a low-angle and high-angle grain boundary. This limit is justified in literature by the transition away from a low-angle structure to the grain boundaries occurring at 15° in bismuth or 13.6° in aluminium[138,139]. An example of a low-angle boundary is shown in Fig. 5.6 with the structure of the low-angle grain boundaries for magnetite simulated using CrystalKit

used to create Fig. 5.7. Diffusion through low-angle boundaries has been found to be similar to diffusion through the bulk lattice with the low-angle grain boundary acting as a slightly more open lattice with diffusion along low-angle boundaries being similar to the bulk lattice[140].

As the grain boundary angle increases beyond the limit of Burger's dislocation model the individual dislocations are no longer distinguishable as they begin to overlap, and computer simulation is needed to examine the behaviour of large-angle boundaries. These approaches operate by modelling the atoms at or nearby grain boundary regions with a given rotation angle and summing of the interaction of each individual atom with its nearby neighbours[141]. The computer simulations of multiple grain boundaries resulted in the development of the *structural unit model* for high-angle grain boundaries, the model predicts that the boundary is composed of repeating structural units[142]. Ashby et al. found the typical structural units to consist of several different polyhedral shapes which has been supported by other simulations and imaging experiments with the majority of grain structures composing of a combination of these fundamental units[143,144]. The structural units that make up the high-angle grain boundaries are described by the concept of the *coincidence site lattice model* that uses the repeated units to describe how two highly mismatched lattices collide.

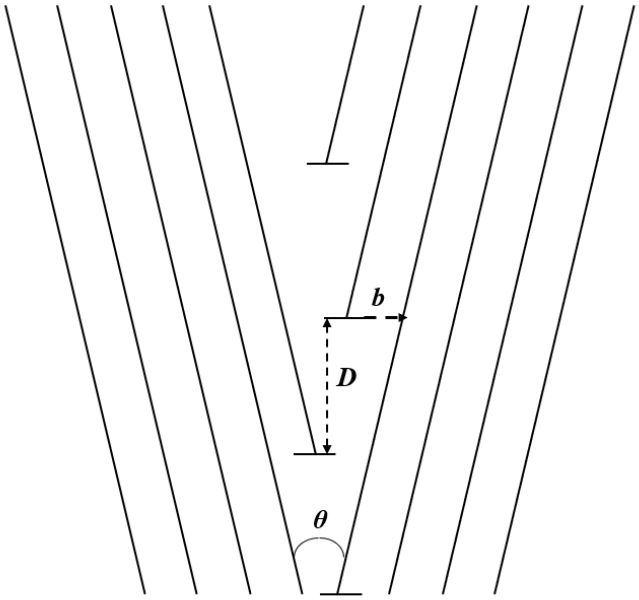

Figure 5.6 Schematic diagram of a low-angle grain boundary.

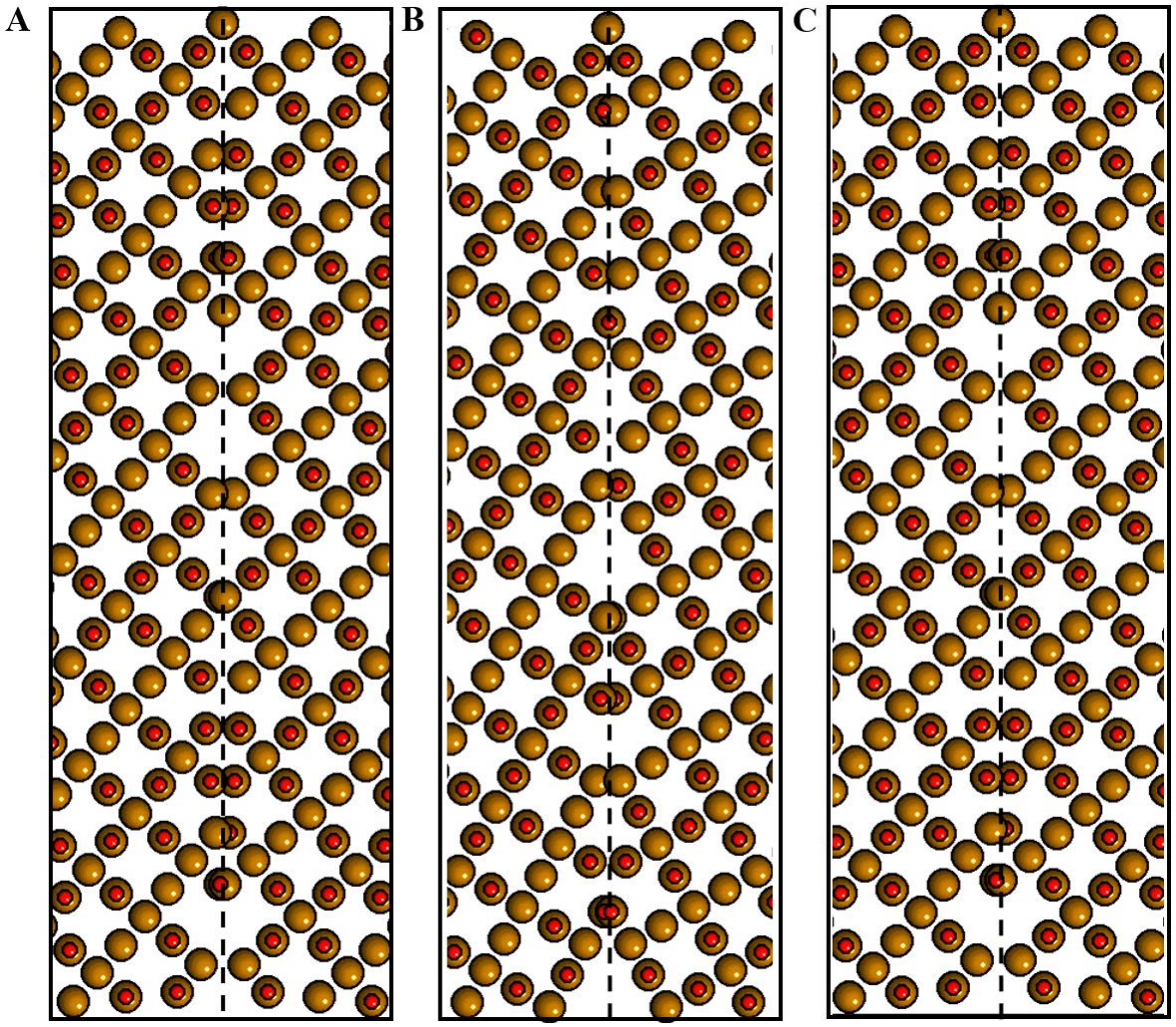

Figure 5.7 Schematic depiction of the grain boundary between two magnetite grains viewed along the [100] zone axis rotated with respect to each other by an angle of A) 10° B) 30° and C) 60°

The coincident site lattice describes the degree of fit between two neighbouring lattices as $\sum X$ where X is the number reciprocal of the ratio of coincident sites in a structural unit to the total number of sites in the unit. In the case of low-angle grain boundaries that can be described purely in terms of dislocations they will be described as $\sum 1$ grain boundaries, in high-angle grain boundaries they may be described as $\sum 3$ and $\sum 5$ which would represent one atom in 3 or 5 respectively that would be shared between the two lattice structures. The type of grain boundary has been shown to have an effect on the local diffusion coefficient as the different boundaries have different degrees of openness. In a simple model this

would serve to lower the activation energy for diffusion along that path which would in turn lower the diffusion coefficient as per the Arrhenius in Eq. 5.7.

$$D_{gb} = D_0 \, exp\left(-\frac{E}{k_B T}\right) \tag{5.7}$$

Where D_0 is the frequency factor and E is the activation energy. The relationship between the mobility of diffusing atoms and the CSL of the grain boundary is non-linear and does not imply that high sigma grain boundaries are more mobile than low sigma boundaries, with the mobility instead determined by the atomic structure of the grain boundary.

Nanoparticles with more spherical geometries have been shown to have a larger number and density of grain boundaries in their shells as such the effective diffusion coefficient as shown in chapter 1 will have a much greater contribution from diffusion along the boundaries. Furthermore, it has been established previously that the effect of diffusion along grain boundaries is more pronounced at lower temperatures. The volume fraction of the grain boundaries has been estimated below as a function of particle geometry. This was measured using HRTEM which could be Fourier filtered to determine the average grain size in the particle, an example of a Fourier filtered particle is given in Fig. 5.8. The filtered grains were then compared to the original image to determine screen the result for any artefacts and the average grain size determined. The volume fraction was then plotted as a function of the particle geometry by assuming a grain boundary width of $\delta = 0.5\ nm$ which is commonly used value in literature[145]. The grains were taken as spherical regions surrounded by a boundary with radius of $r + \frac{\delta}{2}$ where r is the average length of the grain and the factor of 1/2 is to represent the grain boundary being shared by two neighbouring grains.

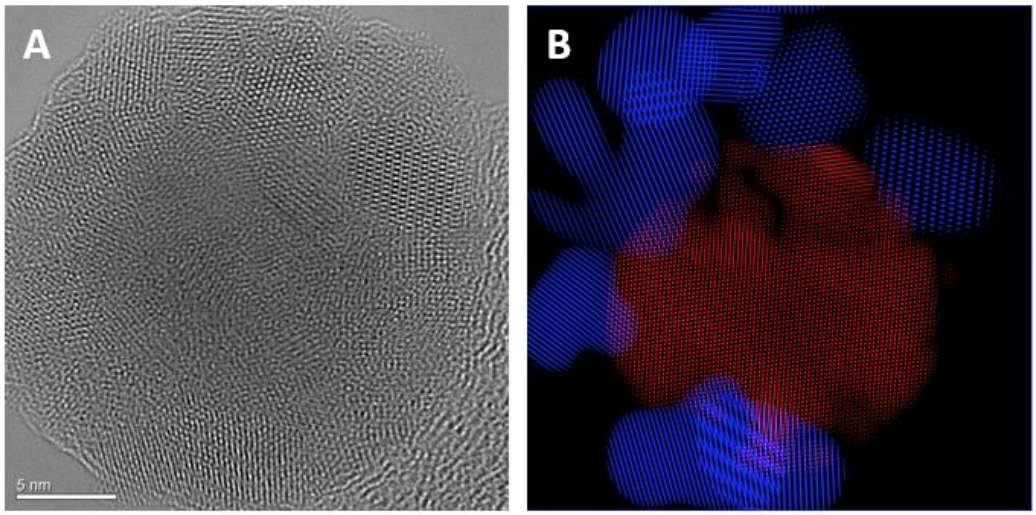

Figure 5.8 A] a Bright-field HRSTEM image of a spherical particle and B] Fourier filtered image of the particle displaying the iron core (red) and the oxide grains (blue).

The total volume of the grains with the additional component due to the grain boundary can then be compared to the volume measured without considering a grain boundary. The volume fraction of the grain boundaries in the particles is shown in Fig. 5.9. As discussed, the diffusion behaviour of low-angle and high-angle grain boundaries is very different with the former, being very similar to the bulk lattice while the latter has greatly enhanced diffusivities compared to the bulk. The diffusivity of any given grain boundary will depend on the structure of the boundary and as such will be different for different rotation angles. With the angular dependence of the diffusivity has been shown increase to a maximum rotation angle of 45° with diffusivity along grains rotated at small angle <20° being virtually indistinguishable from the bulk. This is explained by Achter and Smoluchowski[131]. To investigate the type of grain boundaries, present in the iron oxide shell the rotation angle of neighbouring grains was measured by selecting adjacent grains in the Fourier filtered HRTEM images. This is a highly qualitative approach as the structure of the individual grains is difficult to identify and hence the result is intended to show an indication of typical rotations angles and to determine whether they lie within the low-angle or high-angle regime for grain boundaries. The distribution of the rotation angles is shown in Fig. 5.10 and suggests that the majority of neighbouring grains are rotated by >15° with respect to each other

suggesting a high number of high-angle grain boundaries within the oxide shell. This aids to explain the rapid oxidation process observed in the samples.

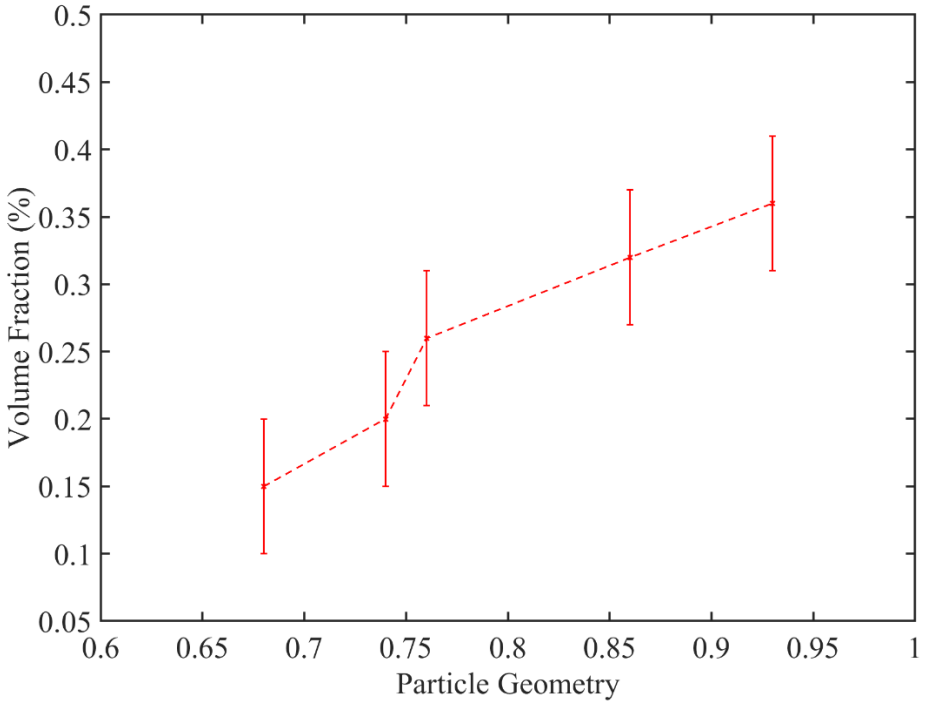

Figure 5.9 Volume fraction of grain boundaries as a percentage of the total volume of oxide shell with an assumed grain boundary width of $\delta = 0.5nm$ around spherical grains. Errors calculated through comparison of maximum and minimum threshold values when filtering grains from particle FFT.

The contribution to the diffusion due to grain boundaries can be estimated by comparing the diffusion coefficients measured previously for particles in this study with the literature values for the diffusion of Fe through magnetite. Using the diffusion coefficient put forward by Sidhu et al[135] for the diffusion of Fe in Fe_3O_4 which yields a diffusion coefficient at 190K of $1.8 \times 10^{-15} cm^2\ s^{-1}$which was determined for non-spherical iron/iron oxide nanoparticles. We can take this a measurement of the diffusion through the iron lattice as the particles used in the study were mostly cubic structured particles which have been shown to have largely monocrystalline side facets and a lower density of grain boundaries as a result.

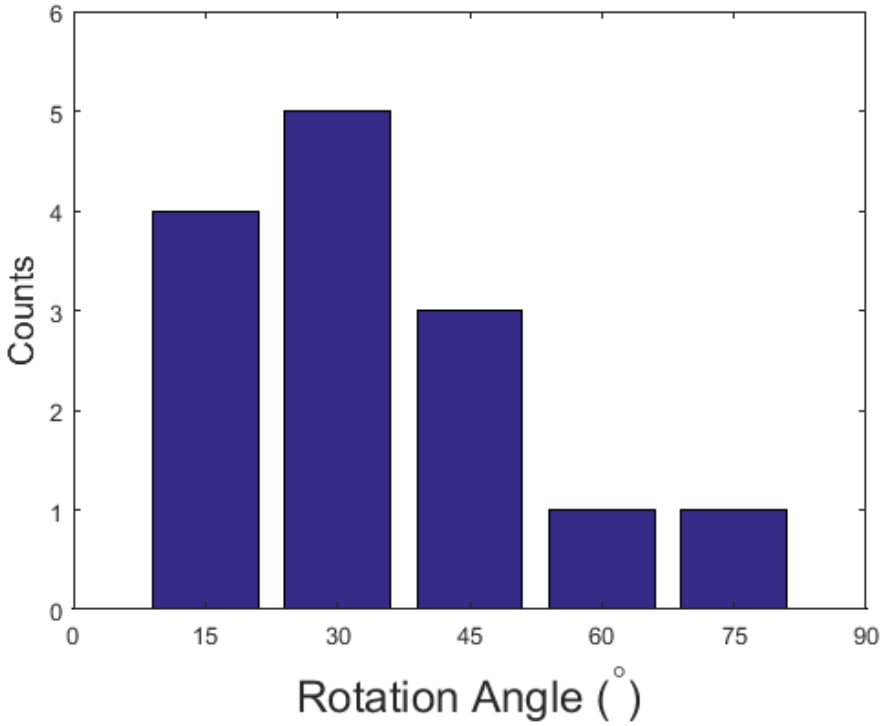

Figure 5.10 Distribution of angle of rotation between neighbouring grains in a spherical particle of R=13.7nm (fig. 5.8) the regions for grain boundaries marked as small-angle have been labelled with the other areas being classified as large-angle boundaries. The distribution shows that are over twice the number of high-angle boundaries.

We apply the equation for the effective diffusion coefficient

$$D_{eff} = gD_{gb} + (1 - g)D_l \tag{5.8}$$

where g represents the volume fraction and is equal to 3δ/d, where δ is the grain boundary width which is approximated through experiment to be 0.5nm and d is the average grain size. This provides a value for the grain boundary diffusion coefficient of

$$D_{gb} = 4.67 \times 10^{-11} cm^2\ s^{-1}$$

Due to the high density of large-angle boundaries rapid oxidation should occur in the immediate regions around the boundaries. This effect will be most prominent in spherical particles which possess a much higher density of boundaries. Due to the low temperatures for heating and short heating times it is expected that diffusion through the lattice will be negligible resulting in the atoms around the centre of grains being unable to diffuse out to the surface while the atoms located

around the boundaries would do. Combined with the relative speeds of iron out-diffusion and oxygen in-diffusion, a Kirkendall void region should begin to form at the boundary, this can be seen in Fig. 5.13 where the large cubic particle has developed voids at the corners. The result is the growth of voids around the boundaries and spoke-structures in the regions with lower boundary density. It is likely that the spokes originate due to the presence of grain boundaries in the oxide shell, diffusion along the grain boundaries is enhanced as discussed above, and as such the difference between the Fe and O ion mobility will be exaggerated. Grain boundaries at a basic level act as regions with lower activation energy, this is because high-angle grain boundaries (characterised by changes in the crystal structure) are often more open than the bulk lattice. In the case of a low-angle boundary, as discussed, they can be modelled purely through dislocations so the change in the activation energy will be minimal as the structure remains similar to the bulk lattice. Due to the lower energy barrier around the high-angle boundaries the rate of both iron out-diffusion and oxygen in-diffusion should increase, however, as the more mobile ion the effect should be greater for the Fe out-diffusion process.

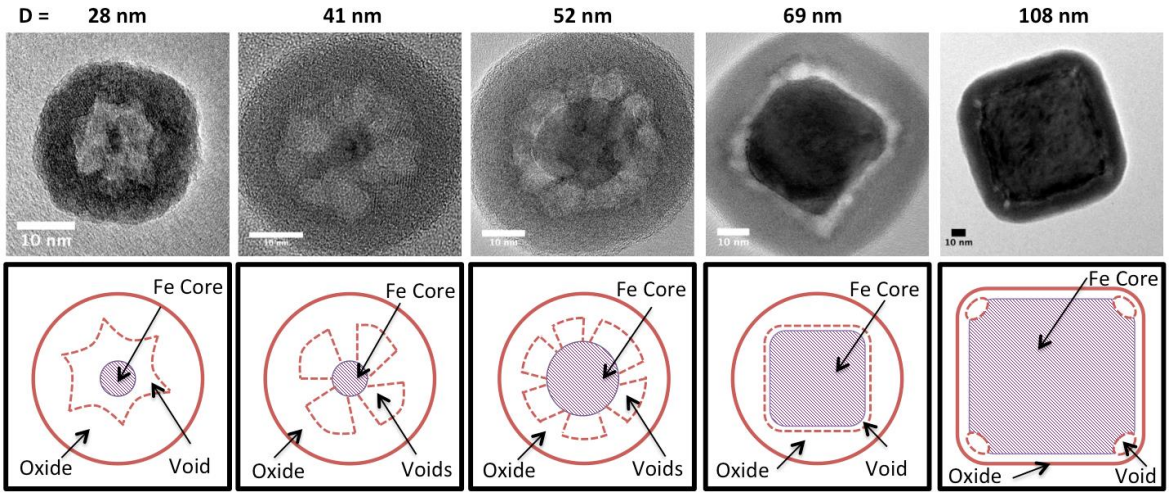

Figure 5.11 (Top) Bright-field TEM images of particles of increasing size where size collates to time in that small particles are further along in the oxidation process than larger particles due to the constant heating time and temperature. (Bottom) Schematic diagrams of the corresponding particles highlighting the smaller cores, larger shells, and void positions in each particle. With Kirkendall voids outlined by the dashed line.

This would explain why the voids form in the corners of cubic particles as seen in Fig. 5.11 and would provide an explanation for the presence of oxide ‘ridges’ as well. As the oxidation progresses the Kirkendall voids will grow and coalesce, as such, it is reasonable to expect that the last region to form voids will be at the centre of the oxide grains where the diffusion is slowest. It is also likely that after the Kirkendall voids grow to such an extent that ionic transport across the Kirkendall voids is energetically unfavourable, these oxide ‘ridges’ will serve as another pathway for oxidation.

Chapter 6: Conclusions

In chapter 3 the heating during and post-deposition of Fe/Fe_xO_y nanoparticles was discussed, and the samples characterised by the effect of the deposition temperature and post-deposition annealing on their physical properties (size, shape and shell thickness). The particles were observed to form two types of iron oxide nanoparticle as the end-point for the oxidation process, it is theorised that, cubic particles resulted in thick, 'non-hollow', iron oxide particles. This is inferred due to previous studies showing the evolution of cubic particles in atmospheric conditions into iron oxide nanoparticles with small (<20%) Kirkendall voids at the centre. This was supported by measurements of the Kirkendall void width and the idea purposed in previous studies by Pratt and Kröger et al[65] that cubic particles have enhanced oxygen in-diffusion due to the presence of strain gradients in the shell. As such it is reasonable to conclude that the thick, 'non-hollow' iron oxide particles observed in the sample originate from similar particles. This is because the cubic structure results in fewer grain boundaries which would otherwise dominate the particles diffusion behaviour. Without a large number of grain boundaries, oxidation will proceed through the strain-enhanced processes reported in the aforementioned study, resulting in iron oxide particles with small Kirkendall voids.

For spherical particles however, the behaviour is different, with particles forming 'hollow' nanoparticles with thinner oxide shells and Kirkendall voids consisting of >60% of the particles width. This suggests very rapid out-diffusion of iron with respect to the in-diffusion of oxygen, as cubic structures exhibit enhanced oxygen in-diffusion it follows that the 'hollow' iron oxide particles result from non-cubic (spherical) morphologies. This is theorised as being a result of the high grain boundary density in spherical particles due to the nature of the geometry not allowing for extended oxide facets such as the (100) facet in cubic particles. As grain boundary diffusion can be seen at a basic level as a region of lower activation energy for diffusion the resulting increase in diffusion will be greater for the already more mobile iron cations than the oxygen anions. This would result in extended Kirkendall

voids due to the relative difference in ion mobility being exaggerated by the presence of grain boundaries in the oxide.

Partially oxidised particles were also observed in the sample, these particles were often larger, as larger particles are more insensitive to the annealing-driven oxidation. The particles were found to form Kirkendall voids at the metal/oxide interface as opposed to at the centre of the particle with oxide 'ridges' separating the voids and linking the shell to the remaining iron core. It is believed that the oxide 'ridge' structures, which, have not been commonly reported in literature are formed at regions corresponding to the centre of oxide grains. This is because the iron out-diffusion results in voids forming at the grain boundaries as seen in Fig. 5.11 where a large cubic particle has developed small Kirkendall voids at the corner regions (where the grain boundaries would be located). As such, it is believed that the voids form around grain boundary regions and extend across the metal/oxide interface until a ring is formed. Oxidation then proceeds at slower rates due to the additional energy cost in an ion crossing the formed voids, however, given enough time/energy the particle will eventually full oxidise.

In chapter 4 the attempted coating of pure Fe nanoclusters with a Cu shell was presented. While it was not possible to determine if the Cu material had alloyed or formed the desired protective shell, dramatic changes in the samples behaviour due to the deposition temperature was observed. These changes imply a degree of Cu uptake had occurred, with particles becoming larger and more cubic with high deposition temperatures. This was in contrast to the pure Fe particles, which while becoming larger on average, also become more spherical. The presence of Cu was confirmed using EDX spectroscopy and was shown using EDX maps to be concentrated around the particles, although a small amount of copper material was spread across the sample. Furthermore, the particles were determined to have a higher magnetic saturation than bulk Fe (0.22 Am^2/g) with a value of roughly 0.26 Am^2/g. The successful adherence of copper material to the iron nanoclusters is a positive sign in creating optimised magnetic nanoparticles for biomedical applications. The retention of the cubic morphology at higher deposition temperatures is also beneficial as it has been found that cubic particles have better performance as MRI contrast agents[147].

Lastly, in chapter 5 a statistical estimation of the diffusion coefficient was made by comparing the amount of diffused material in a particle that was large enough to completely lose it core within the heating period of 15 minutes. This was then compared with measurements for 50 particles with an estimated effective diffusion coefficient of $8.41 \times 10^{-12}\ kg\ cm^{-2}s^{-1}$ which is similar to the coefficients determined for iron at temperatures over 900K, suggesting that diffusion at lower temperatures is greatly enhanced. This enhanced oxidation at lower temperatures may prove problematic when optimising nanoparticles for biomedical applications. As such, being able to control the distribution of geometries in the sample such that the oxidation pathway taken is closer to that observed in cubic particles, would allow for the tuning of the particles oxidation behaviour. This would be very important in creating particles for biomedical applications where oxidation is not a desired outcome.

Despite the conclusions mentioned above there were a number of technical issues that were encountered, as the samples were observed and measured after annealing, the conclusion surrounding the nature of the oxidation processes are inferred. As such, there are a number of areas for further study that would be productive. Firstly, it would be ideal to observe the oxidation processes in real time, this could be done using an *in situ* TEM heating holder, although it would need to allow for the same atmospheric conditions to be achieved. Secondly, it would be useful to simulate the effect of heating on the iron/iron oxide interface using a computer simulation method such as LLAMPS. This would provide important theoretical backing to the observation made in the samples studied here as modelling the grain boundaries in such a manner may determine the origin of the oxide 'ridge' structures observed.

Furthermore, in the case of the Fe@Cu particles, the fact that the EDX analysis suggests that the materials have alloyed as opposed to forming a complete shell, means it would be useful to extend the study to other magnetic alloy nanoparticles. Materials such as: Fe-Co and Fe-Pd would be interesting to study, in particular Fe-Co alloys as $Fe_{60}Co_{40}$ is a material known for having a very high magnetic saturation which would make it an ideal candidate in medical applications and as a follow-on study to the materials presented here.

Bibliography

1. Mangematin V, Walsh S. *The future of nanotechnologies*, (2012): p. 157-160.
2. Ever, P. *Nanotechnology in Medical Applications: The Global Market*. BCC Research (2015).
3. Ahmed N, Fessi H, Elaissari A. *Theranostic applications of nanoparticles in cancer*. *Drug discovery today*. 2012 Sep 30;17(17):928-34.
4. Liu Z, Tabakman S, Welsher K, Dai H. Carbon nanotubes in biology and medicine: in vitro and in vivo detection, imaging and drug delivery. Nano research. 2009 Feb 1;2(2):85-120.
5. Sondi I, Salopek-Sondi B. Silver nanoparticles as antimicrobial agent: a case study on E. coli as a model for Gram-negative bacteria. Journal of colloid and interface science. 2004 Jul 1;275(1):177-82.
6. Daniel MC, Astruc D. Gold nanoparticles: assembly, supramolecular chemistry, quantum-size-related properties, and applications toward biology, catalysis, and nanotechnology. Chemical reviews. 2004 Jan 14;104(1):293-346.
7. Johannsen M, Thiesen B, Wust P, Jordan A. Magnetic nanoparticle hyperthermia for prostate cancer. International Journal of Hyperthermia. 2010 Dec 1;26(8):790-5.
8. Kahn O. Molecular magnetism. VCH Publishers, Inc.(USA), 1993,. 1993:393.
9. Langenberg A, Hirsch K, Ławicki A, Zamudio-Bayer V, Niemeyer M, Chmiela P, Langbehn B, Terasaki A, Issendorff BV, Lau JT. Spin and orbital magnetic moments of size-selected iron, cobalt, and nickel clusters. Physical Review B. 2014 Nov 19;90(18):184420.
10. Schenck JF. The role of magnetic susceptibility in magnetic resonance imaging: MRI magnetic compatibility of the first and second kinds. Medical physics. 1996 Jun 1;23(6):815-50.
11. Terris, B. D. & Thomson, T. Nanofabricated and self-assembled magnetic structures as data storage media. J. Phys. D 38, R199–R222 (2005).
12. Cundy, A. B., Hopkinson, L. & Whitby, R. L. D. Use of iron-based technologies in contaminated land and groundwater remediation: A review. Sci. Total Environ. 400, 42–51 (2008).

13. Pankhurst QA, Connolly J, Jones SK, Dobson JJ. Applications of magnetic nanoparticles in biomedicine. Journal of physics D: Applied physics. 2003 Jun 18;36(13):R167.
14. Tartaj P, Veintemillas-Verdaguer S, Serna CJ. The preparation of magnetic nanoparticles for applications in biomedicine. Journal of Physics D: Applied Physics. 2003 Jun 18;36(13):R182.
15. Gupta AK, Gupta M. Synthesis and surface engineering of iron oxide nanoparticles for biomedical applications. Biomaterials. 2005 Jun 30;26(18):3995-4021.
16. Dieckmann R, Schmalzried H. Defects and cation diffusion in magnetite (I). Berichte der Bunsengesellschaft für physikalische Chemie. 1977 Mar 1;81(3):344-7.Sounderya N, Zhang Y. Use of core/shell structured nanoparticles for biomedical applications. Recent Patents on Biomedical Engineering. 2008 Jan 1;1(1):34-42.Perigo
17. EA, Hemery G, Sandre O, Ortega D, Garaio E, Plazaola F, Teran FJ. Fundamentals and advances in magnetic hyperthermia. Applied Physics Reviews. 2015 Dec;2(4):041302.
18. Hussey RJ, Caplan D, Graham MJ. The growth and structure of oxide films on Fe. II. Oxidation of polycrystalline Fe at 240–320° C. Oxidation of Metals. 1981 Jun 1;15(5-6):421-35.
19. Gilchrist R K, Medal R, Shorey W D, Hanselman R C, Parrott J C and Taylor C B 1957 Selective inductive heating of lymph nodes Ann. Surg. 146 596–606
20. Reilly J P 1992 Principles of nerve and heart excitation by time-varying magnetic fields Ann. New York Acad. Sci. 649 96–117
21. Curvo-Semedo L, Caseiro-Alves F. MR Contrast agents. InClinical MRI of the Abdomen 2009 (pp. 17-39). Springer Berlin Heidelberg.
22. Khawaja AZ, Cassidy DB, Al Shakarchi J, McGrogan DG, Inston NG, Jones RG. Revisiting the risks of MRI with Gadolinium based contrast agents—review of literature and guidelines. Insights into imaging. 2015 Oct 1;6(5):553-8.
23. Wang YX. Superparamagnetic iron oxide based MRI contrast agents: current status of clinical application. Quantitative imaging in medicine and surgery. 2011 Dec;1(1):35.

24. Maier-Hauff K, Rothe R, Scholz R, Gneveckow U, Wust P, Thiesen B, Feussner A, von Deimling A, Waldoefner N, Felix R, Jordan A. Intracranial thermotherapy using magnetic nanoparticles combined with external beam radiotherapy: results of a feasibility study on patients with glioblastoma multiforme. Journal of neuro-oncology. 2007 Jan 1;81(1):53-60.
25. Brusentsov NA, Nikitin LV, Brusentsova TN, Kuznetsov AA, Bayburtskiy FS, Shumakov LI, Jurchenko NY. Magnetic fluid hyperthermia of the mouse experimental tumor. Journal of Magnetism and Magnetic Materials. 2002 Nov 1;252:378-80.
26. Atkinson WJ, Brezovich IA, Chakraborty DP. Usable frequencies in hyperthermia with thermal seeds. IEEE Transactions on Biomedical Engineering. 1984 Jan(1):70-5.
27. Laurent S, Forge D, Port M, Roch A, Robic C, Vander Elst L, Muller RN. Magnetic iron oxide nanoparticles: synthesis, stabilization, vectorization, physicochemical characterizations, and biological applications. Chemical reviews. 2008 Jun 11;108(6):2064-110.
28. Kumari M. *Magnetic properties of iron-oxide nanoparticles and methods for their characterization* (Doctoral dissertation).
29. Levy D, Giustetto R, Hoser A. Structure of magnetite (Fe 3 O 4) above the Curie temperature: a cation ordering study. Physics and Chemistry of Minerals. 2012 Feb 1;39(2):169-76.
30. Shavel A, Rodríguez-González B, Spasova M, Farle M, Liz-Marzán LM. Synthesis and characterization of iron/iron oxide core/shell nanocubes. Advanced functional materials. 2007 Dec 17;17(18):3870-6.
31. Yin Y, Rioux RM, Erdonmez CK, Hughes S, Somorjai GA, Alivisatos AP. Formation of hollow nanocrystals through the nanoscale Kirkendall effect. Science. 2004 Apr 30;304(5671):711-4.
32. Wang CM, Baer DR, Thomas LE, Amonette JE, Antony J, Qiang Y, Duscher G. Void formation during early stages of passivation: Initial oxidation of iron nanoparticles at room temperature. Journal of Applied Physics. 2005 Nov 1;98(9):094308.
33. Cabrera NF, Mott NF. Theory of the oxidation of metals. Reports on progress in physics. 1949 Jan 1;12(1):163.Adsc

34. Evans VR. *The corrosion and oxidation of metals (Second Supplementary Volume)*. 1976.
35. Hauffe K. *Oxidation of Metals*. 1965.
36. Kubaschewski O, Hopkins BE. *Oxidation of Metals and Alloys*. 1967.
37. Ahmad Z. High Temperature Corrosion. InTech. 2016 Sep.
38. Darken L, Gurry RW. The system iron—oxygen. II. Equilibrium and thermodynamics of liquid oxide and other phases. Journal of the American Chemical society. 1946 May;68(5):798-816.
39. Davies MH, Simnad MT. c. E. Birchenall. Journal of Metals, Transactions, AIME. 1951:889.
40. Himmel L, Mehl RF, Birchenall CE. Self-diffusion of iron in iron oxides and the Wagner theory of oxidation. Trans. Aime. 1953 Jan 1;197(6):827-43.
41. Fromhold Jr AT. Theory of Metal Oxidation. Fundamentals. North Holland Publishing Co., Amsterdam, New York and Oxford. 1976, 547 p. 1976.
42. Xu C, Gao W. Pilling-Bedworth ratio for oxidation of alloys. Materials Research Innovations. 2000 Mar 1;3(4):231-5.
43. Bedworth RE, Pilling NB. The oxidation of metals at high temperatures. J Inst Met. 1923;29(3):529-82.
44. Leontis TE, Rhines FN. Rates of high temperature oxidation of magnesium and magnesium alloys. Transactions AIME. 1946 Jan 1;166:265-94.
45. C. Wagner, Beitrag zur Theorie des Anlaufvorgangs, Z. phys. Chem 21, 1933, 25-41
46. Atkinson A. Transport processes during the growth of oxide films at elevated temperature. Reviews of Modern Physics. 1985 Apr 1;57(2):437.
47. Atkinson A, Taylor RI. Diffusion of 55Fe in Fe2O3 single crystals. Journal of Physics and Chemistry of Solids. 1985 Jan 1;46(4):469-75.
48. N. Birks, G.H. Meier, Introduction to High Temperature Oxidation of Metals, Edward Arnold Ltd 1983
49. P. Kofstad, High Temperaure Corrosion, Elsevier Ltd 1988
50. Ritchie IM. Chemisorption and Reactions on Metallic Films, Vol. by JR Anderson.
51. Fromhold Jr AT. Theory of metal oxidation. Vol. 2.
52. Fehlner FP, Mott NF. Low-temperature oxidation. Oxidation of Metals. 1970 Mar 1;2(1):59-99.

53. Mantina M, Wang Y, Arroyave R, Chen LQ, Liu ZK, Wolverton C. First-principles calculation of self-diffusion coefficients. Physical review letters. 2008 May 30;100(21):215901.
54. Ermoline A, Dreizin EL. Equations for the Cabrera–Mott kinetics of oxidation for spherical nanoparticles. Chemical Physics Letters. 2011 Mar 21;505(1-3):47-50.
55. Blaney L. Magnetite (Fe3O4): Properties, synthesis, and applications.
56. Rae AI. Quantum Mechanics 5th Edition.
57. Mahapatra AK, Bhatta UM, Som T. Oxidation mechanism in metal nanoclusters: Zn nanoclusters to ZnO hollow nanoclusters. Journal of Physics D: Applied Physics. 2012 Sep 27;45(41):415303.
58. Low GG. Some measurements of phonon dispersion relations in iron. Proceedings of the Physical Society. 1962 Mar;79(3):479.
59. Mahapatra AK, Bhatta UM, Som T. Oxidation mechanism in metal nanoclusters: Zn nanoclusters to ZnO hollow nanoclusters. Journal of Physics D: Applied Physics. 2012 Sep 27;45(41):415303.
60. Dean, John A. Lange's Handbook of Chemistry, 12th ed.; McGraw-Hill: New York, New York, 1979; p 9-4–9-94
61. Grosvenor AP, Kobe BA, McIntyre NS. Activation energies for the oxidation of iron by oxygen gas and water vapour. Surface Science. 2005 Jan 10;574(2-3):317-21.
62. Grosvenor AP, Kobe BA, McIntyre NS. Examination of the oxidation of iron by oxygen using X-ray photoelectron spectroscopy and QUASESTM. Surface science. 2004 Sep 10;565(2-3):151-62.
63. Sidhu PS, Gilkes RJ, Posner AM. Mechanism of the low temperature oxidation of synthetic magnetites. Journal of Inorganic and Nuclear Chemistry. 1977 Jan 1;39(11):1953-8.
64. LaGrow, A. P. et al. Synthesis, alignment and magnetic properties of monodisperse nickel nanocubes. J. Am. Chem. Soc. 134, 855–858 (2012).
65. Pratt A, Lari L, Hovorka O, Shah A, Woffinden C, Tear SP, Binns C, Kröger R. Enhanced oxidation of nanoparticles through strain-mediated ionic transport. Nature materials. 2014 Jan;13(1):26.
66. Fick A. Ueber diffusion. Annalen der Physik. 1855 Jan 1;170(1):59-86.

67. Levine HS, MacCallum CJ. Grain boundary and lattice diffusion in polycrystalline bodies. Journal of Applied Physics. 1960 Mar;31(3):595-9.
68. Suzuki A, Mishin Y. Atomic mechanisms of grain boundary diffusion: Low versus high temperatures. Journal of materials science. 2005 Jun 1;40(12):3155-61.
69. Paul A, Laurila T, Vuorinen V, Divinski SV. Fick's Laws of Diffusion. InThermodynamics, Diffusion and the Kirkendall Effect in Solids 2014 (pp. 115-139). Springer International Publishing.
70. Liu CL, Plimpton SJ. Molecular-statics and molecular-dynamics study of diffusion along [001] tilt grain boundaries in Ag. Physical Review B. 1995 Feb 15;51(7):4523.
71. Wang YJ, Gao GJ, Ogata S. Atomistic understanding of diffusion kinetics in nanocrystals from molecular dynamics simulations. Physical Review B. 2013 Sep 9;88(11):115413.
72. Jamnik J, Kalnin JR, Kotomin EA, Maier J. Generalised Maxwell-Garnett equation: application to electrical and chemical transport. Physical Chemistry Chemical Physics. 2006;8(11):1310-4.
73. Prokoshkina D, Esin VA, Wilde G, Divinski SV. Grain boundary width, energy and self-diffusion in nickel: effect of material purity. Acta Materialia. 2013 Aug 31;61(14):5188-97.
74. Lide DR. Magnetic susceptibility of the elements and inorganic compounds. CRC handbook of chemistry and physics. 2005;73:9.
75. Baker, S., Thornton, S., Edmonds, W., Maher, M. J., Norris, C., & Binns, C. (2000). The construction of a gas aggreation source for the preparation of size-selected nanoscale transition metal clusters. Review of Scientific Instruments, 3178-3183.
76. Karlsson HL, Cronholm P, Gustafsson J, Moller L. Copper oxide nanoparticles are highly toxic: a comparison between metal oxide nanoparticles and carbon nanotubes. Chemical research in toxicology. 2008 Aug 19;21(9):1726-32.
77. Hirsch, PB, Howie, A, Nicholson, RB, Pashley, DW and Whelan, MJ 1977 Electron Microscopy of Thin Crystals 2nd Ed. Krieger Huntington NY
78. Rother A, Scheerschmidt K. Relativistic effects in elastic scattering of electrons in TEM. Ultramicroscopy. 2009 Jan 1;109(2):154-60.

79. Williams DB, Carter CB, Veyssiere P. Transmission electron microscopy: a textbook for materials science. New York: Springer; 1998.
80. Bleloch A, Brown LM, Brydson R, Craven A, Goodhew P, Kiely C. The superSTEM: An Aberration Corrected Analytical Microscopy Facility. Microsc. Microanal. 2002 Aug;1.
81. Garratt-Reed, AJ and Bell, DC 2002 Energy-Dispersive X-ray Analysis in the Electron Microscope Bios (Royal Microsc. Soc.) Oxford, UK
82. Thomas PJ, Midgley PA. Image-spectroscopy–II. The removal of plural scattering from extended energy-filtered series by Fourier deconvolution. Ultramicroscopy. 2001 Aug 1;88(3):187-94.
83. DeGraef, M 2003 Introduction to Conventional Transmission Microscopy Cambridge University Press New York
84. Chang CC. Auger electron spectroscopy. Surface Science. 1971 Mar 1;25(1):53-79.
85. Egerton, RF 2006 Physical Principles of Electron Microscopy; An Introduction to TEM, SEM, and AEM Springer New York
86. Egerton RF, Li P, Malac M. Radiation damage in the TEM and SEM. Micron. 2004 Aug 1;35(6):399-409.
87. Mott NF, Massey HS. The theory of atomic collisions. Oxford: Clarendon Press; 1965.
88. Bragg, WL 1965 The Crystalline State I Ed. WL Bragg Cornell University Press Ithaca NY
89. Reimer, L 1997 Transmission Electron Microscopy; Physics of Image Formation and Microanalysis 4th Ed. Springer-Verlag New York
90. Stewart M, Vigers G. Electron microscopy of frozen-hydrated biological material. Nature. 1986 Feb;319(6055):631.
91. Fultz, Brent and Howe, James M. (2007) *Transmission Electron Microscopy and Diffractometry of Materials (Third Edition).* Springer , Heidelberg.
92. Hirsch PB, Whelan MJ. A kinematical theory of diffraction contrast of electron transmission microscope images of dislocations and other defects. Phil. Trans. R. Soc. Lond. A. 1960 May 5;252(1017):499-529.
93. C. Kisielowski et al. (2008). *"Detection of single atoms and buried defects in three dimensions by aberration-corrected electron microscopy with 0.5 Å information limit"*. Microscopy and Microanalysis. **14**: 469–477.

94. Boersch, H, Hamisch, H, Wohlleben, D and Grohmann, K 1920 Z. Phys. 159 397–404
95. Wade, R. H. (October 1992). *A brief look at imaging and contrast transfer*. Ultramicroscopy. **46**: 145–156
96. Ludwig Reimer (1997 4th ed) *Transmission electron microscopy: Physics of image formation and microanalysis* (Springer, Berlin)
97. Lentzen M, Jahnen B, Jia CL, Thust A, Tillmann K, Urban K. High-resolution imaging with an aberration-corrected transmission electron microscope. Ultramicroscopy. 2002 Aug 1;92(3-4):233-42.
98. Isaacson, M, Ohtsuki, M and Utlaut, M 1979 in Introduction to Analytical Electron Microscopy p 343 Eds. JJ Hren, JI Goldstein and DC Joy Plenum Press New York.
99. Clarke, A. R. (2002) Microscopy techniques for materials science. CRC Press (electronic resource)
100. Lund, MW 1995 Current Trends in Si(Li) Detector Windows for Light Element Analysis in X-Ray Spectrometry in Electron Beam Instruments DB Williams, JI Goldstein and DE Newbury, Eds. 21–31 Plenum Press New York.
101. Garratt-Reed, AJ and Bell, DC 2002 Energy-dispersive X-ray Analysis in the Electron Microscope Bios (Royal Microsc. Soc.) Oxford UK
102. Novel Magnetic Nanoparticles for Medical Applications. (2018). K. Dexter. University of Leicester
103. Binns C. Nanoclusters deposited on surfaces. Surface science reports. 2001 Oct 1;44(1-2):1-49.
104. Lan Y, Wang H, Wang D, Chen G, Ren Z. Grids for Applications in High-Temperature High-Resolution Transmission Electron Microscopy. Journal of Nanotechnology. 2010;2010.
105. Zhang Z, Su D. Behaviour of TEM metal grids during in-situ heating experiments. Ultramicroscopy. 2009 May 1;109(6):766-74.
106. Karlsson G. Thickness measurements of lacey carbon films. Journal of microscopy. 2001 Sep 1;203(3):326-8.
107. Saito Y, Mihama K, Uyeda R. Formation of ultrafine metal particles by gas-evaporation VI. Bcc metals, Fe, V, Nb, Ta, Cr, Mo and W. Japanese Journal of Applied Physics. 1980 Sep;19(9):1603.

108. Granqvist CG, Buhrman RA. Ultrafine metal particles. Journal of applied Physics. 1976 May;47(5):2200-19.
109. Kiss LB, Söderlund J, Niklasson GA, Granqvist CG. New approach to the origin of lognormal size distributions of nanoparticles. Nanotechnology. 1999 Mar;10(1):25.
110. Batsidis A, Economou P, Tzavelas G. Tests of fit for a lognormal distribution. Journal of Statistical Computation and Simulation. 2016 Jan 22;86(2):215-35.
111. Clauset A, Shalizi CR, Newman ME. Power-law distributions in empirical data. SIAM review. 2009 Nov 6;51(4):661-703.
112. Wang CM, Baer DR, Amonette JE, Engelhard MH, Qiang Y, Antony J. Morphology and oxide shell structure of iron nanoparticles grown by sputter-gas-aggregation. Nanotechnology. 2007 May 29;18(25):255603.
113. Hayashi T, Ohno T, Yatsuya S, Uyeda R. Formation of ultrafine metal particles by gas-evaporation technique. IV. Crystal habits of iron and Fcc metals, Al, Co, Ni, Cu, Pd, Ag, In, Au and Pb. Japanese Journal of Applied Physics. 1977 May;16(5):705.
114. R V Zucker, D Chatain, U Dahmen, S Hagege, W C Carter. "New software tools for the calculation and display of isolated and attached interfacial-energy minimizing particle shapes." Journal of Materials Science, vol. 47, pp. 8290-8302.
115. Fromhold Jr AT, Cook EL. Kinetics of oxide film growth on metal crystals: electron tunneling and ionic diffusion. Physical Review. 1967 Jun 15;158(3):600.
116. Huber DL. Synthesis, properties, and applications of iron nanoparticles. Small. 2005 May 1;1(5):482-501.
117. Yin Y, Rioux RM, Erdonmez CK, Hughes S, Somorjai GA, Alivisatos AP. Formation of hollow nanocrystals through the nanoscale Kirkendall effect. Science. 2004 Apr 30;304(5671):711-4.
118. Fan HJ, Gösele U, Zacharias M. Formation of nanotubes and hollow nanoparticles based on Kirkendall and diffusion processes: a review. small. 2007 Oct 1;3(10):1660-71.
119. Hwang JW. Thermal expansion of nickel and iron, and the influence of nitrogen on the lattice parameter of iron at the Curie temperature.

120. Anderson JB, Fenn JB. Velocity distributions in molecular beams from nozzle sources. The physics of fluids. 1965 May;8(5):780-7.

121. Lubman DM, Rettner CT, Zare RN. How isolated are molecules in a molecular beam?. The Journal of Physical Chemistry. 1982 Apr;86(7):1129-35.

122. Nolden IM, Van Beijeren H. Equilibrium shape of bcc crystals: Thermal evolution of the facets. Physical Review B. 1994 Jun 15;49(24):17224. S

123. Saito Y, Mihama K and Uyeda R 1980 Japan. J. Appl. Phys.19 1603–10

124. Hayashi T, Ohno T, Yatsuya S and Uyeda R 1977 Japan. J.Appl. Phys. 16 705–17

125. Kapur, JN; Sahoo, PK & Wong, ACK (1985), "A New Method for Gray-Level Picture Thresholding Using the Entropy of the Histogram", Graphical Models and Image Processing 29(3): 273-285

126. Otsu N. A threshold selection method from gray-level histograms. IEEE transactions on systems, man, and cybernetics. 1979 Jan;9(1):62-6.

127. Sahoo PK, Soltani SA, Wong AK. A survey of thresholding techniques. Computer vision, graphics, and image processing. 1988 Feb 1;41(2):233-60.

128. Grochola G, Russo SP, Yarovsky I, Snook IK. “Exact” surface free energies of iron surfaces using a modified embedded atom method potential and λ integration. The Journal of chemical physics. 2004 Feb 15;120(7):3425-30

129. Jian-Min Z, Fei M, Ke-Wei X. Calculation of the surface energy of fcc metals with modified embedded-atom method. Chinese Physics. 2004 Jul;13(7):1082.

130. LaGrow AP, Ingham B, Cheong S, Williams GV, Dotzler C, Toney MF, Jefferson DA, Corbos EC, Bishop PT, Cookson J, Tilley RD. Synthesis, alignment, and magnetic properties of monodisperse nickel nanocubes. Journal of the American Chemical Society. 2011 Dec 28;134(2):855-8.

131. Wang SG, Tian EK, Lung CW. Surface energy of arbitrary crystal plane of bcc and fcc metals. Journal of Physics and Chemistry of Solids. 2000 Aug 1;61(8):1295-300.

132. Ueda M, Maruyama T. Estimation of the Effect of Grain Boundary Diffusion on Microstructure Development in Magnetite Bi-crystal under Oxygen Chemical Potential Gradient at 823 K. Journal of the Korean Ceramic Society. 2012;49(1):37-42.

133. Dieckmann R, Schmalzried H. Defects and cation diffusion in magnetite (I). Berichte der Bunsengesellschaft für physikalische Chemie. 1977 Mar 1;81(3):344-7.

134. Atkinson A. Wagner theory and short circuit diffusion. Materials science and technology. 1988 Dec 1;4(12):1046-51.

135. Sidhu PS, Gilkes RJ, Posner AM. Mechanism of the low temperature oxidation of synthetic magnetites. Journal of Inorganic and Nuclear Chemistry. 1977 Jan 1;39(11):1953-8.

136. Lejček P. Grain Boundaries: Description, Structure and Thermodynamics. Grain Boundary Segregation in Metals. 2010:5-24.

137. Kittel C. Introduction to solid state physics. Wiley; 2005.

138. Taylor GI. The mechanism of plastic deformation of crystals. Part I. Theoretical. Proceedings of the Royal Society of London. Series A. 1934 Jul 2;145(855):362-87.

139. Glicksman ME, Vold CL. Heterophase dislocations—an approach towards interpreting high temperature grain boundary behavior. Surface science. 1972 Jun 1;31:50-67.

140. Winning M, Gottstein G, Shvindlerman LS. On the mechanisms of grain boundary migration. Acta Materialia. 2002 Jan 22;50(2):353-63.

141. Couling SR, Smoluchowski R. Anisotropy of diffusion in grain boundaries. Journal of Applied Physics. 1954 Dec;25(12):1538-42.

142. Liu CL, Plimpton SJ. Molecular-statics and molecular-dynamics study of diffusion along [001] tilt grain boundaries in Ag. Physical Review B. 1995 Feb 15;51(7):4523.

143. Ashby MF, Spaepen F, Williams S. The structure of grain boundaries described as a packing of polyhedra. Acta Metallurgica. 1978 Nov 1;26(11):1647-63.

144. Smith DA. Grain boundary structure and migration. Ultramicroscopy. 1989 May 2;29(1-4):1-8.

145. Prokoshkina D, Esin VA, Wilde G, Divinski SV. Grain boundary width, energy and self-diffusion in nickel: effect of material purity. Acta Materialia. 2013 Aug 1;61(14):5188-97.

146. Achter MR, Smoluchowski R. Diffusion in Grain Boundaries. Journal of Applied Physics. 1952 Mar 1;23(3):373-4.
147. Aktaş S, Thornton SC, Binns C, Lari L, Pratt A, Kröger R, Horsfield MA. Control of gas phase nanoparticle shape and its effect on MRI relaxivity. Materials Research Express. 2015 Feb 17;2(3):035002.